Department of Information Engineering

Master's Degree in Electronic Engineering

Study on a wide-angle scanning phased antenna array for 5G mm-Wave

Supervisor:
Prof. Andrea Galtarossa

Candidate:
Edoardo Vergerio

Co-Supervisor:
Ing. Daniele Piazza

Academic Year 2023/2024

25/11/2024

Index

1 Sommario

In questo elaborato di tesi viene studiato un metodo per realizzare una schiera di antenne ad ampio angolo di scansione per applicazioni 5G mm-Wave nella banda di frequenze comprese tra 26.5 GHz e 27.5 GHz. Dopo aver descritto le caratteristiche di propagazione delle onde millimetriche, si introdurrà al ruolo che i Network Controlled Repeaters (NCRs) avranno nelle reti mobile multi-Gbit del futuro. Successivamente, si passerà alla fase di progettazione dell'elemento radiante. Tramite delle simulazioni, verrà inizialmente analizzata la cella unitaria che costituisce la schiera: una patch a microstriscia con doppia polarizzazione lineare appositamente modificata con degli elementi parassiti per ottenere un pattern di radiazione ad ampio beamwidth. Successivamente, delle schiere di tale elemento vengono simulate per valutarne il comportamento ad ampi angoli di scansione.

Questo lavoro è stato svolto durante il periodo di tirocinio presso l'azienda Adant Technologies Inc. sita in Legnaro (Padova).

2 Abstract

This thesis work studies a method to design a wide-angle scanning phased antenna array for 5G mm-Wave communication systems in the frequency band from 26.5 GHz to 27.5 GHz. After a general introduction to the propagation characteristics of millimeter waves and to the role that Network Controlled Repeaters (NCRs) will have in future, multi-Gbit mobile networks, the work will then continue with the design process of the radiating element. The array unit-cell is initially analyzed: it consists of a dual linearly polarized microstrip patch antenna that has been modified with the introduction of parasitic elements in order to obtain a wide beamwidth radiation pattern. After that, arrays of the proposed unit-cell element are simulated to evaluate their performance at large scan angles.

This work has been carried out during the internship time spent at the company Adant Technologies Inc. located in Legnaro (Padova).

3 Introduction

The technological advancements that are currently taking place in the mobile communications industry mainly revolve around the migration from 4G LTE (Long Term Evolution) to 5G NR (New Radio). The increase of wireless data traffic and the continued request for larger bandwidth has made it necessary to explore new parts of the spectrum. The current and well established transmission technologies at lower frequencies have brought to the so called *spectrum crunch*. This means that the lower frequencies spectrum has been heavily exploited and, as a result, it has become too overcrowded, making future expansions not feasible. The major leap forward brought by 5G NR will enable future networks to sustain the ever growing traffic demand. Two bands have been of particular interest: the 5G sub-6 GHz and the mm-Wave bands. In particular, 5G Frequency Range 2 (FR2) mobile networks operating in the millimeter-wave (mm-Wave) frequency range (above 24 GHz) will be the key to provide multi-gigabit data rates and very low latency. Compared to the 5G sub-6 GHz (FR1) band, mm-Wave networks allow mobile network operators to better manage dense urban scenarios and crowded environments in general, such as event venues or stadiums. Moreover, the defined bands in the sub-6 GHz range provide ≈ 5 GHz of bandwidth, which is only a third if compared to the ≈ 15 GHz of bandwidth allocated to mm-Wave bands [1]. However, moving towards higher frequencies poses significant challenges due to the worsened propagation characteristics of mm-Wave signals. Under this motivation, a lot of research is currently exploring this new part of the spectrum to make it ready for future multi-Gbit mobile networks [1].

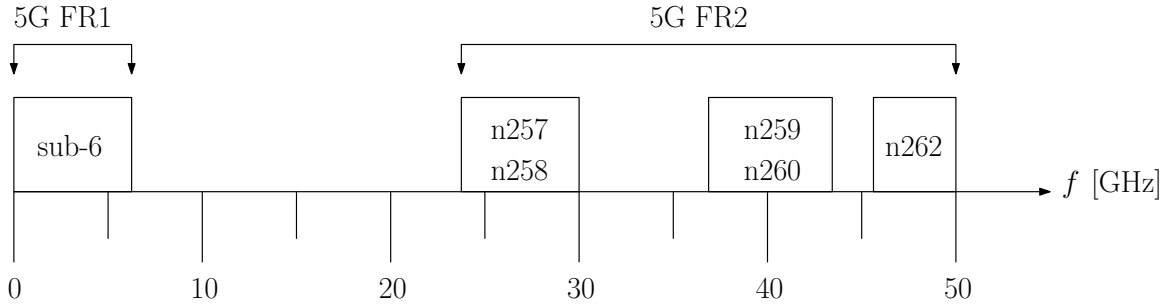

Figure 3.1: The 5G NR FR1 & FR2 bands

Band	**Frequency Range** [GHz]
n257	26.5-29.5
n258	24.25-27.5
n259	39.5-43.5
n260	37-40
n262	47.2-48.2

Table 1: The 5G NR mm-Wave Frequency Range 2 (FR2) bands

This thesis will focus on the mm-Wave bands and it is organized as follows:

- In sections 4 & 5, the main theoretical aspects of antennas and arrays that will be used in this work are reviewed.
- In section 6, the propagation characteristics of mm-Waves will be explored. This will reveal that mm-Waves suffer from higher propagation losses, if compared to the lower frequencies. An overview on real-world measuring campaigns is also given, which are needed to understand and characterize the propagation channel.
- In section 7, Network Controlled Repeaters (NCRs) are introduced. NCRs aim to be a low cost solution to overcome the reduced coverage capability of mm-Wave signals. An example of link budget calculation is also carried out to derive the typical specifications for an NCR antenna array.
- In section 8, the objectives and specifications for this thesis work are stated.
- In section 9, the design process of the radiating element will be described, starting at first with the analysis of a unit-cell and then with the array. To support this design phase, multiple simulations are carried out using the Ansys HFSS 3D electromagnetic (EM) simulation software.

4 Review of Antenna Parameters

While designing any kind of antenna, it is important to define some parameters that can effectively describe the general properties of the antenna. Antenna parameters are defined for both transmitting and receiving antennas. In the following, some of the most common parameters that will be used in this work are reviewed.

4.1 Spherical reference frame

Before starting, it is appropriate to define the reference frame that will be used all along this thesis work. The *spherical reference frame* is defined by three mutually orthogonal unitary vectors: $\hat{r}, \hat{\theta}, \hat{\phi}$.
Vector $\hat{r}$ is radial, therefore orthogonal at any point on the surface of the sphere that has radius r and is centered in the origin.
Vectors $\hat{\theta}$ and $\hat{\phi}$ are instead tangent to the spherical surface at any point.

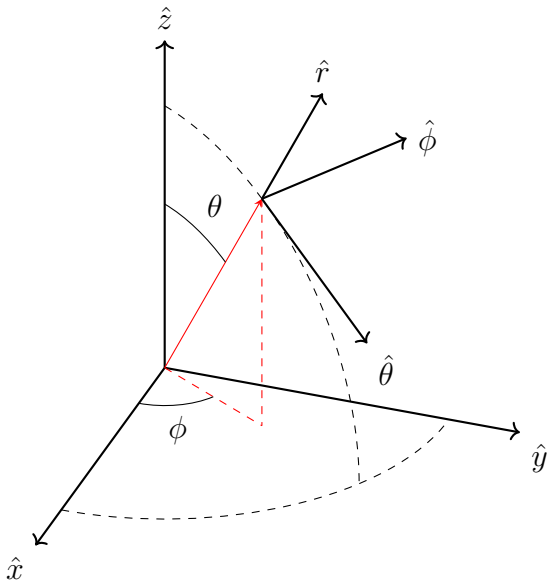

Figure 4.1: Spherical reference frame.

It is possible to move from the spherical reference frame to the cartesian reference frame through the following basis transformation:

$$\begin{bmatrix} \hat{r} \\ \hat{\theta} \\ \hat{\phi} \end{bmatrix} = \begin{bmatrix} sin(\theta)cos(\phi) & sin(\theta)sin(\phi) & cos(\theta) \\ cos(\theta)cos(\phi) & cos(\theta)sin(\phi) & -sin(\theta) \\ -sin(\phi) & cos(\phi) & 0 \end{bmatrix} \begin{bmatrix} \hat{x} \\ \hat{y} \\ \hat{z} \end{bmatrix} \tag{1}$$

To be noted is that the change of basis matrix is orthonormal, thus the inverse matrix is equal to the transposed one. This property can be useful when cartesian coordinates are required starting from the spherical ones.

4.2 Radiation patterns

Depending on how the antenna is designed, it will have its own characteristic radiation properties. Suppose an antenna radiates an electric field given by the following expression:

$$E_{rad} = E(r, \theta, \phi) \, . \tag{2}$$

Then, we can define the *normalized field pattern function* as:

$$F(\theta, \phi) = \frac{E(r, \theta, \phi)}{E(r, \theta_{max}, \phi_{max})} \, , \tag{3}$$

where $E(r, \theta_{max}, \phi_{max})$ is the maximum radiated field, in terms of magnitude, that is generated by the antenna at the coordinates $(r, \theta_{max}, \phi_{max})$. To be noted is that $F(\theta, \phi)$ does not depend on the radial distance r.
One can also refer to the *normalized power pattern function*, which is simply defined as:

$$|F(\theta, \phi)|^2 = \frac{|E(r, \theta, \phi)|^2}{|E(r, \theta_{max}, \phi_{max})|^2} \, . \tag{4}$$

The previous definitions can be used to realize the so called *radiation pattern plots*, that can be obtained by plotting in spherical coordinates the surface given by:

$$\mathcal{P}(\theta, \phi) = \big[|F(\theta, \phi)|, \theta, \phi \big] \, . \tag{5}$$

4.2.1 Half-Power Beam Width (HPBW)

The half-power beam width of an antenna is defined as the angular region between two points whose power level is halved with respect to the point of maximum radiation. The angles at which the power is halved can be found by imposing:

$$|F(\theta_{HP}, \phi_{HP})|^2 = \frac{|E(r, \theta_{HP}, \phi_{HP})|^2}{|E(r, \theta_{max}, \phi_{max})|^2} = \frac{1}{2}. \tag{6}$$

The given expression is equivalent to:

$$|F(\theta_{HP}, \phi_{HP})| = \frac{1}{\sqrt{2}}, \tag{7}$$

and the HPBW parameter is then computed as:

$$HPBW = |\theta_{HP}^{left} - \theta_{HP}^{right}|. \tag{8}$$

Alternatively, the HPBW is most easily computed graphically. In Figure 4.2, a normalized field pattern function $|F(\theta, \phi)|$ is used to find the half-power angles.

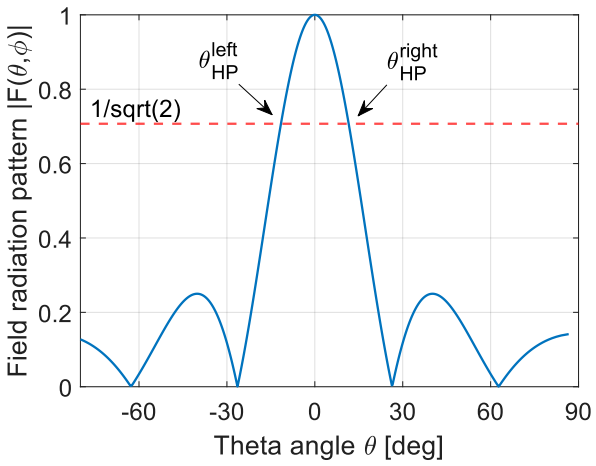

Figure 4.2: Example of a graphical HPBW calculation.

4.3 Directivity, gain and EIRP

The parameters of directivity and gain are used to describe how well an antenna can radiate in a particular direction. A highly directive (or high gain) antenna is used when a beam focused along a particular direction is required, for example in a point-to-point link. A less directive (or low gain) antenna, is better suited in all those applications where the radiated power is required to cover a larger area, like in a broadcast application.

4.3.1 Radiated power per unit solid angle

The *radiated power per unit solid angle* is defined as:

$$U(\theta,\phi) = I_R(r,\theta,\phi)r^2 = \frac{|E(r,\theta,\phi)|^2}{2\eta_0}r^2, \tag{9}$$

where $I_R(r,\theta,\phi)$ is the *radiated power intensity* $[W/m^2]$ and $\eta_0 = \sqrt{\frac{\mu_0}{\varepsilon_0}} = 120\pi$ $[\Omega]$ is the *free-space characteristic impedance*.
In the direction of the mainlobe we can also define:

$$U_m = U(\theta_{max},\phi_{max}) = \frac{|E(r,\theta_{max},\phi_{max})|^2}{2\eta_0}r^2. \tag{10}$$

If we recall equation (4), after rearranging the terms we can write a more compact form:

$$U(\theta,\phi) = U_m|F(\theta,\phi)|^2. \tag{11}$$

If an *isotropic antenna* existed, then its radiated power would be uniformly distributed in all directions, meaning that:

$$U_{isotropic}(\theta,\phi) = U_{avg} = \frac{P}{4\pi}, \tag{12}$$

where P is the total power radiated by the antenna.

4.3.2 Directivity

The *directivity* is defined as the ratio of the maximum to the average radiated power per unit solid angle:

$$D = \frac{U_m}{U_{avg}} = \frac{U_m/r^2}{U_{avg}/r^2} = \frac{1}{P}\left(4\pi r^2 \frac{|E(r,\theta_{max},\phi_{max})|^2}{2\eta_0}\right) = \frac{EIRP}{P}, \tag{13}$$

where, again, P is the total power radiated by the antenna.
In the ideal case of an isotropic antenna it holds that $U_m^{isotropic} = U_{avg}^{isotropic}$, therefore one would obtain that its directivity $D_{isotropic} = 1$. In reality, no such isotropic antenna can be realized and in practice it is always $D > 1$.
The directivity of an antenna can also be expressed in relation to that of a reference antenna. In the previous definition it is implicit that the reference antenna is the ideal isotropic one. When the reference is the isotropic antenna, it is common practice to report the directivity value in terms of dBi, where the "i" stands for *isotropic*.

$$D_{dBi} = 10 \cdot log_{10}\left(\frac{D}{D_{isotropic}}\right) = 10 \cdot log_{10}\left(D\right). \tag{14}$$

4.3.3 EIRP - Equivalent Isotropic Radiated Power

The *Equivalent Isotropic Radiated Power* (EIRP) is the power an hypothetical (ideal) isotropic antenna would radiate if it generated at a distance r the maximum electric field $|E(r,\theta_{max},\phi_{max})|$ of an antenna with directivity D.

$$EIRP = 4\pi r^2 \frac{|E(r,\theta_{max},\phi_{max})|^2}{2\eta_0}. \tag{15}$$

4.3.4 Gain

If the definition of *directivity* (D) is well defined from a theoretical point of view, it is in practice a difficult task to measure the *total radiated power* (P). It is instead easier to measure the active power that is entering (feeding) the antenna. We can define the active power entering the antenna as the *input power* P_{in}. Then, the *antenna gain* can be written as:

$$G = \frac{EIRP}{P_{in}}. \tag{16}$$

It is also possible to report the antenna gain in dBi:

$$G_{dBi} = 10 \cdot log_{10}\left(\frac{EIRP}{P_{in}}\right) = EIRP_{dBm} - P_{in[dBm]}, \tag{17}$$

and rearranging the terms one can also obtain that:

$$EIRP_{dBm} = G_{dBi} + P_{in[dBm]}. \tag{18}$$

4.3.5 Radiation efficiency

The *input power* P_{in} that is entering the antenna is not totally converted into *radiated power* P. In fact, antennas are affected by ohmic losses and part of the input power is dissipated by the Joule effect. Some types of antennas are realized on dielectric substrates, which also contribute in dissipating a fraction of the input power. One can account for such losses by defining the *radiation efficiency*:

$$e_r = \frac{P}{P_{in}}. \tag{19}$$

To be noted is that $0 \leq e_r < 1$.
The radiation efficiency definition can be useful to obtain an important relation between *Directivity* and *Gain*, that is:

$$G = D \cdot e_r \ \ , \ \ G < D. \tag{20}$$

4.3.6 Realized gain

The *realized gain*, also referred to as *absolute gain* [2], takes into account the power reflected at the antenna input port due to impedance mismatch. Consider the following scheme:

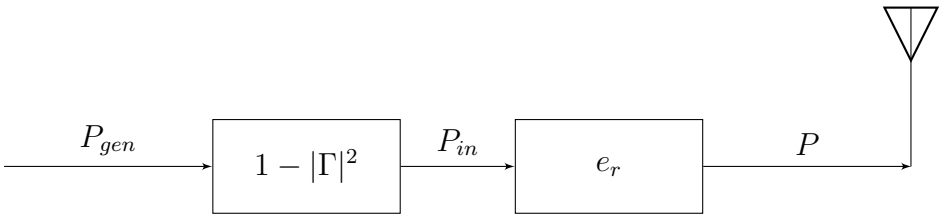

Figure 4.3: Schematic of power delivery to an antenna.

In Figure 4.3 the following quantities are defined:

- P_{gen} is the incident power coming from the generator that drives the antenna;
- The term $P_{in} = P_{gen} \cdot (1 - |\Gamma|^2)$ represents the power that is actually delivered to the antenna itself, after taking into account impedance mismatch. In fact, Γ is the reflection coefficient:

  $$\Gamma = \frac{Z_L - Z_C}{Z_L + Z_C}, \tag{21}$$

  where Z_L is the antenna input impedance and Z_C is the characteristic impedance of the transmission line the antenna is connected to. If the antenna was perfectly matched to the line, then one would obtain $\Gamma = 0$.
- The term $P = P_{in} \cdot e_r$ is the radiated power by the antenna after accounting for the losses that occur inside the antenna itself. The term e_r is the antenna radiation efficiency parameter that was previously discussed.

Finally, the *realized gain* or *absolute gain* is defined as:

$$G_{abs} = \frac{EIRP}{P_{gen}} = (1 - |\Gamma|^2) \cdot G, \tag{22}$$

where G is the antenna gain defined in equation (16).

4.4 Effective area

Any antenna can be associated with a value of *effective area*. This parameter can be used to describe the power capturing ability of the antenna. More precisely, the effective area is the ratio of available power at the terminals of a receiving antenna to the power flux density of a plane wave incident on the antenna from a given direction. If the direction is not specified, the direction of maximum radiation intensity is implied [2]. This definition can be translated into the form:

$$A_e = \frac{P_T}{W_i}, \tag{23}$$

where A_e is the *effective area* $[m^2]$, P_T is the power delivered to the load [W] and W_i is the incident power density of the incoming wave $[W/m^2]$.

4.5 The Friis Formula

Consider the following link that consists of a transmitter (TX) and a receiver (RX) separated by a distance r.
The proposed link will be analyzed under the following assumptions:

- each antenna is in the far-field of the other;
- the antennas are optimally oriented toward their respective mainlobe direction;
- the antennas are polarization and impedance matched.

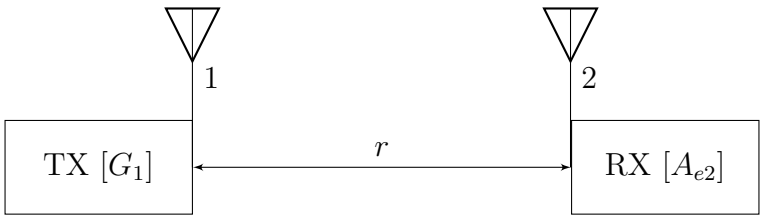

Figure 4.4: Example scheme of a TX-RX link.

In this setup, TX is supplied with an input power P_{in1} and has a gain G_1. The receiver has instead an effective area A_{e2}. The power received by RX can be computed as:

$$P_{r2} = A_{e2} \cdot \frac{|E_{1max}|^2}{2\eta_0} = \tag{24}$$

$$= A_{e2} \cdot \frac{EIRP_1}{4\pi r^2} = A_{e2} \cdot \frac{P_{in1} G_1}{4\pi r^2}. \tag{25}$$

Note that the term $\frac{|E_{1max}|^2}{2\eta_0}$ is the maximum power density generated by the TX antenna that is available in the position of the RX antenna but without the presence of the RX antenna itself. This is a simplified assumption, though it is acceptable for the purpose of this analysis.

Consider now **the same two antennas** but with their roles reversed, as shown in Figure (4.5):

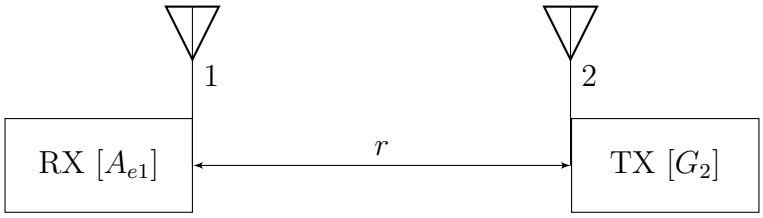

Figure 4.5: Example scheme of a RX-TX link.

The power received by RX is now:

$$P_{r1} = A_{e1} \cdot \frac{|E_{2max}|^2}{2\eta_0} = \tag{26}$$

$$= A_{e1} \cdot \frac{EIRP_2}{4\pi r^2} = A_{e1} \cdot \frac{G_2 P_{in2}}{4\pi r^2}. \tag{27}$$

At this point, under reciprocity conditions, if $P_{in1} = P_{in2}$ it must be $P_{r1} = P_{r2}$ and as such, it follows:

$$A_{e1} \cdot \frac{G_2 P_{in2}}{4\pi r^2} = A_{e2} \cdot \frac{P_{in1} G_1}{4\pi r^2}, \tag{28}$$

$$\frac{A_{e2}}{G_2} = \frac{A_{e1}}{G_1}. \tag{29}$$

Since equation (29) was found while considering two generic antennas, it is a general property that applies to any type of antenna. The effective area-to-gain ratio is a constant. Since this is a property that is independent from the type of antenna, it can be proven that calculating said ratio for the ideal dipole, one obtains:

$$\boxed{\frac{A_e}{G} = \frac{\lambda^2}{4\pi}}. \tag{30}$$

With this important relation, the expression of the received power by an antenna can be rewritten in the form of the *Friis Formula*:

$$P_{RX} = A_{eRX} \cdot \frac{G_{TX} P_{inTX}}{4\pi r^2}, \tag{31}$$

$$\boxed{P_{RX} = G_{RX} G_{TX} P_{inTX} \left(\frac{\lambda}{4\pi r}\right)^2}. \tag{32}$$

The term $\left(\frac{\lambda}{4\pi r}\right)^2$ is defined as the *free-space attenuation factor* and it will be further analyzed in the following sections.

5 Antenna Arrays and Beamforming

In some applications it is desirable to have a highly directive antenna that can precisely focus its beam in a particular direction. Usually, single antenna elements cannot achieve such high values of directivity. Antenna arrays are a type of antenna made of multiple radiating elements that are arranged in a particular geometrical configuration, like linear, rectangular, circular or others. The single-element can be any type of antenna. Ideally, assuming the coupling between elements is negligible, the total radiated field generated by the array is the vector addition of the single-elements' fields, due to the superposition of effects. The radiated fields of the single-elements should add up constructively in the desired direction and cancel out in the unwanted ones, thus generating a highly directive beam. When designing an array of identical elements, there are at least five fundamental parameters that can be used to shape the total radiation pattern [2]:

1. the geometry of the array (linear, rectangular, circular, etc.);
2. the excitation amplitude of each single element;
3. the excitation phase of each single element;
4. the relative positioning between elements;
5. the single element radiation pattern.

By properly working on the aforementioned parameters, one can influence the overall behaviour of the array. The following sections are dedicated to a brief revision of some basic theoretical concepts related to linear and planar arrays that were used in this work.

5.1 Uniform linear arrays

5.1.1 Array factor

Uniform linear arrays consist of N equally spaced single-elements that are aligned along a given particular axis, be it $\hat{x}$, $\hat{y}$ or $\hat{z}$, and are all excited with the same magnitude but with a progressive phase shift α. In Figure 5.1 an N-element linear array oriented along the $\hat{y}$ axis is showed as an example.

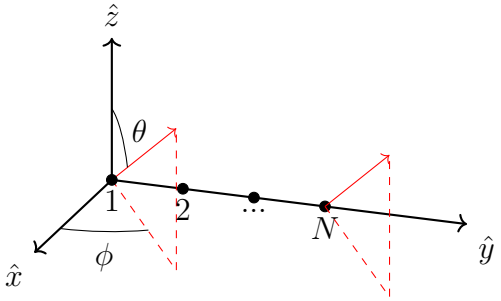

Figure 5.1: Linear array of N-elements aligned on the $\hat{y}$ axis.

Initially, consider the case in which two isotropic sources are aligned along the $\hat{y}$ axis and are separated by a distance d_y.

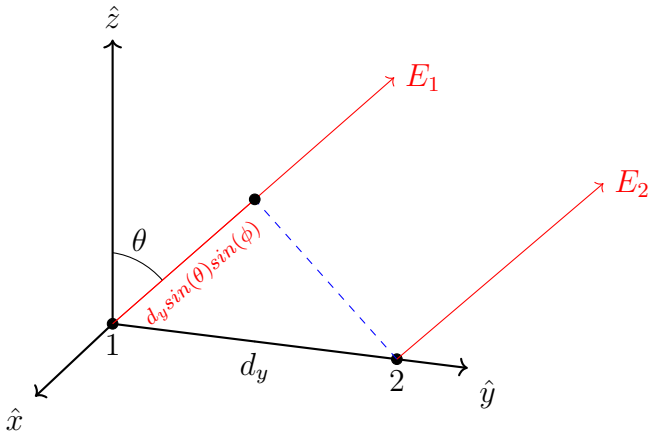

Figure 5.2: Linear array of two isotropic elements aligned on the $\hat{y}$ axis.

The total electric field radiated by the two sources, calculated in a far-zone point P, assuming no coupling between them, can be written as:

$$E_{tot} = E_1 + E_2 = CI_1 e^{-j\beta r} + CI_2 e^{-j\beta(r - d_y sin(\theta) sin(\phi))}. \tag{33}$$

As it can be observed in Figure 5.2, and assuming the observation point P is in the far-field, the wave arriving at source 1 has to travel an extra distance of $\Delta r = d_y sin(\theta) sin(\phi)$ compared to source 2, thus resulting in a phase difference of $\beta \Delta r$, where β is the free-space propagation constant. The terms I_1 and I_2 represent the excitation currents that are applied to the sources. Without loss of generality, they can be written as $I_n = |I_n| e^{j(n-1)\alpha}$. Since the elements are excited with the same signal magnitude, for simplicity $|I_1| = |I_2| = |I|$, therefore:

$$E_{tot} = C|I| e^{-j\beta r} + C|I| e^{j\alpha} e^{-j\beta(r - d_y sin(\theta) sin(\phi))} \tag{34}$$

$$= C|I| e^{-j\beta r} (1 + e^{j(\alpha + \beta(d_y sin(\theta) sin(\phi)))}). \tag{35}$$

Equation (35) allows to make a very important observation. The total far-zone electric field of a uniform two element array is equal to the product of the field generated by the source positioned at the reference point ($E_{ref} = E_1$), in this case the origin, and the array factor AF of that particular array:

$$E_{tot} = E_{ref} \cdot AF. \tag{36}$$

This is referred to as the *pattern multiplication principle* and, although it has just been derived for a two-element array, it also holds for an N-element array.
The *array factor* (AF) for a two element uniform linear array is therefore defined as:

$$AF = 1 + e^{j(\alpha + \beta(d_y sin(\theta) sin(\phi)))}. \tag{37}$$

The extension to the case of N-elements aligned along the $\hat{y}-$axis is the following:

$$E_{tot} = E_1 + E_2 + ... + E_N \tag{38}$$

$$= CI_1 e^{-j\beta r} + CI_2 e^{-j\beta(r - d_y sin(\theta) sin(\phi))} + ... + CI_N e^{-j\beta(r-(N-1)d_y sin(\theta) sin(\phi))} \tag{39}$$

$$= C|I|e^{-j\beta r}\left(1 + e^{j(\alpha+\beta d_y sin(\theta) sin(\phi))} + ... + e^{j(N-1)(\alpha+\beta d_y sin(\theta) sin(\phi))}\right). \tag{40}$$

Finally, the expression of the *array factor* for an N-element uniform linear array (along the $\hat{y}$-axis) is:

$$AF_{\hat{y}} = \sum_{n=1}^{N} e^{j(n-1)(\alpha+\beta d_y sin(\theta) sin(\phi))} = \sum_{n=1}^{N} e^{j(n-1)\psi_y}, \tag{41}$$

where $\psi_y(\theta, \phi) = \alpha + \beta d_y sin(\theta) sin(\phi)$ is a phase parameter that accounts for constructive and destructive interference effects in the far-field.

The same reasoning can be applied to arrays that have M-elements aligned along the $\hat{x}$-axis, separated by a distance d_x; in this case one obtains:

$$AF_{\hat{x}} = \sum_{m=1}^{M} e^{j(m-1)(\alpha+\beta d_x sin(\theta) cos(\phi))} = \sum_{m=1}^{M} e^{j(m-1)\psi_x}. \tag{42}$$

The array factor AF can be rewritten in a more convenient form, that is:

$$AF(\psi) = 1 + e^{j\psi} + ... + e^{j(N-1)\psi} \tag{43}$$

$$AF(\psi)e^{j\psi} = e^{j\psi} + e^{j2\psi} + ... + e^{jN\psi} \tag{44}$$

$$AF(\psi)e^{j\psi} - AF(\psi) = e^{jN\psi} - 1 \tag{45}$$

$$AF(\psi) = \frac{e^{jN\psi} - 1}{e^{j\psi} - 1} = e^{j\left(\frac{N-1}{2}\psi\right)} \cdot \frac{sin(N\psi/2)}{sin(\psi/2)}. \tag{46}$$

The *normalized array factor* is obtained by normalizing expression (46):

$$AF_n(\psi) = \frac{sin(N\psi/2)}{N sin(\psi/2)}. \tag{47}$$

Equation (47) can be employed to realize useful plots. Some examples are reported in Figure (5.3), in which single-elements are aligned along the $\hat{y}$-axis and are separated by a distance d_y.

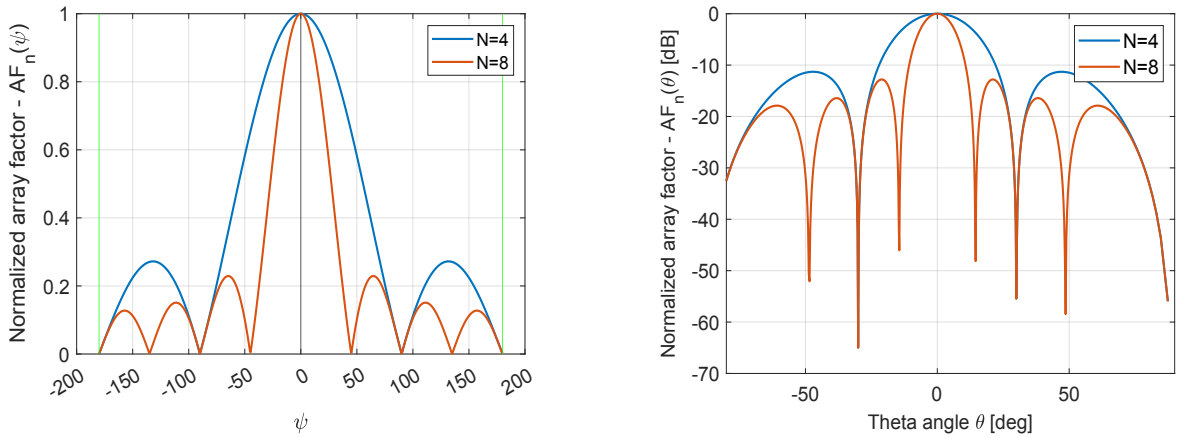

(a) Normalized array factor $AF_n(\psi)$.

(b) Normalized array factor $AF_n(\theta)$ [dB].

Figure 5.3: Normalized array factor - $d_y = 0.5\lambda_0$ - $\phi = 90°$.

At first glance we can observe that, if the number of elements increases, the mainlobe beamwidth becomes narrower and also more sidelobes (or secondary lobes) appear. Equation (47) is a periodic function of ψ. If we recall (41), or equivalently (42), we can observe that

$$\alpha - \beta d \leq \psi \leq \alpha + \beta d, \tag{48}$$

where, for notation simplicity, the term d is used to refer to the separation between single-elements. Equation (48) is defined to be the *visible region* of the array factor. The *visible region width* is instead defined as $2\beta d$. A full period is visible if $2\beta d = 2\pi$, that implies $d = \lambda/2$. If $d < \lambda/2$, less than a full period will be visible. On the other hand, if $d > \lambda/2$, more than one period will be visible. Figure (5.4) shows a normalized array factor plot when the distance between elements is λ, making the visible region of the array factor larger than one period.

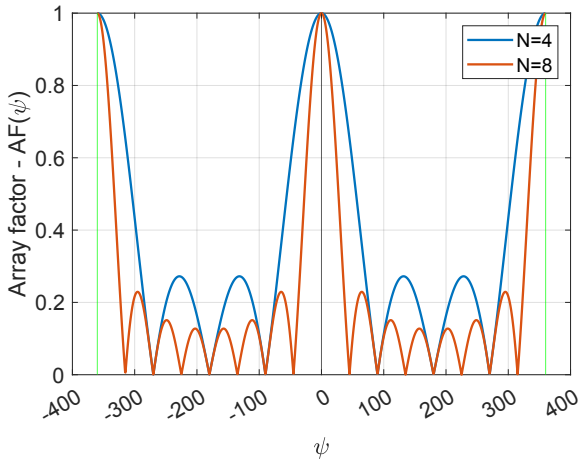

Figure 5.4: Normalized array factor - $d_y = \lambda_0$ - $\phi = 90°$.

To be noted is that other main-lobes could appear if the visible range of the array is larger than one period; it is common to refer to them as *grating lobes*. Grating lobes are generally not desired, therefore extra caution should be taken when choosing the spacing between array elements.

5.1.2 Main lobes of the array factor

The array factor function is maximized when $\psi = \psi_M = 2\pi N$, where $N = 0, \pm 1, \pm 2...$, under the condition that $\alpha - \beta d \leq \psi_M \leq \alpha + \beta d$. The main lobe is always found when $N = 0$, which is equivalent to $\psi = 0$. To avoid the presence of the grating lobes, one should guarantee that the other, higher order maximums are outside the visible region of the array. As an example, referring to a linear array with elements aligned along the $\hat{y}$-axis ($\phi = 90°$), the direction of the main lobe (N=0) can be computed as:

$$\theta_M = asin\left(-\frac{\alpha_y}{\beta d_y}\right). \tag{49}$$

5.1.3 Phased arrays

Equation (49) is used to compute the direction of the maximum given the phase shift between adjacent elements along the $\hat{y}$-axis, α_y, the propagation constant, β, and their separating distance, d_y. It is always possible to reverse such expression and compute the progressive phase shift α_y between consecutive elements that is required to steer the maximum in a particular desired direction θ_0. It follows that:

$$\alpha_y = -\beta d_y sin(\theta_0) sin(\phi)|_{\phi=90^\circ}. \tag{50}$$

Equivalently, for linear arrays aligned along the $\hat{x}$-axis, one would obtain:

$$\alpha_x = -\beta d_x sin(\theta_0) cos(\phi)|_{\phi=0^\circ}. \tag{51}$$

By properly controlling the phase of each single element in a linear array, one can achieve beam-steering capabilities. Depending on the alignment, linear arrays can only scan the beam along one plane, for example, the xz-plane for $\hat{x}$-oriented arrays, or the yz-plane for $\hat{y}$-oriented arrays.

5.2 Planar arrays

Planar arrays are an extension of linear arrays. When dealing with planar arrays, different geometries can be used. In this work, only rectangular planar arrays will be considered. In a rectangular geometry, single elements are aligned along two different axis, for example, M elements along the $\hat{x}-$axis and N elements along $\hat{y}-$axis, as shown in Figure 5.5.

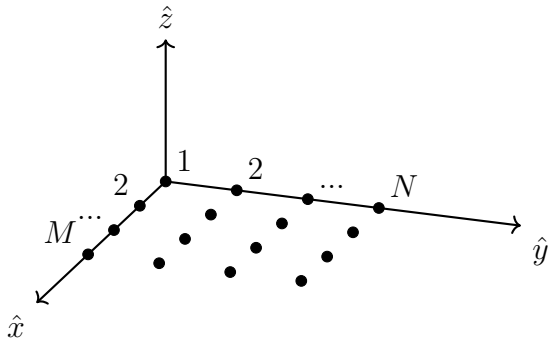

Figure 5.5: Planar array of $M \times N$-elements aligned on the $\hat{x}$ and $\hat{y}$ axes.

Planar arrays present some major benefits compared to linear arrays. These advantages include the capability of steering the main beam along both θ and ϕ. The increased number of elements yields larger gain and lower sidelobes. The major disadvantage is the increased number of elements itself, which makes the dimensions of the whole array substantially larger compared to linear arrays. The design procedure of a rectangular planar array is similar to the one that is used for linear arrays. In practice, since the elements are placed along the $\hat{x}$ and $\hat{y}$ axes, the array factor of a planar array can be formulated as the multiplication of the array factors of two linear arrays.

This is a direct application of the multiplication principle that was previously introduced:

$$AF^{planar} = AF_{\hat{x}} \cdot AF_{\hat{y}} = \sum_{n=1}^{N} \sum_{m=1}^{M} e^{j\left((m-1)\psi_x + (n-1)\psi_y\right)}, \tag{52}$$

which can be rewritten in the normalized form as:

$$AF_n^{planar} = \left[\frac{sin(M\psi_x/2)}{Msin(\psi_x/2)}\right] \cdot \left[\frac{sin(N\psi_y/2)}{Nsin(\psi_y/2)}\right], \tag{53}$$

$$\psi_x(\theta, \phi) = \alpha_x + \beta d_x u \text{ where } u = sin(\theta)cos(\phi), \tag{54}$$

$$\psi_y(\theta, \phi) = \alpha_y + \beta d_y v \text{ where } v = sin(\theta)sin(\phi). \tag{55}$$

The terms α_x and α_y are the progressive phase shift between elements aligned along the $\hat{x}$ and $\hat{y}$ directions, respectively. Figure 5.6 shows an example of a planar (2D) array factor.

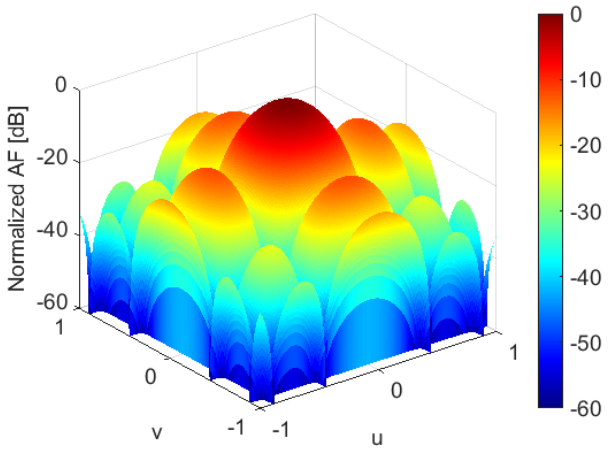

Figure 5.6: Example of normalized array factor from a 5×5 planar array.

To further extend this reasoning, it is possible to compute the required phase shift that each element in the planar array should have in order to steer the main-lobe toward a generic direction (θ_0, ϕ_0).
The *array scanning direction vector* $\hat{r_0}$, which points towards the mainlobe direction, and the *element position vector* r_{mn}, which instead points toward the specific (m,n) single-element in the array, can be defined as follows:

$$\hat{r_0} = \begin{bmatrix} sin(\theta_0)cos(\phi_0) \\ sin(\theta_0)sin(\phi_0) \\ cos(\theta_0) \end{bmatrix} \qquad \overline{r_{mn}} = \begin{bmatrix} (m-1)d_x \\ (n-1)d_y \\ 0 \end{bmatrix} \tag{56}$$

As it was previously shown, the progressive phase shift required to steer the beam along the $\hat{x}$-axis is given by equation (51):

$$\alpha_x = -\beta d_x sin(\theta_0) cos(\phi_0) = -\beta d_x \hat{x} \cdot \hat{r_0}. \tag{57}$$

While instead along the $\hat{y}$-axis, recalling equation (50):

$$\alpha_y = -\beta d_y sin(\theta_0) sin(\phi_0) = -\beta d_y \hat{y} \cdot \hat{r_0}. \tag{58}$$

Therefore, the phase shift to apply to the (m,n) single-element in the array is obtained with:

$$\boxed{\alpha_{mn} = (m-1)\alpha_x + (n-1)\alpha_y = -\beta \overline{r_{mn}} \cdot \hat{r_0}}. \tag{59}$$

By properly applying the just computed phase shifts to the single-elements in a rectangular planar array, 2D beam-steering can be achieved.

5.3 Beamforming

In the previous section it was shown that performing phase control on each single-element in an array enables beam-steering capabilities. This feature is also referred to as *beamforming*. Beamforming is a technique that allows to focus the radiated energy toward a specific direction. In the following, a brief overview of the possible available beamforming architectures are presented [3].

5.3.1 Analog beamforming

This beamforming architecture requires several components in the RF front-end such as: analog base-band, frequency generation, modulation and frequency conversion, power amplification and phase shifting [3].
Starting from the coded digital signal, the analog baseband converts it to a continuous time analog signal, using a digital to analog converter (DAC). After the conversion, a filtering stage is typically employed to remove higher frequency spectral components. The filtered analog signal is then used to modulate a high frequency carrier signal, that is defined as the Local Oscillator (LO). Typically, the LO signal is generated by a phase locked loop (PLL) that is connected to a highly precise, but lower frequency reference. The modulation is carried out by RF mixers. In some cases, modulation is applied in two steps: the first brings the baseband signal up to an intermediate frequency and the second takes the intermediate frequency and up converts it to RF. After that, the signal goes through the power amplifier and it is finally injected into the antenna element. Up to know, phase shifting was not mentioned. This is because, according to the position of the phase shifters, we can further identify three more categories:

- Analog RF beamforming
  Phase shifters are positioned in the RF domain, just before the amplification stage. In Figure 5.7 one phase-shifter per antenna is required, but only one Digital-to-Analog Converter (DAC) is used [3].

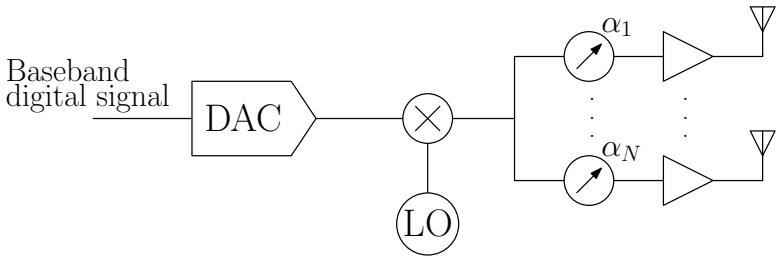

Figure 5.7: Analog RF beamforming - Block scheme.

- Analog IF/Base-Band beamforming
  Phase shifters are implemented in the intermediate frequency (IF) or base-band (BB) domain. Phase shifting at low frequencies is less critical and can be obtained with high resolution, low insertion loss, low power and small foot-print [3].

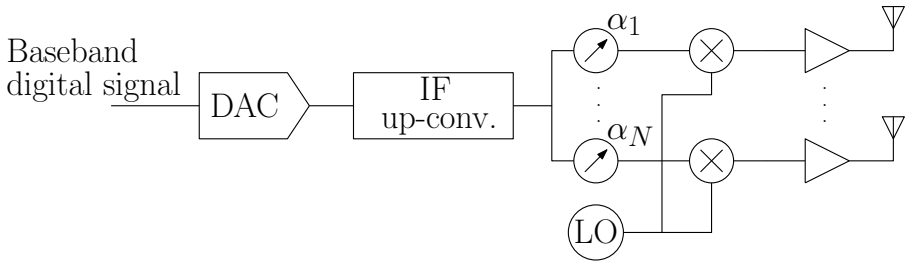

Figure 5.8: Analog IF beamforming - Block scheme.

- Analog LO beamforming
  Phase shifters are positioned in the LO domain. To be noted is that in this topology phase shifting is not implemented in the main signal path, thus relaxing the requirements on phase shifter's bandwidth and linearity [3].

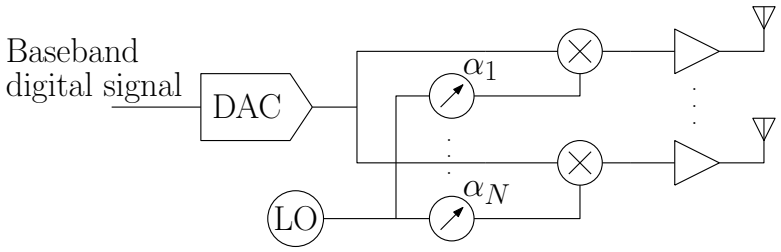

Figure 5.9: Analog LO beamforming - Block scheme.

5.3.2 Digital beamforming

In this architecture, phase shifting is carried out by a digital processor, which allows to have a greater control over each antenna element. The major advantage is the possibility to simultaneously direct beams in multiple directions at any given time. The main drawback is the increased power consumption that is due to the digital processor and to the DACs that are present on each RF chain (i.e. one DAC per antenna element) [3].

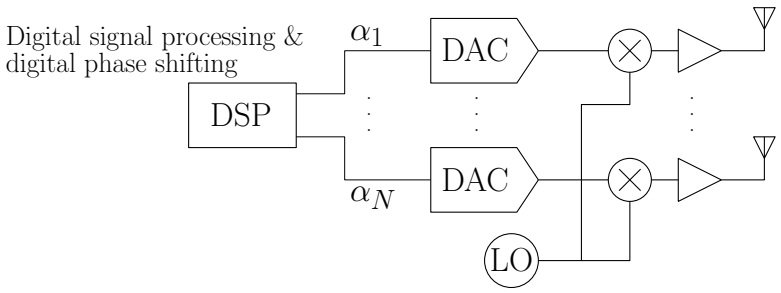

Figure 5.10: Digital beamforming - Block scheme.

5.3.3 Hybrid beamforming

This architecture combines both analog and digital beamforming [3]. There exist two primary types of hybrid beamforming designs:

- fully connected: every antenna is connected to every RF chain;
- partially connected: a group of antennas is coupled with an RF chain.

A digital precoder receives N_S input data streams. The N_S signals could represent data streams that are destined to different users. These streams are elaborated into N_{IF} signals and converted to the analog domain by a Digital to Analog Converter (DAC). Next, they are up-converted to an intermediate frequency before going through the analog beamformer, whose architecture could be, for example, the Analog IF that was previously presented. Compared to digital beamforming, in hybrid architectures the number of required RF chains (N_{IF}) is smaller than the number of antenna elements and only lower bounded by the number of data streams N_S that are to be transmitted. This not only reduces power consumption but also the overall system complexity.

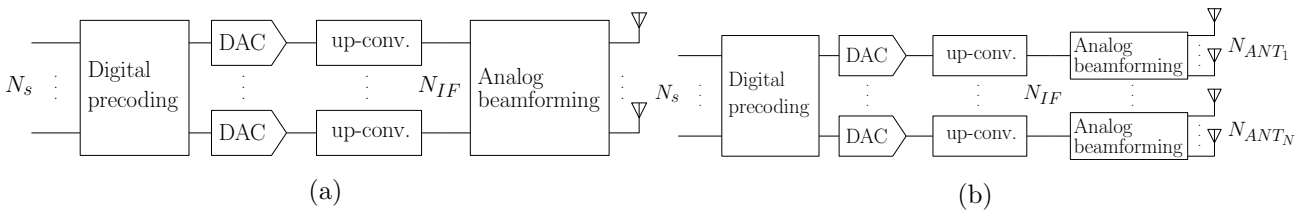

Figure 5.11: Hybrid beamforming - (a) fully connected and (b) partially connected architectures.

6 Introducing the mm-Wave band

The frequencies spanning from 30 GHz up to 300 GHz are termed as the *millimeter-wave* (mm-Wave) spectrum, since it has wavelengths in the order of 1 mm to 10 mm. Future networks are expected to provide data rates in the order of Gb/s. Services that take advantage of these rates require a large amount of bandwidth, which can be found in the mm-Wave bands. Frequencies between 24.25 GHz and 71 GHz are currently supported by the 3GPP 5G NR standard as well as IEEE 802.11ad,aj,ay [4]. The large spectrum availability is the key reason why a lot of research effort is spent into this new technology. Unfortunately, its adoption has not reached the expected scale so far. Wireless communications at mm-Wave are impaired by the propagation characteristics, which differ from today's more commonly used lower frequencies (below 6 GHz). Effects like path-loss and shadowing, together with other attenuation losses, become harsher as frequency increases. There are various possibilities and techniques to counteract these effects, but it is firstly necessary to understand the characteristics of the propagation channel. This is done through measuring campaigns in the real world, which provide valuable data so that channel models can be built upon it [5].

6.1 mm-Wave propagation characteristics

Compared to lower frequency signals, mm-Waves are more vulnerable to atmospheric effects, human shadowing and cannot propagate well through most materials. Taking account for these effects is of crucial importance while carrying out the channel modelling process. Before moving on to the analysis of various channel effects, it is worth to recall the Friis Formula, which will be useful to understand the following reasoning. In Section (4.5) it was found that the most common but simplified formulation of the Friis Formula can be written as:

$$P_r = G_r G_t P_t \left(\frac{\lambda}{4\pi d}\right)^2, \tag{60}$$

where P_r is the received power, G_r, G_t are the receiver and transmitter antenna gains, respectively, P_t is the transmitted power and the remaining term is defined as the *free-space attenuation factor*. This formulation assumes that the antennas are optimally oriented, that each antenna is in the far-field of the other and that they are impedance matched and polarization matched. Noted this, the formula can still give some very useful insights and is sufficient for an initial analysis of a wireless link.

6.2 Free-space attenuation

The *free-space attenuation* or *free-space loss* term embedded in the Friis Formula is defined as:

$$FSL = \left(\frac{\lambda}{4\pi d}\right)^2, \tag{61}$$

which can be conveniently rewritten in dB scale as:

$$FSL_{dB} = -10log(FSL) = 92.4 + 20log(d_{[km]}) + 20log(f_{[GHz]}). \tag{62}$$

From the last expression we can observe that the FSL_{dB} is proportional to both the distance ($d_{[km]}$) between the link points and also to the carrier frequency ($f_{[GHz]}$). Compared to the traditional lower frequency bands, moving to the higher frequencies of mm-Waves has an inherently worse (larger) FSL_{dB}. To better visualize this [5], two different plots are reported as an example: in Figure 6.1a the FSL_{dB} for different frequencies is reported as a function of the distance between the transmitting and receiving antennas, whereas in Figure 6.1b, the received power for different link distances is reported as a function of frequency.

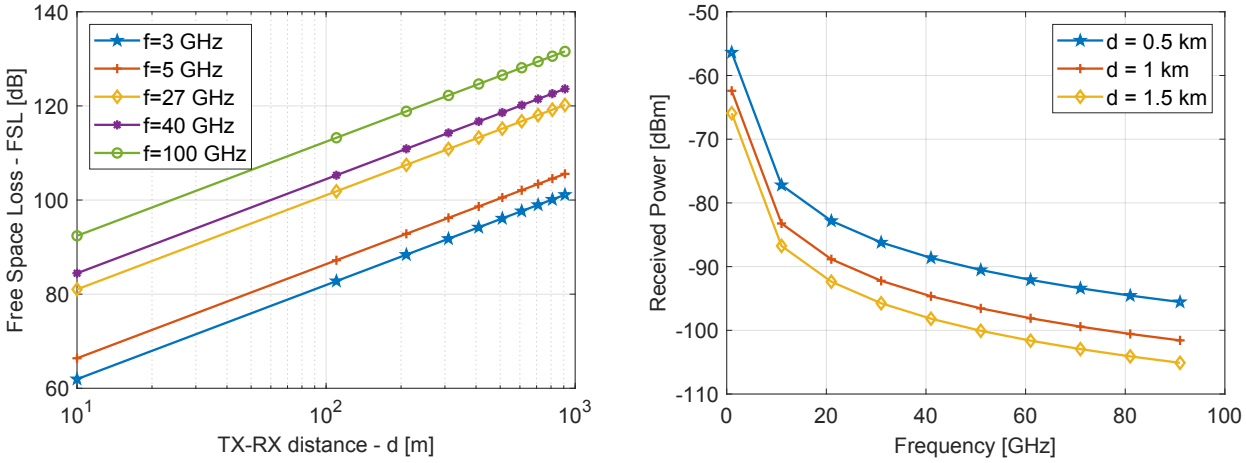

(a) (b)

Figure 6.1: (a) Free Space Loss (FSL_{dB}) over TX & RX distance. (b) Received power over frequency, $P_t = 10\,dBm$, $G_t = G_r = 10\,dBi$.

From the Friis Formula, one way to increase the received power is to increase the antenna gain (i.e. realizing a more directive beam). If we also recall the known relation between effective aperture and gain we have that:

$$A_{eff} = G\frac{\lambda^2}{4\pi} = \frac{G}{4\pi}\left(\frac{c}{f}\right)^2. \tag{63}$$

Therefore if the gain gets larger, it implies that also its effective aperture will increase. This is actually a simplified way to understand the effect of arrays: by properly arranging multiple antennas close together the total size and the effective area increase and this allows to achieve a higher gain. This makes antenna arrays very suitable to effectively counteract the increased propagation losses in the mm-Wave spectrum.

6.3 Atmospheric absorption

Another limiting factor is represented by the attenuation caused by gas molecules that are present in the atmosphere. When excited by electromagnetic waves, gas molecules absorb the incoming energy and turn it into vibrational energy. By nature molecules vibrate with a strength proportional to the carrier frequency [5]. The great part of this energy absorption is caused by oxygen molecules (O_2) and water vapors (H_2O). The carrier frequency is not the only factor determining the strength of gaseous absorption, but temperature, pressure and altitude are other parameters that contribute to this phenomenon.

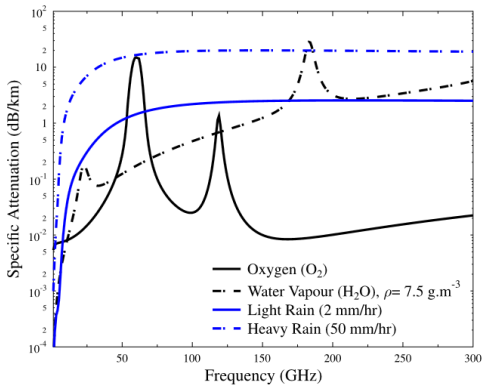

Figure 6.2: Specific attenuation curves of O_2, H_2O and rain at sea level [5].

Observing Figure 6.2, the absorption maximums for oxygen are found at the 60 GHz and 119 GHz frequencies, with loss values in the order of 15 dB/km and 1.4 dB/km, respectively. However, if short distance communications are considered, such absorption levels can be reduced significantly. For example, if the cell range is reduced from 1 km to 100 m, the O_2 attenuation for the same two previous frequencies reduces to 1.5 dB and 0.14 dB, respectively. In the end, the atmospheric attenuation can be considered negligible in short range communication links [5].

6.4 Rain-induced fading

The signal attenuation caused by the interaction of the propagating waves and the rain droplets becomes a significant matter when frequency increases. We can say that mm-Wave signals have wavelengths that are in the range of 1 mm up to 10 mm, while an average rain droplet has a size that is typically in the order of few millimeters. The comparable size between the two makes mm-Wave signals more vulnerable to rain blockage compared to larger wavelength signals. Looking again at the graph in Figure 6.2 we can observe the *specific rain attenuation* γ_{Rain} for a given rain rate R [mm/hr] as a function of frequency. The attenuation increases exponentially up to a critical frequency, after which its value settles. The attenuation curve can be modeled according to [5]:

$$\gamma_{Rain} = kR^{\alpha}, \tag{64}$$

where k and α are functions of the operating frequency and other parameters like temperature, polarization of the EM field, altitude and other factors. Two rain conditions are reported: 2 mm/hr and 50 mm/hr, representing a light and heavy rain downfall condition, respectively. In these two cases, the respective maximum attenuation recorded in the upper frequency bands of mm-Waves are 2.55 dB/km and 20 dB/km.
From this data we can learn that, much like atmospheric absorption, lower attenuation levels can be achieved if short-range communications are considered. This is another reason why the size of future communication cells is expected to be small.

6.5 Foliage attenuation

The presence of foliage between the transmitter and the receiver contributes to increase signal attenuation and to the worsening of the Quality of Service (QoS) of the wireless system. The degree of signal attenuation, which depends on the density of the vegetation, can be modeled with the following empirical formula [5]:

$$\gamma_{foliage[dB]} = \alpha f^{\beta} D_f^c (\theta + E)^{\varepsilon}, \tag{65}$$

where f [MHz] and D_f [m] are the carrier frequency and foliage thickness, while the terms $\alpha, \beta, c, \theta, E$ and ε are empirical parameters that depend on the model used. For example, using the ITU-R model and for foliage thicknesses smaller than 400m, the previous formula reduces to [5]:

$$\gamma_{foliage[dB]} = 0.2 f^{0.3} D_f^{0.6}. \tag{66}$$

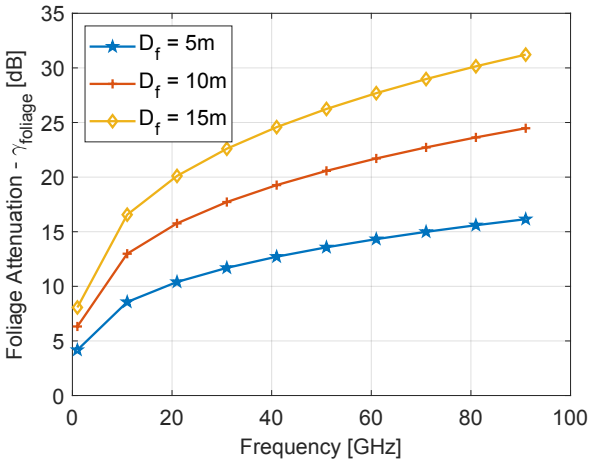

Figure 6.3: Foliage attenuation for different vegetation thicknesses.

The plot in Figure 6.3, which was obtained using equation (66), shows that for a foliage thickness of 10 m, the foliage attenuation at a 28 GHz frequency is estimated to be 17 dB, which is around 10 dB higher than sub-6 GHz frequencies. In recent measuring campaigns [5], foliage attenuation could be mitigated with the use of highly directive antennas for both the transmitter and the receiver devices.

6.6 Material interaction

Signals in the mm-Wave frequencies cannot propagate through obstacles such as furniture, doors and walls without being severely attenuated. Penetration losses have been quantified through measuring campaigns. This poses significant challenges in terms of coverage, especially when considering outdoor-to-indoor scenarios. In recent trials [5], it was shown that a 28 GHz signal was attenuated by 24.4 dB and 45.1 dB when going through two walls and four doors, respectively.

Typically, when an electromagnetic wave encounters a discontinuity between two different materials, part of the wave energy is reflected back into the material the wave originated from and the remaining part is instead refracted into the second material.

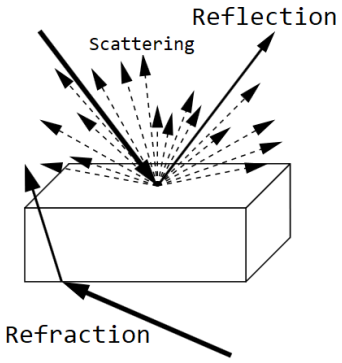

Figure 6.4: Ray-like wave propagation mechanism [5].

In Figure 6.4, the propagating EM waves are simplified and represented as rays, this allows an easier description of the propagation mechanisms. The reduced wavelength of mm-Wave signals introduces an additional effect. When these signals encounter small structural features that are close in size to the signal's wavelength, a diffused scattering is generated. This means that each reflected ray has a different reflection angle, thus signal power is scattered in many directions, generating the so called Multipath Components (MPCs). This is especially true when dealing with rough surfaces. Multiple studies based on measuring campaigns were carried out in the effort to discover the mm-Wave propagation mechanisms. For example, in NLoS scenarios it was shown that the link between TX and RX could successfully be established by relying on the reflected and the scattered (MPCs) components. Moreover, outdoor materials were discovered to be more reflective than indoor ones, making propagation in outdoor environments be greatly based on reflections. Previously, it was mentioned that highly directive antennas in the form of antenna arrays should be employed in mm-Wave systems to overcome the free-space loss. This means that the communication link consists of narrow and directional beams that limit the number of Multipath Components (MPCs) that are in the beam-range of the receiver antenna. This not only reduces multi-path interference but it also decreases the received power, which could potentially bring an outage to the link [5].

6.7 Human blockage

Another limiting factor to the propagation of mm-Waves is represented by human blockage. The presence of human bodies in between the transmitting and the receiving antennas can introduce an attenuation of up to $25\,dB - 30\,dB$ per person, as reported by measuring campaigns [5]. Interestingly, the severity of human induced attenuation is not proportional to the number of people, but it strongly depends on the configuration of the transmitting and receiving antennas. Notably, highly directive and beamsteering capable antennas showed that human blockage could be effectively mitigated. On the other hand, the presence of human bodies contributes to the generation of reflected waves that can yield an additional $1-2\,dB$ gain in the form of multipath

components (MPCs), as shown in the following Figure 6.5.

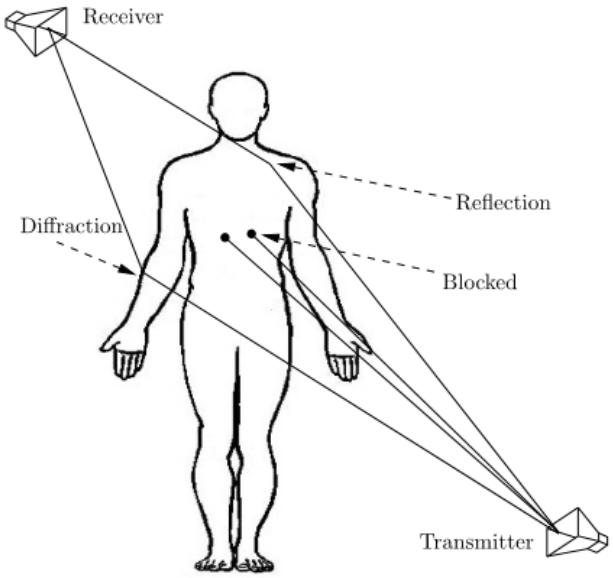

Figure 6.5: Human blockage [5].

6.8 Summary on measuring campaigns

While analyzing the mm-Wave propagation channel, many references to measuring campaigns were made. If it is important to know the elements that affect the mm-Wave channel, it is also valuable to perform real world measurements. This is a necessary step to have a full understanding of the channel. It is interesting to have a general overview of how measuring campaigns are carried out and, to this extent, a summary of the work carried out by a research group [4] from the *Politecnico di Milano* will be reported next. The aim of the aforementioned campaign is to directly compare the propagation characteristics of 5G sub-6 GHz and 5G mm-Wave signals. Two ad-hoc networks, one for the sub-6GHz and one for the 5G mm-Wave, were setup on the roof of a building in the university campus, in the same location, for a fair comparison. The User Equipments (UEs), together with other devices required for traffic generation, were placed inside a cart and carried around the campus site to perform cell coverage measurements. The campus represents a well suited urban environment to study LoS and NLoS propagation while also including effects like the blockage caused by buildings and trees. Before the real measurements, predictions were made using ray-tracing simulation tools. This phase can give extra insight on expected signal levels; the results of these simulations are given in terms of Reference Signal Received Power (RSRP), an indicator that represents the strength of the signal received by the UE. Ray-tracing tools can simulate the multiple propagation paths that result from refraction and reflections that occur with 3D-objects placed in the simulation environment.

The mm-Wave equipment used for the tests is fully standard-compliant and commercially available.

In Table 2 some relevant parameters of the mm-Wave setup are reported.

Base Station (gNB)	
Center Frequency	27.2 GHz
Channel bandwidth	200 MHz
Subcarrier spacing	120 kHz
Frame Structure	TDD 4:1 (D/U)
QAM order	256/64 (D/U)
TX power	37.5 dBm
TX antenna gain	32.5 dBi
TX EIRP	70 dBm
User Equipment (UE)	
UE antenna gain	20 dBi
UE EIRP	45 dBm

Table 2: Hardware specification for the mm-Wave measurement campaign [4].

The measurements were carried out using the following procedure:

1. Position the UE at the desired measurement point;
2. Perform two speed tests, one in downlink (DL) and one in uplink (UL), sequentially;
3. Measure the DL and UL speeds, also known as Key Performance Indicator (KPI), in 15-second windows;
4. Due to the receiver's antenna directivity, repeat the tests under a different direction. In this campaign, the test is repeated with the receiver antenna being oriented according to the four cardinal points.

The data collected during the measuring campaign can be used to produce plots like the one in Figure 6.6, which represents the Cumulative Distribution Function (CDF) of the measured downlink throughput and RSRP. The CDF of a random variable χ, evaluated at a value x, is the probability that χ will take values less or equal to x, that is $CDF(x) = P(\chi \leq x)$.

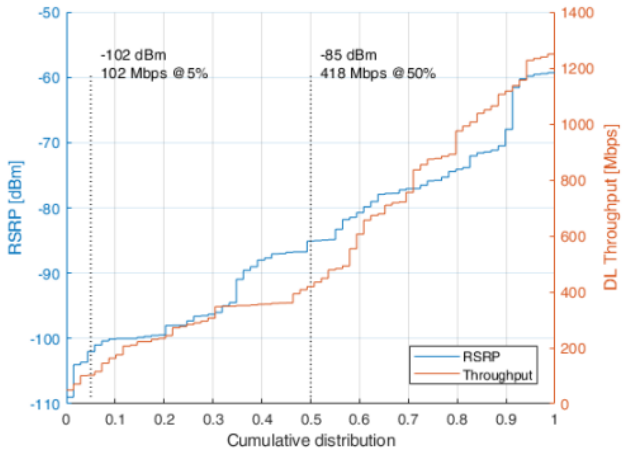

Figure 6.6: mm-Wave downlink throughput and RSRP CDF [4].

The general trend that can be observed and that one could expect is that for an increasing RSRP the throughput increases. This means that one can estimate the speed of the channel by evaluating the strength of the reference signal, the RSRP. In Table 3, data values related to the mm-Wave network and collected in some specific points during the measuring campaign are reported.

Test Point	gNB-UE Distance	LoS	DL [Mbps]	UL [Mbps]	RSRP
α	190m	✓	1239	235	-59 dBm
λ	285 m	×	708	0	-91 dBm
γ	315 m	×	355	17	-87 dBm
ζ	395 m	×	407	0	-96 dBm
ϵ	568 m	×	435	10	-95 dBm

Table 3: Specific test point measurements for mm-Wave [4].

At the end of the campaign, it was shown that the mm-Wave network suffers of a degradation in signal propagation. In some cases the mm-Wave UE even failed to connect to the base station while the sub-6GHz system, in the same position, could still provide half of its full capacity. mm-Wave signals show lower performance in severe NLoS scenarios. Instead, in favorable conditions, the two networks have comparable performance, with mm-Wave signals showing a potentially higher throughput in some cases.
The mm-Wave results of this campaign show that the best performance was achieved when the RSRP value, measured at the position of the UE, was around -59 dBm.

7 Network Controlled Repeaters (NCRs)

7.1 Overview

The deteriorated propagation characteristics that were previously discussed, make it a challenging task to *provide everyone everywhere* with a high quality of service (QoS). From measuring campaigns, it resulted that the main problem to overcome for mm-Waves is to guarantee network coverage. For this task, conventional RF repeaters represent a possible, cost-effective solution to extend coverage, although their ability to support network performance enhancing features, such as adaptive beamforming, dynamic gain and power adjustments are limited or not available. This is why Network-Controlled Repeaters (NCRs) are of great interest [6][7]. NCRs are low complexity network nodes whose function is to overcome coverage problems. They carry out the typical amplify-and-forward operation of traditional RF repeaters, but they also receive side control information from the base station (gNB), which allows more efficient operations. To better define the NCR functionalities, 3GPP initiated a group work in the effort to pinpoint the essential control information that are necessary for beamforming, uplink (UL) - downlink (DL) Time Division Duplex (TDD) and ON-OFF protocols. NCRs can be considered as network-controlled "beam benders" relative to the gNB. 3GPP has specified the characteristics of NCRs based on the following important assumptions [6]:

- NCRs are in-band RF repeaters used to extend network coverage on FR1 (5G sub-6 GHz) and FR2 (5G mm-Wave) bands.
- Only single-hop stationary NCRs are considered.
- NCRs are transparent to user equipment (UE).
- NCRs can maintain the gNB-repeater link and the repeater-UE link simultaneously.

7.2 NCR architecture

A possible, generalized, NCR block-scheme is represented in Figure 7.1. It can be observed that the NCR architecture consists of two functional entities: the NCR-MT and the NCR-Fwd.

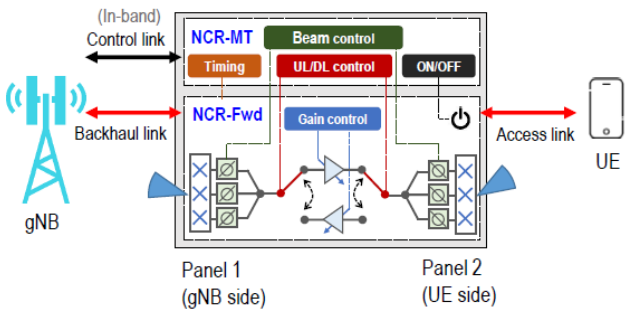

Figure 7.1: NCR architecture block scheme [6].

7.2.1 NCR-MT (Mobile Termination)

The NCR-MT (Mobile Termination) connects to the gNB via a control link (C-link) using the NR-Uu interface, which is the standard 5G interface that connects a generic UE to a gNB. The NCR links to its parent gNB as a standard device, while being identified as an NCR within the network. It also manages the exchange of side control information (SCI) to control the NCR-Fwd operations [6].

7.2.2 NCR-Fwd (Forwarding)

The NCR-Fwd (Forwarding) operates as an RF repeater: it relays uplink (UL) and downlink (DL) signals between the gNB and UEs using the backhaul and access links. The NCR receives a signal from the gNB in DL (or from the UE in UL). Within the NCR central stage, the signal is amplified and then transmitted to the UE in DL (or to the gNB in UL). The NCR does not carry out any signal processing on the relayed signal, therefore also noise is amplified and forwarded. The NCR-Fwd is controlled by side control information provided by the NCR-MT from the gNB. The NCR deciphers only the control information related to itself and ignores all of the UEs' data. The NCR-Fwd can be implemented with a central amplifying stage and two sets of array antennas: one for each the backhaul and access links. NCRs typically adopt analog beamforming, because it reduces the node complexity and it eliminates the need for the more advanced but power demanding digital beamforming [6].

7.3 Beam information

Either a fixed beam or an adaptive beam can be considered at an NCR for both the C-link and backhaul link. A fixed beam is simpler to implement and suitable in the case that the link between gNB and NCR is stable. An adaptive beam is instead a better solution for dense urban scenarios, in fact, an adaptive beam makes it possible to change the topology between gNBs and NCRs via air, a major benefit over the traditional fiber backhaul. In any case, both possibilities have their own benefits, and the discussion currently ongoing about this subject is moving towards making this option a feature up to NCR capability [8]. If adaptive beams are employed for both C-link and backhaul link, the determination of the best beam index can be accomplished through new signaling provided by the gNB. Another solution that does not require the gNB intervention requires a set of predetermined rules the NCR uses to select the appropriate beam.
In the access link, the NCR-Fwd provides adaptive beamsteering towards users for improved performance, compared to fixed-beam solutions. The access link for the NCR-Fwd is identified by a beam index. The proper index can be selected (indicated) in both a dynamic or a semi-automatic way. In a rapidly changing environment, that for example includes user mobility, the dynamic indication allows to quickly select the beam index that better suits the new conditions. Instead, the semi-static indication holds a stable beam configuration with less frequent adjustments. It is the gNB that specifies which time slots are to be allocated for a particular beam [6].

The gNB guides the NCR to perform periodic beam sweeping during the beam-training phase. The gNB may not have full knowledge of the NCR's beam characteristics but knows the NCR's number of supported beams. All of this process is transparent to the UE, which cannot differentiate between beams originating from the gNB or the NCR. The UE reports its preferred beam index based solely on the received Reference Signal Reference Power (RSRP), which is used for beam quality measurements. On the other hand, the gNB has full control over which gNB's TX beam and which NCR's TX beam index are adopted for transmission [6]. This concept is shown in Figure 7.2.

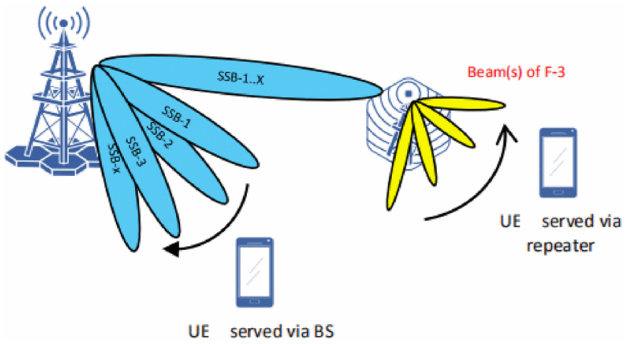

Figure 7.2: Concept of the NCR extending the gNB coverage [7].

7.4 Timing information (TDD)

In contrast to lower sub-6 GHz frequencies, mm-Wave bands only operate in Time-Division-Duplex (TDD) [1]. This means that both uplink (U) and downlink (D) symbols are transmitted on the same frequency but are multiplexed in the time domain. Depending on how symbols are arranged in time, 3GPP allows 61 predefined combinations, called *slot formats*. The availability of many slot formats makes 5G NR scheduling very flexible. In fact, combining different formats in sequence allows to adapt to changing transmission scenarios. A typical slot format always consists of 14 symbols, each of which can be dedicated to a different function: D is a downlink symbol, U is an uplink symbol, F is a flexible symbol. Flexible symbols can be dynamically allocated to either downlink, uplink or they can be reserved for other functions. For example, when a heavy downlink transmission is required, format #28 can be effectively used because most of the symbols are of the downlink type. Figure 7.3, shows such configuration:

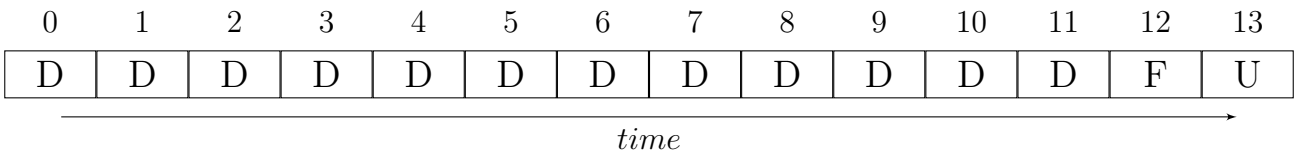

Figure 7.3: Slot format #28.

Figure 7.4 is instead an example of format #34, which prioritizes uplink transmissions:

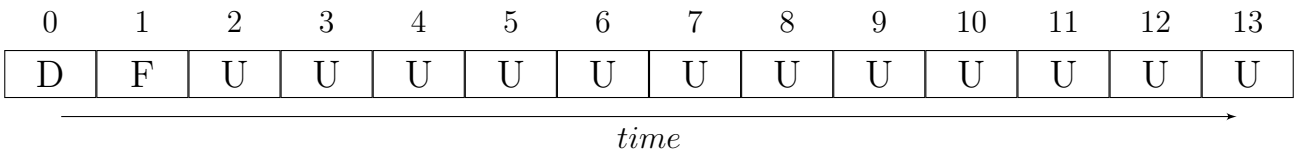

Figure 7.4: Slot format #34.

For what NCRs are concerned, the currently ongoing discussion about this topic [8] is moving towards having a semi-static TDD UL/DL configuration for NCR links. This means that the NCR will less frequently change the slot format structure. This allows to reduce the overall complexity and cost of NCR nodes. In any case, it is always the gNB that sends the slot format indication to the NCR-MT [7].

7.5 ON/OFF indication

ON-OFF information is used to turn the NCR off when it is not needed. This not only represents a power saving mechanism, but it can also be used to maintain a stable network performance across the cell users: the NCR can turn off for high RSRP users to avoid interference, and it can turn on for low RSRP users. The NCR-Fwd is by default assumed to be in the OFF state unless explicitly indicated by the gNB [6].

7.6 Variable gain control

As it can be observed in the block scheme of Figure 7.1, the NCR-Fwd central stage provides a gain control for both the UL and DL chains. The NCR-Fwd may receive signals from the gNB with different beams, thus the expected power is going to be variable depending on the selected backhaul beam. Moreover, the antenna gain is going to change for different steering angles. The variability of received power may result in poor network coverage. Therefore variable gain is used to compensate for antenna gain and/or received power variations.

7.7 An example of NCR-Fwd antenna array

This section highlights some of the features that the radiating element of an NCR should have in order to successfully extend coverage in mm-Wave networks.
In modern MIMO systems it is common to transmit the same signal using different polarizations. Given that in most wireless systems the strength of the received signal varies with time, by properly combining the differently polarized signal replicas the overall quality of the communication channel can be improved. This is also referred to as *polarization diversity* [9]. It is therefore common practice to provide the NCR with dual polarized radiating elements.
Another fundamental characteristic of an NCR is that it should be capable of beamforming, allowing it to steer the main radiation beam toward the desired user. A phased antenna array could be therefore employed for this task. Arrays can also provide highly directive beams, which are necessary to overcome the large propagation losses experienced by mm-Waves.
The radiating element should also satisfy other requirements, such as guaranteeing a reduced sidelobe level, the absence of the grating lobes and last but not least, it should be impedance matched to the RF devices it is connected to.
In Figure 7.5, a possible array layout is presented. It consists of dual polarized antennas in a 4×4 planar configuration. The H (horizontal) and V (vertical) polarization input signals are distributed using power dividers and feed the 2×4 beamformer ICs (BFICs); in this example each IC provides a total of eight outputs, four for each of the two polarizations. These integrated circuits carry out analog beamforming and can be controlled by a serial interface, for example SPI (Serial Peripheral Interface). This allows to manage both the phase shift and the amount of RF amplification applied to the input signals. Finally, the outputs of the ICs connect to the antennas' feed points. Although the proposed example is a 4×4 arrangement, it can be easily scaled up to larger size panels. Moreover, there is no restriction on which type of antenna that can be used as a unit-cell. For example, the unit-cell itself could be a sub-array of antenna elements.

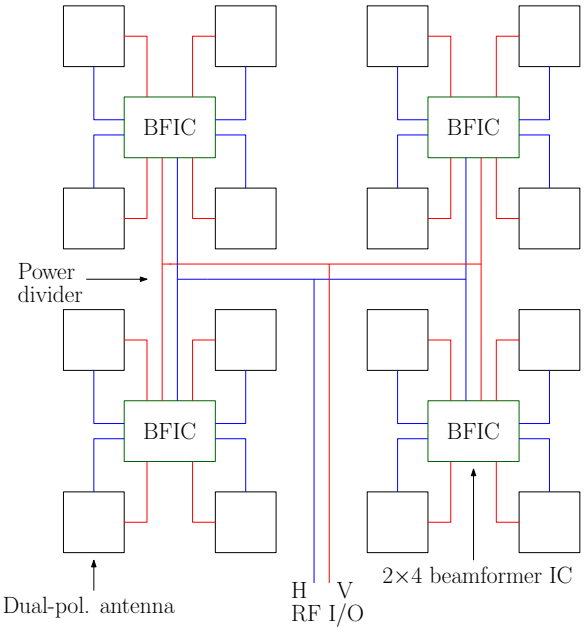

Figure 7.5: Example of a possible antenna array layout.

A beamforming IC (BFIC) receives at its input the RF signals for the H and V polarizations. The signals are then distributed to the various channels using power dividers. In the example above, each IC has eight channels: four are dedicated to the H polarization, the remaining ones for the V polarization. The ICs perform phase shifting and can also apply a variable gain on each RF chain. In Figure 7.6, a simplified architecture of an analog beamforming IC is shown as an example and for just the V polarization. An identical scheme could be also applied to the H polarization.

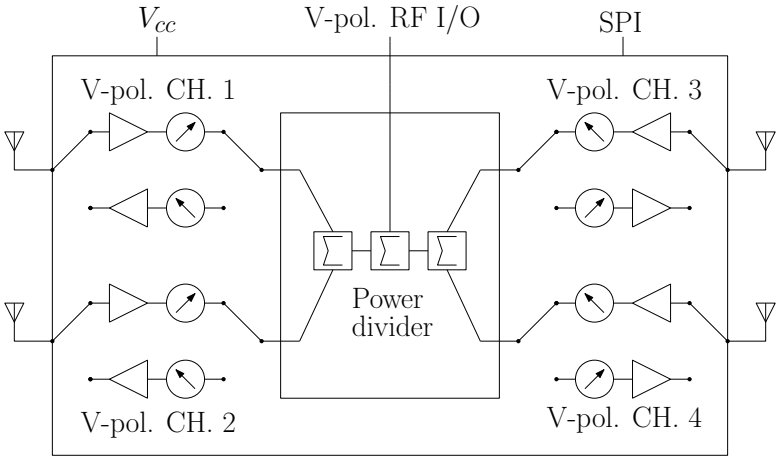

Figure 7.6: Example of a possible beamforming IC architecture.

7.8 Link budget analysis

In order to successfully establish a wireless link, the transmitted and received power should be adjusted to achieve the desired network performance. This power balance relies on the link budget, which considers the characteristics of the base station (gNB) and of the user equipment (UE) in terms of transmitted/received power and antenna gain. The following example of link budget calculation mainly focuses on extracting some relevant information regarding the characteristics an NCR should have in order to overcome the coverage gap that would exist between gNB and UE if the NCR was not present.
In this example, there are some important assumptions and details that will be listed in the following:

1. the distance between gNB and UE is fixed to $d_{link} = d_1 + d_2 = 400\,m$. The position of the NCR is set to be at $d_1 = 350\,m$ from the gNB, with a clear LoS, while it is at a $d_2 = 50\,m$ distance from the UE location, this time under a NLoS condition.

2. The gNB and UE devices are chosen before hand and they are representative of a possible real-world deployment. This means that the gNB transmit power, the gNB and UE antenna gains are fixed. Their values are reported in the following.

3. Instead of using the free space attenuation formula to compute the path loss, real world data from the measuring campaign in [4] is used.

Figure 7.7 presents the communication scenario under analysis:

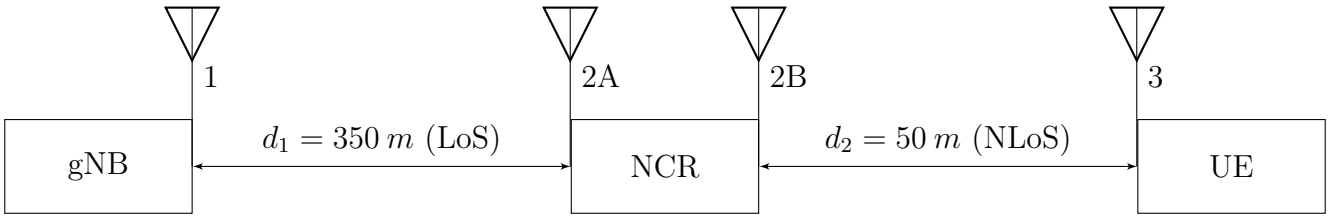

Figure 7.7: Communication link scenario.

The objective is to properly size the NCR antenna array by computing the required number (N) of array unit-cells and their antenna gain (G_{elem}). The calculations are based on the following known quantities:

1. the gNB transmit power ($P_{gNB}^{TX} = 35\,dBm$) and antenna gain ($G_{gNB} = 29\,dBi$);
2. the UE antenna gain ($G_{UE} = 0\,dBi$);
3. the real world measured path loss values between gNB-NCR ($PL_{NCR}^{gNB} = 124\,dB$), and between NCR-UE ($PL_{UE}^{NCR} = 106\,dB$);
4. the gain provided by the central stage of the NCR-Fwd ($G_{NCR}^{center} = 36\,dB$) and by the BFICs ($G_{BFIC} = 18\,dB$);
5. the desired power level at the UE location ($P_{UE} = -64\,dBm$).

	Link budget calculation	unit	value	details
(1)	gNB TX power	dBm	35	P_{gNB}^{TX}
(2)	gNB antenna gain	dBi	29	G_{gNB}
(3)	gNB EIRP	dBm	64	(1)+(2)
(4)	Path Loss (PL) @ 350 m LoS NCR Location	dB	124	PL_{NCR}^{gNB} Path loss between gNB and NCR location
(5)	RX power at NCR on gNB side	dBm	-60	P_{NCR}^{RX} = (3)-(4)

Table 4: Link budget calculation.

Figure 7.8 shows how the power inside an NCR-Fwd is distributed: from the antenna arrays, passing through the BFICs and the NCR central stage. It is assumed that the NCR antenna arrays on both the gNB and UE sides are identical.

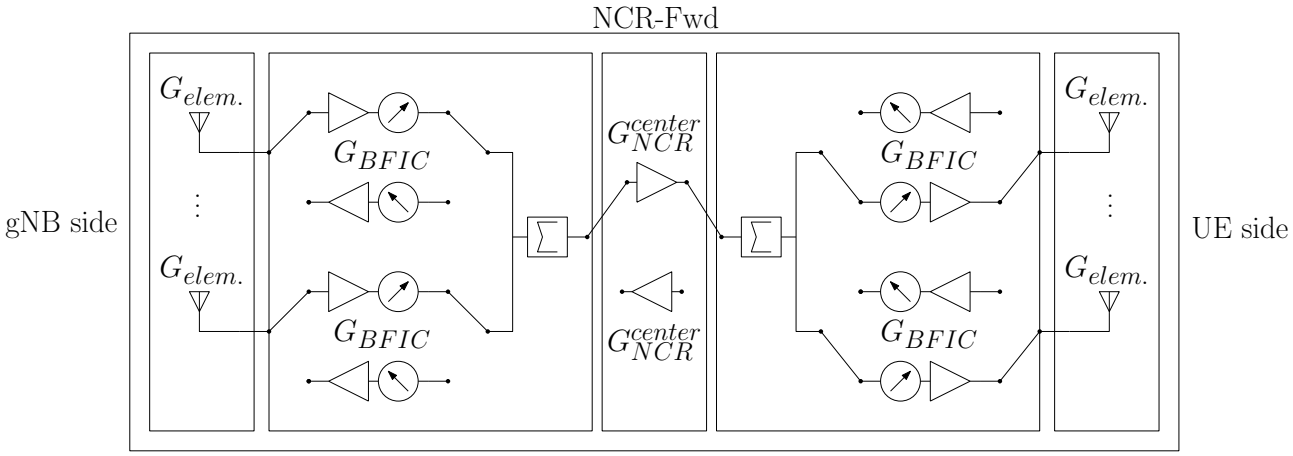

Figure 7.8: Power distribution inside the NCR-Fwd.

The received power P_{NCR}^{RX} that is available at the NCR location on the gNB side is collected by every antenna element in the array. The output power of each RF chain is P_{RF} and it takes into account that each antenna element has a gain G_{elem} and that the amplification provided by the BFIC is G_{BFIC}:

$$P_{RF} = P_{NCR}^{RX} + G_{elem.} + G_{BFIC}. \tag{67}$$

All the RF chains are then combined together. Depending on the total number N of antennas in the array, and assuming each antenna is directly connected to a BFIC channel as in Figure 7.5, the total combination gain is equivalent to $|AF| = 10log_{10}(N)$. After the combiner there is the *NCR center*, which represents an additional amplification stage with gain G_{NCR}^{center}. The total power exiting the *NCR center* and feeding the array panel on the UE side is P_{NCR}^{UE}:

$$P_{NCR}^{UE} = P_{RF} + |AF| + G_{NCR}^{center}. \tag{68}$$

On the UE side, power is once more distributed to all the BFICs, amplification for each RF chain takes place again and, in the end, a power P_{rad} is radiated by the array.

$$P_{rad} = P_{NCR}^{UE} + G_{BFIC} + G_{elem.} = \tag{69}$$

$$= P_{NCR}^{RX} + 2 \cdot G_{elem.} + 2 \cdot G_{BFIC} + |AF| + G_{NCR}^{center}. \tag{70}$$

(6)	NCR UE-side transmitted power	dBm	P_{rad}	
(7)	Path Loss (PL) @ 50 m NLoS UE Location	dB	106	PL_{UE}^{NCR}
(8)	UE received power	dBm	-64	P_{UE} = (6)-(7)

Table 5: Link budget calculation - continued.

Finally, plugging the known values, it is possible to obtain that the power received at the position of the UE is P_{UE}:

$$P_{UE} = P_{rad} - PL_{UE}^{NCR} = \tag{71}$$

$$= P_{NCR}^{RX} + 2 \cdot G_{elem.} + 2 \cdot G_{BFIC} + |AF| + G_{NCR}^{center} - PL_{UE}^{NCR} = \tag{72}$$

$$= -94\,dBm + 2 \cdot G_{elem.} + |AF|, \tag{73}$$

where $G_{BFIC} = 18\,dB$, and $G_{NCR}^{center} = 36\,dB$ are given as known values. For example, if the array was made of conventional microstrip patch antennas and their gain was supposed to be $G_{elem.} = 6\,dBi$, then an $N = 8 \times 8$ array, which can provide a maximum array factor of $|AF| = 10log_{10}(8 \times 8) = 18\,dB$, would be adequate to reach the desired requirement. In fact, with these assumptions one obtains that:

$$P_{UE} = -94\,dBm + 2 \cdot G_{elem.} + |AF| = -64\,dBm, \tag{74}$$

and in the end total array gain is:

$$G_{array} = G_{elem} + |AF| = 6\,dBi + 10log_{10}\,(8 \times 8) = 24\,dBi. \tag{75}$$

This analysis provided a general design guidance that allowed to compute the size of the array and the gain that the unit-cell should have in order to guarantee the desired power level at the position of the UE.

8 Project Specifications

After exploring the characteristics of NCR antenna arrays in Section 7 and after carrying out the link budget for a real world communication scenario in Section 7.8, it is now possible to write down the project specifications for a radiating element intended to be implemented in an NCR.

Parameter	Value	Details
Frequency Band	26.5-27.5 [GHz]	reflection coefficient $S_{11} < -10\,dB$
Realized Gain	24 [dBi]	peak realized gain broadside at 27 GHz
Side Lobe Level	-10 [dB]	no grating lobes allowed
Polarization	dual-linear	H,V polarizations
Beam Scanning	$\pm 60°/\pm 60°$	azimuth/elevation, for both H,V
Scan Loss	<4 dB	at max. scan angle

Table 6: Project Specifications.

The main objective of this thesis work is to study how to satisfy at the same time the beam scanning and the scan loss requirements. It is not trivial and generally not common to achieve such a large scanning requirement in both the elevation and azimuth planes. Arrays that can meet such requirement are often defined to be *wide-angle scanning*. Possibly, the array should cover the whole scanning region while minimizing the scan losses at large angles and suppressing the grating lobes. In this case, the aim is to investigate how to maintain the scan-loss in the neighbourhood of $3\,dB$ or in any case $< 4\,dB$ at the maximum scan angle.
Given the computational effort required to simulate large finite arrays, and in the light of the available hardware resources allocated to the simulation software, the requirement related to array gain will be of lower priority. This means that the size of the arrays that will be analyzed in this work will be limited to a maximum of a 5×5. Indeed, if all the other requirements are satisfied, one can increase the array gain to reach the target by increasing the number of unit-cells in the structure.

9 Design Process

9.1 Wide-angle scanning phased arrays

The study of wide-angle scanning phased arrays (WASA) has been an ongoing research topic and it represents a challenging task. The wide-angle feature is usually interpreted as an angular coverage larger than 100° (i.e. a $\pm 50°$ scan). The difficulty level is due to the large number of degrees of freedom and to the combination of multiple requirements that need to be satisfied at the same time. When dealing with scanning arrays, the most desired feature is being able to steer the main beam toward a given direction in a wide angular region, while maintaining good impedance matching and keeping the antenna gain as high as possible. This is in contrast with what actually happens: impedance matching changes and the antenna gain decreases for increasing scan angles.
The varying input impedance as a function of the scan angle could bring to a condition called *scanning blindness*, that is when the reflection coefficient (Γ) approaches unity and all the input power is reflected back from the array to the generator due to impedance mismatch. Guaranteeing good levels of matching at large scan angles is not trivial.
There are therefore two major issues that need to be addressed.
The first one is related to the *scan-loss*, which is the reduction of gain with the varying scanning angle. In a relatively large planar array, the array directivity can be approximated with the following generalized equation [10]:

$$D = \frac{32400 \cdot cos(\theta_0)}{\theta_{x3}\theta_{y3}}, \tag{76}$$

where θ_{x3} [°] and θ_{y3} [°] are the 3-dB beamwidth (HPBW) of the array in the principal planes ($\phi = 0° \ \& \ \phi = 90°$) at broadside and θ_0 is the angle the beam is scanned to. This general equation reveals that the array directivity approximately decreases as the cosine function for an increasing scan-angle. Recall now the definition of *realized gain* given in equation (22). It can be rewritten in the form:

$$G_{abs} = (1 - |\Gamma|^2)D \cdot e_r. \tag{77}$$

Ideally, if the array was perfectly matched (i.e. $\Gamma = 0$), then the realized gain would only depend on the pattern characteristics of the array through the directivity term D. In practice, both the directivity D and the reflection coefficient Γ vary as a function of the scan angle. It is therefore convenient to combine both factors into one and approximate the scan-loss in the form of some power of the cosine $(cos\theta)^n$. Reasonable design goals are for $n = 1$, 3/2 and 2 [10]. Clearly, the most desirable condition would be to have the scan-loss behave as per $n = 1$. This can be usually obtained only for one plane of scan, either $\phi = 0°$ or $\phi = 90°$. It is challenging to achieve it for both planes. Generally, it is common practice to assume that the scan-loss behaves as $(cos\theta)^{3/2}$ in both planes [10]. As an example, consider an 8-element linear array with a uniform spacing of $0.45\lambda_0$ between them. Recalling that the total array pattern is the product of the array factor with the element pattern, and assuming the element normalized power pattern to be approximated as $(cos\theta)$, the following Figure 9.1 shows the total array power pattern normalized to the broadside condition and for different angles of scan.

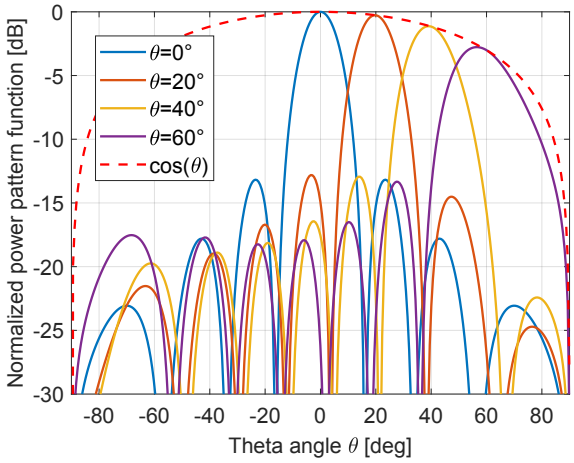

Figure 9.1: Array patterns at different scanning angles - N = 8 - $d = 0.45\lambda_0$.

As the main beam moves away from broadside, its gain decreases at the rate of the element pattern [11]. For this reason, in order to mitigate the scan-loss, it is important for the single element to have a wide HPBW, which should be comparable or even larger than the desired scanning range. Traditional antenna elements with a broadside radiation pattern have in general a limited HPBW, and their gain decreases significantly as the angle deviates from broadside: this directly translates into a limited scanning capability of the array.

The second issue is instead related to the mutual coupling between adjacent elements in the array. In general, when multiple antennas are near each other, whether they're transmitting or receiving, some part of the energy that was intended for one antenna will inevitably reach the others. This effect is defined as mutual coupling. The amount of coupling is primarily determined by the: [2]

1. radiation characteristics of the elements;
2. separation among elements;
3. relative orientation between elements.

All these parameters influence the array performance by varying the element impedance, reflection coefficients and the overall antenna pattern. The behavior that is observed for an isolated element is quite different from the one when the same is inside the array. For example, element patterns and gain vary across the array, with elements on the edge behaving in a different way compared to those in the center [10]. About the element impedance, it is necessary to introduce the following definitions [2]:

1. antenna impedance: the impedance of the isolated antenna unit-cell;
2. active impedance: the impedance of a unit-cell inside an array with all the other elements excited.

The unit-cell *active impedance* depends on mutual coupling and on the relative excitation of each element in the array. It can be evaluated using the following relations [2].
Consider a $M \times N$ planar array where each element is identified with an index mn. The voltage at the terminals of the $mn-$element is written as:

$$V_{mn} = \sum_{p=1}^{M} \sum_{q=1}^{N} Z_{mn,pq} I_{pq} \, , \tag{78}$$

where $Z_{mn,pq}$ is the usual impedance term that is obtained from the impedance matrix, and $I_{pq} = I_o e^{j\left((p-1)\alpha_x + (q-1)\alpha_y\right)}$ is the excitation current applied to the $pq-$element. Assuming all unit-cells in the array are excited with same magnitude currents but with a relative phase shift, the *active impedance* is then defined as [2]:

$$Z_{mn}^{active} = \frac{V_{mn}}{I_{mn}} = \sum_{p=1}^{M} \sum_{q=1}^{N} Z_{mn,pq} \frac{I_{pq}}{I_{mn}} = \sum_{p=1}^{M} \sum_{q=1}^{N} Z_{mn,pq} e^{j\left((p-m)\alpha_x + (q-n)\alpha_y\right)} \, , \tag{79}$$

where α_x and α_y are the relative phase shifts that are used to steer the main beam and that were discussed in Section 5.2. This relation clearly shows that the active impedance is the sum of the self-impedance term ($mn = pq$) and the phased mutual impedance between other elements ($mn \neq pq$). To be noted is that, if active impedance changes as a function of the scan angle, so will do the antenna impedance matching.
For this reason, it is also possible to define the *active scattering parameters* [12]. The incident and reflected wave voltages for the mn-element in the array can be respectively written as [12]:

$$V_{mn}^{+} = Z_c I_{mn}^{+} \, , \tag{80}$$

$$V_{mn}^{-} = \sum_{p=1}^{M} \sum_{q=1}^{N} S_{mn,pq} V_{pq}^{+} \, , \tag{81}$$

where $I_{mn}^{+} = I_0 e^{j\left((m-1)\alpha_x + (n-1)\alpha_y\right)}$ is the phase shifted excitation current provided at element mn and the term $S_{mn,pq}$ is the usual scattering parameter between elements mn and pq. In the following it is still assumed that elements have same magnitude excitation (i.e. $|I_{mn}^{+}| = |I_{pq}^{+}| = I_o$). The *active scattering parameter* at the element mn is defined as [12]:

$$S_{mn,mn}^{active} = \frac{V_{mn}^{-}}{V_{mn}^{+}} = \frac{\sum_{p=1}^{M} \sum_{q=1}^{N} S_{mn,pq} V_{pq}^{+}}{V_{mn}^{+}} = \frac{\sum_{p=1}^{M} \sum_{q=1}^{N} S_{mn,pq} Z_c I_{pq}^{+}}{Z_c I_{mn}^{+}} = \tag{82}$$

$$= \sum_{p=1}^{M} \sum_{q=1}^{N} S_{mn,pq} e^{-j\left((m-p)\alpha_x + (n-q)\alpha_y\right)} . \tag{83}$$

To be noted is that this relation is different from the usual definition of scattering parameters, where one element at a time is excited while the others are terminated on a matched load. In this case, all the elements inside the array are excited at the same time. The definition becomes much more involved and it now needs to account for the mutual coupling terms and relative phase shifts. Ideally, if coupling was not present, meaning $S_{mn,pq} = 0$ for all $mn \neq pq$, then one would obtain that $S_{mn,mn}^{active} = S_{mn,mn}$.

For most practical configurations, mutual coupling is difficult to predict analytically but should be taken into account. Moreover, coupling effects cannot be generalized to any antenna configuration and may be very dependant on the chosen antenna design [2]. Considering microstrip patch antennas, the coupling mechanism is generally attributed to the fields present in the air-dielectric interface and four different types of waves can be identified: radiated or spatial waves, surface waves, guided waves and leaky waves.

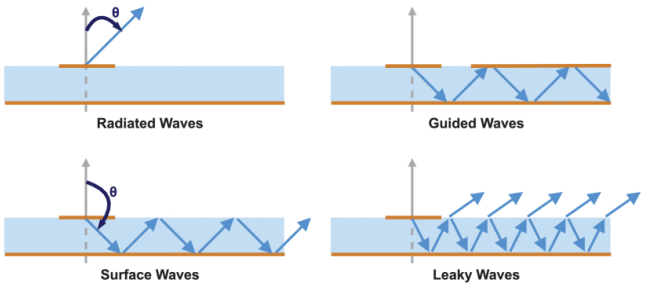

Figure 9.2: Wave coupling mechanisms [13].

Spatial waves are desired when the patch is required to act as a radiator, whereas guided waves propagate in between two metal layers. Surface waves propagate between the substrate and the ground plane, where they are successively reflected, undergoing total reflection. Then there are leaky waves, which are similar to surface waves, but due to their angle of incidence with respect to the dielectric surface they are not totally reflected and therefore radiate part of their energy. Coupling in antenna arrays is mainly attributed to space waves and surface waves [13]. The fact that surface waves propagate within the substrate material is a major concern. For miniaturization purposes, high dielectric constant substrates are typically employed [2]. Moreover, thick substrates are beneficial to widen the bandwidth [2]. However, these types of substrate have the side effect to be particularly favourable to the propagation of surface waves. Coupling increases as the distance between single elements is reduced. One first solution to mitigate coupling would be to position the elements far from each other, but increasing the separation might have the side effect of introducing the grating lobes in the array, which are not desirable. To account for all these effects, careful design choices and compromises should be taken.

9.2 Initial analysis - The reference patch

At the beginning, it was important to firstly understand the general behavior of a single element, the unit-cell that is then used to build the array. As a starting point, a dual-polarized patch was designed and analyzed to understand its features. Figure 9.3a presents the 3D-view of the simplified unit-cell under analysis. An important consideration needs to be made on the size of the unit-cell. As it was mentioned in section 5.1.1, element spacing is critical in an array. If the distance between elements is larger than $\lambda_0/2$, the performance of the array might be severely impaired by the grating lobes. For this reason, it was decided to make the unit-cell smaller than $\lambda_0/2 = 5.55\,mm$, thus $L_s = 5\,mm = 0.45\lambda_0$. To achieve this high miniaturization level a relatively large dielectric constant material was used, the Rogers RO3006 with $\varepsilon_r = 6.15$ and $tan(\delta) = 0.0020$. In [10] it is also reported that, using a small spacing between unit-cells ($< \lambda_0/2$) should be beneficial to provide a well-behaved scan performance.

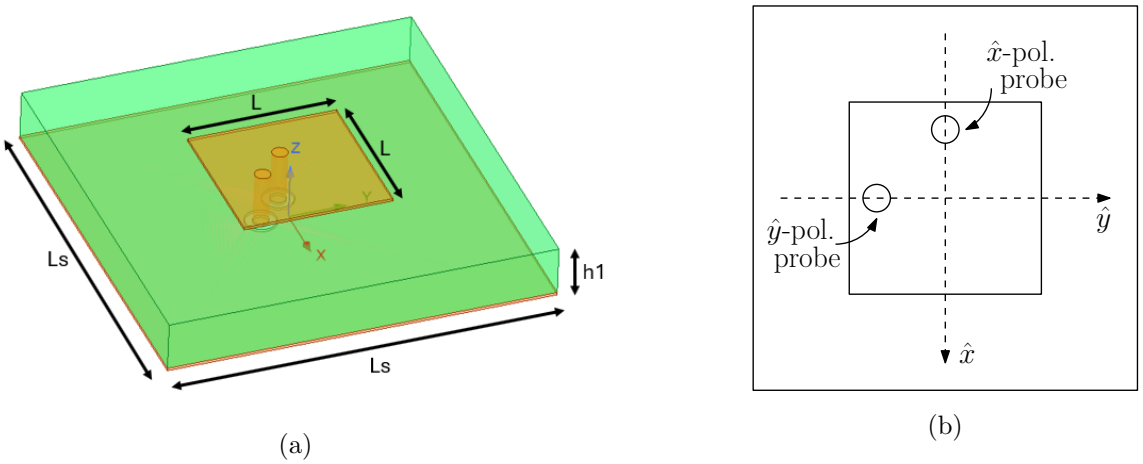

Figure 9.3: (a) Reference dual-polarized patch unit-cell. (b) Detail of the dual linear polarization.

9.2.1 The transmission line model

The radiating element under analysis is a patch antenna. Its radiating properties can be described by the *Transmission Line Model* [2], which can be used to derive some important design equations to guide an initial sizing of the element. The following equations were used throughout the whole design process.

The length of the patch, L, is the main parameter that controls the resonance frequency f_0:

$$L = \frac{c_0}{2f_0\sqrt{\varepsilon_{re}}} - 2\Delta L. \tag{84}$$

The term ΔL accounts for the fringing fields at the edges of the patch, that make it appear electrically larger than the actual geometrical length:

$$\Delta L = 0.412\frac{\varepsilon_{re} + 0.3}{\varepsilon_{re} - 0.258}\frac{W/h + 0.264}{W/h + 0.8}h, \tag{85}$$

where h is the substrate thickness, W is the width of the patch, and ε_{re} is the *effective* relative dielectric constant:

$$W = \frac{c_0}{2f_0}\sqrt{\frac{2}{\varepsilon_r + 1}}, \tag{86}$$

$$\varepsilon_{re} = \frac{\varepsilon_r + 1}{2} + \frac{\varepsilon_r - 1}{2}\left(1 + \frac{12h}{W}\right)^{-1/2}. \tag{87}$$

The term ε_r is instead the relative dielectric constant of the substrate material used.

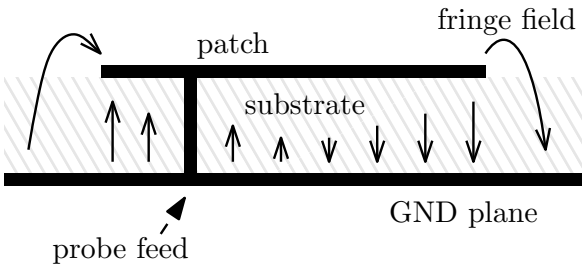

Figure 9.4: Microstrip patch transmission line model - Electric field distribution.

The dual linear polarization can be achieved by exciting the patch with two feed probes, realized with plated vias. The feed probes should be placed where the input impedance of the antenna matches the characteristic impedance of the transmission line the antenna is connected to. In this case, the reference impedance is set to be $Z_0 = 50\,\Omega$. For probe fed patch antennas, the input impedance at a distance Δx_p (later defined as *inset*) from the patch edge is:

$$Z_A(\Delta x_P) = Z_A(\Delta x_P = 0)cos^2\left(\frac{\pi\Delta x_P}{L}\right). \tag{88}$$

The term $Z_A(\Delta x_P = 0)$ is the input impedance at the edge of the patch. Its value can be approximated with the peak input resistance at resonance:

$$Z_A(\Delta x_P = 0) = R_A \approx 90\frac{\varepsilon^2}{\varepsilon - 1}\left(\frac{L}{W}\right)^2. \tag{89}$$

The two vias are therefore placed as shown in Figure 9.3b.
After plugging the known values in the formulas above, the initial theoretical parameters of the patch were computed for the resonance frequency $f_0 = 27\,GHz$:

substrate height	$h1 = 0.64\,mm$	relative dielectric constant	$\varepsilon_r = 6.15$
substrate length	$L_s = 5\,mm$	feed inset	$inset = 0.69\,mm$
patch length	$L = 1.97\,mm$	feed via diameter	$diamVia = 0.2\,mm$

Table 7: Reference patch theoretical parameters.

To be noted is the fact that the transmission line model yields the theoretical dimensions a *rectangular* patch should have in order to resonate at the given desired frequency. But in this design, since the objective is to have a dual linear polarization at the same frequency, the patch cannot be rectangular, in fact it should be a square, with all its sides equal to L.

9.2.2 Simulation results

After some adjustments using the simulation software, the amended parameters and the simulated results of this initial analysis are shown in the following:

substrate height	$h1 = 0.64\,mm$	relative dielectric constant	$\varepsilon_r = 6.15$
substrate length	$L_s = 5\,mm$	feed inset	$inset = 0.6\,mm$
patch length	$L = 1.91\,mm$	feed via diameter	$diamVia = 0.2\,mm$

Table 8: Reference patch - amended parameters.

For simplicity and due to the symmetry of the dual linear polarization, the radiation pattern that is shown in the following is the one for the $\hat{x}$-polarization active.

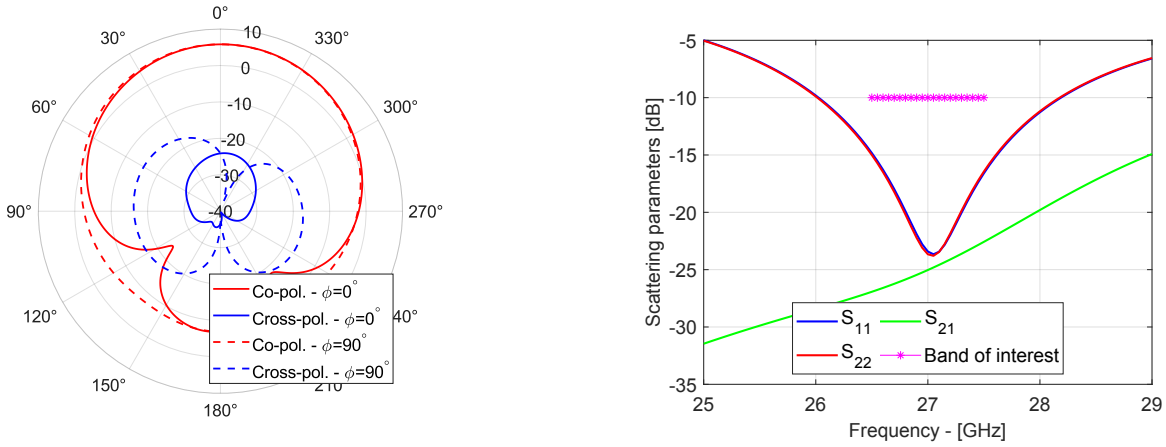

(a) Realized gain [dBi] - $\hat{x}$-pol. at 27 GHz.

(b) Scattering parameters.

Figure 9.5: Reference patch - simulated results.

The symmetry between the $\hat{x}$ and $\hat{y}$ polarizations is confirmed when evaluating the realized gain and the HPBW:

Polarization	**Peak realized gain** $\phi = 0°$	**Peak realized gain** $\phi = 90°$	**HPBW** $\phi = 0°$	**HPBW** $\phi = 90°$
$\hat{x}$-pol.	5.81 [dBi]	5.81 [dBi]	96.9°	100.5°
$\hat{y}$-pol.	5.80 [dBi]	5.81 [dBi]	100.4°	96.7°

Table 9: Simulated parameters of the reference patch at 27 GHz.

To be noted is that the HPBW achieved by the isolated element is $\approx 100°$.

9.2.3 Reference patch 5×5 array

Adopting the unit-cell that was just designed, the next step is to simulate it in a finite array: the characteristics of a 5×5 planar array are now evaluated. The array, shown in Figure 9.6a, consists of twenty-five reference patch unit-cells that are arranged on the $\hat{x}$ and $\hat{y}$ axes using a square layout. The center-to-center distance between the cells is the same on both the axes: $d_x = d_y = 5\,mm = 0.45\lambda_0$. In order to assure that the grating lobes are kept out of the visible range of the array even for large scan angles, the theoretical normalized array factor was studied first for the broadside condition and for large scan angles ($\pm\,60°$). The result, shown in Figure 9.6b, confirms that there should not be any grating lobes in the visible range of this array configuration.

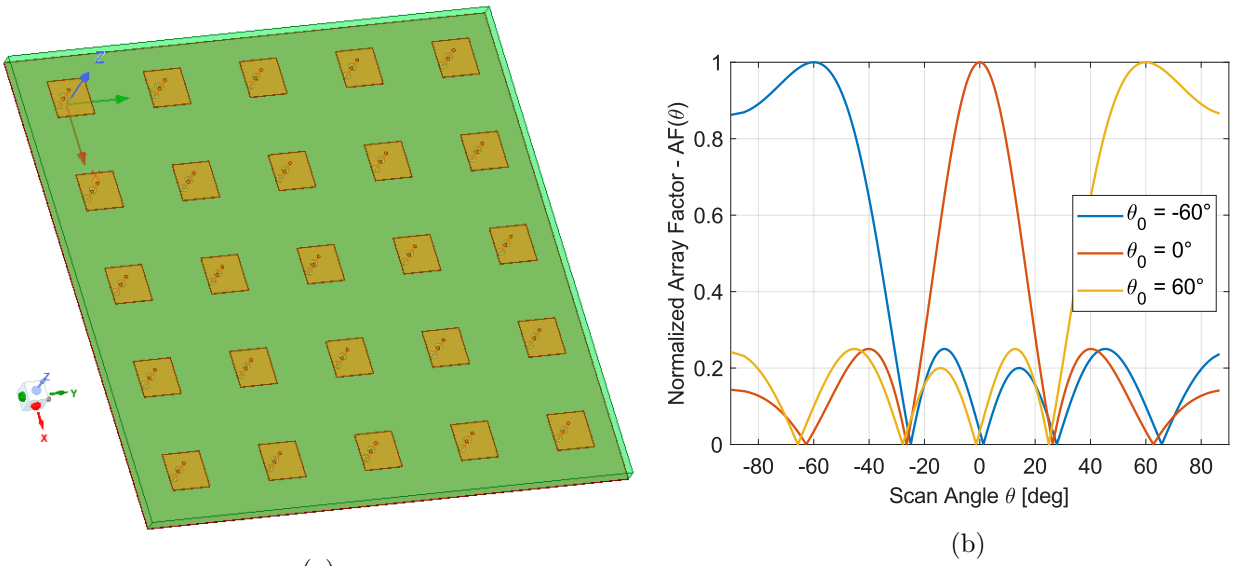

(a) (b)

Figure 9.6: (a) 5×5 array of reference patch unit-cells. - (b) Theoretical normalized array factor - $N_y = 5$ - $d_{array} = 5\,mm = 0.45\lambda_0$ - $\phi = 90°$.

Given the fact that the array type is planar, the main beam can be scanned toward a generic angle (θ_0, ϕ_0). To simplify the analysis, the following results will only present the scans along the two principal planes: the xz-plane ($\phi = 0°$) and the yz-plane ($\phi = 90°$). Both polarizations will be tested, but one at a time. This is possible because each feeding probe is excited by a dedicated port. As a side note, all ports are set to a $50\,\Omega$ reference impedance. To steer the main beam, all the ports that belong to the polarization under test are excited with the same signal magnitude. For each scanning angle, the required phase difference between adjacent cells was computed using equation (59). All the following simulation results are reported at the center frequency $f_0 = 27\,GHz$.
Figures 9.7a, 9.8a, 9.9a, 9.10a present the realized gain patterns at different scan angles. Instead, Figures 9.7b, 9.8b, 9.9b, 9.10b show the peak realized gain for different scan angles and normalized with respect to the broadside ($\theta_0 = 0°$) condition. From these plots, one can also extract the scan-loss, in fact: $(\text{scan-loss})_{dB} = SL_{dB} = -\,(\text{normalized peak realized gain})_{dB}$.

Firstly, the scanning using the $\hat{x}$-polarization is observed:

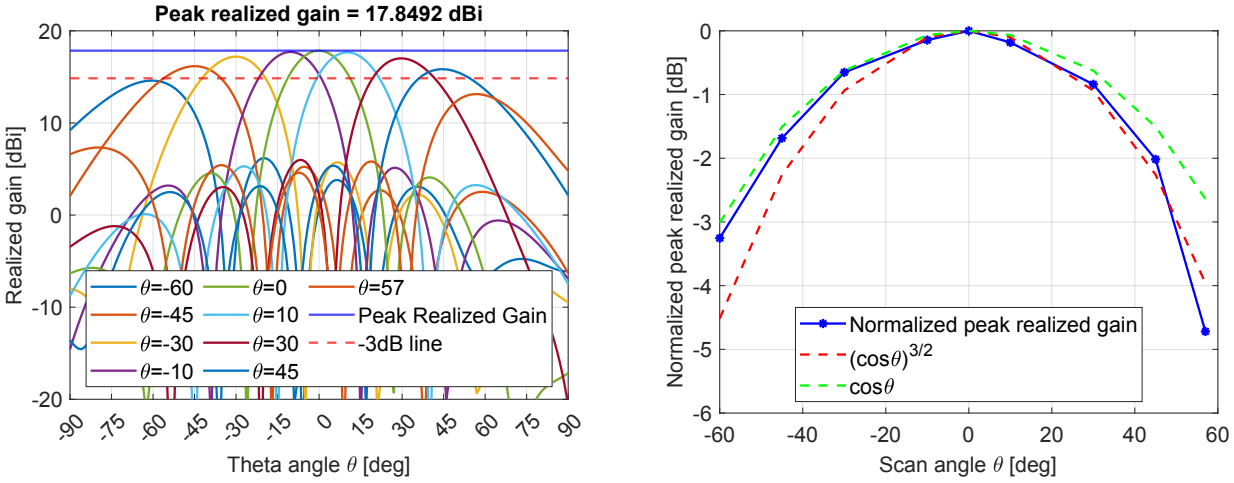

(a) (b)

Figure 9.7: (a) Realized gain - $\phi = 0°$ - $\hat{x}$-pol. (b) Normalized peak realized gain - $\phi = 0°$ - $\hat{x}$-pol.

Scan angle θ_0	$-60°$	$-45°$	$-30°$	$-10°$	$0°$	$10°$	$30°$	$45°$	$57°$
Scan-loss [dB]	3.25	1.68	0.62	0.14	0	0.18	0.94	2.02	4.72

Table 10: Scan-loss summary - $\phi = 0°$ - $\hat{x}-$pol.

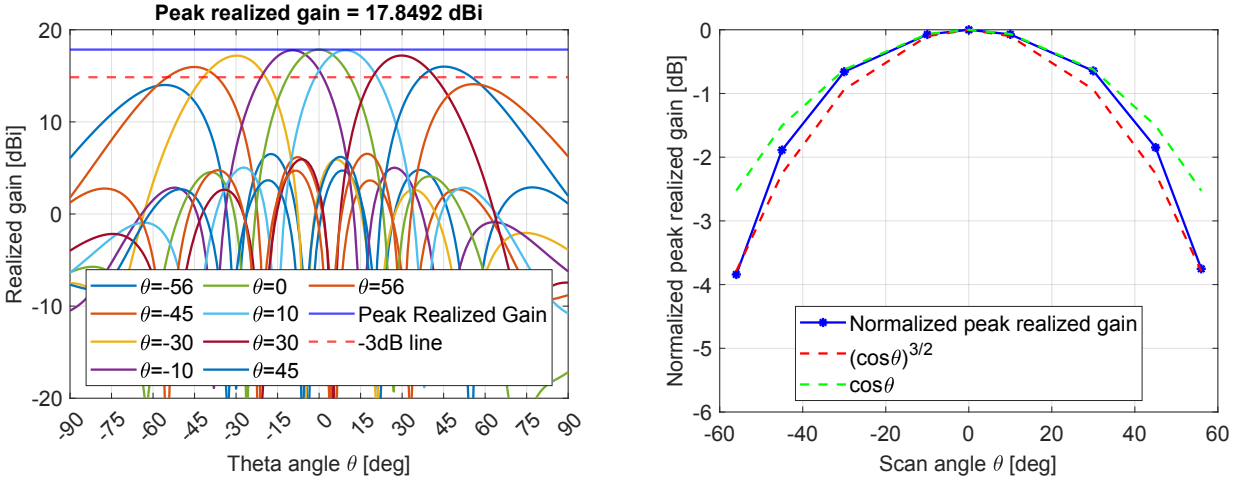

(a) (b)

Figure 9.8: (a) Realized gain - $\phi = 90°$ - $\hat{x}$-pol. (b) Normalized peak realized gain - $\phi = 90°$ - $\hat{x}$-pol.

Scan angle θ_0	$-56°$	$-45°$	$-30°$	$-10°$	$0°$	$10°$	$30°$	$45°$	$56°$
Scan-loss [dB]	3.84	1.89	0.62	0.07	0	0.07	0.62	1.85	3.79

Table 11: Scan-loss summary - $\phi = 90°$ - $\hat{x}-$pol.

The analysis continues with the $\hat{y}$-polarization:

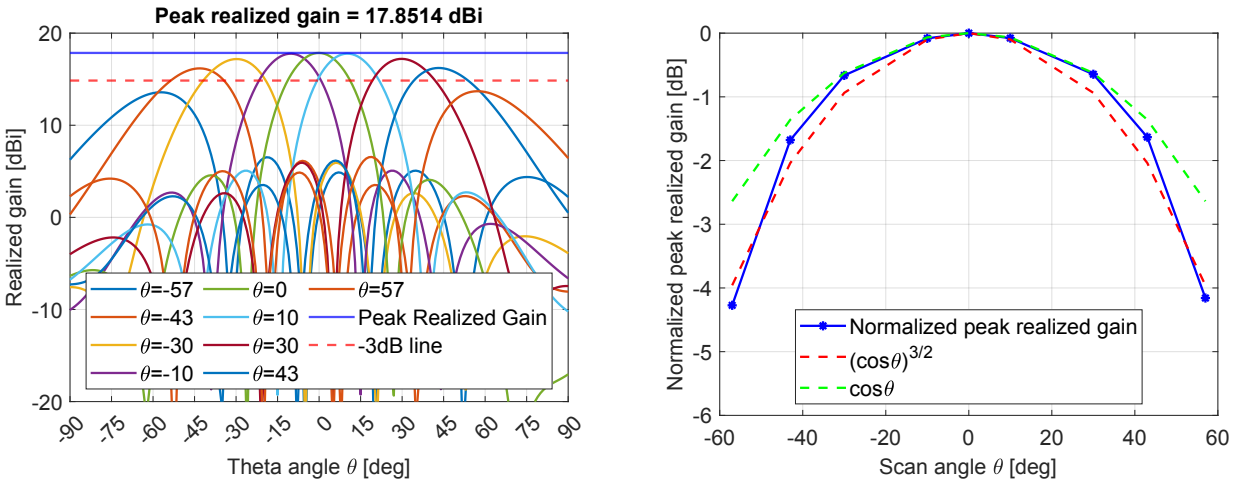

(a) (b)

Figure 9.9: (a) Realized gain - $\phi = 0°$ - $\hat{y}$-pol. (b) Normalized peak realized gain - $\phi = 0°$ - $\hat{y}$-pol.

Scan angle θ_0	$-57°$	$-43°$	$-30°$	$-10°$	$0°$	$10°$	$30°$	$43°$	$57°$
Scan-loss [dB]	4.27	1.68	0.62	0.07	0	0.07	0.62	1.63	4.16

Table 12: Scan-loss summary - $\phi = 0°$ - $\hat{y}-$pol.

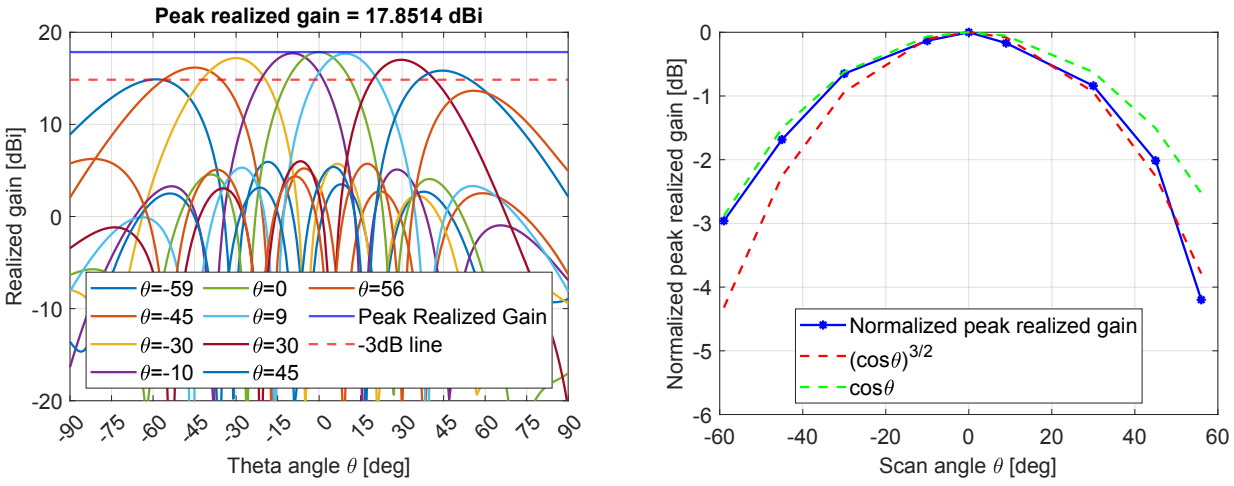

(a) (b)

Figure 9.10: (a) Realized gain - $\phi = 90°$ - $\hat{y}$-pol. (b) Normalized peak realized gain - $\phi = 90°$ - $\hat{y}$-pol.

Scan angle θ_0	$-59°$	$-45°$	$-30°$	$-10°$	$0°$	$9°$	$30°$	$45°$	$56°$
Scan-loss [dB]	2.96	1.68	0.62	0.09	0	0.17	0.94	2.02	4.20

Table 13: Scan-loss summary - $\phi = 90°$ - $\hat{y}-$pol.

To be noted is that, for both polarizations, the absence of the grating lobes is confirmed. It is also interesting to observe that the normalized scanned pattern envelope, which represents the scan-loss, behaves in a way that is in between the $(cos\theta)$ and $(cos\theta)^{3/2}$ curves, as mentioned in Section 9.1. At the maximum scan angle the worst scan-loss approaches $5\,dB$. In general, the sidelobe level (SLL) achieved at broadside is $SLL_{\theta_0=0^\circ} \approx -13\,dB$, while for larger scan angles, it increases up to $\approx -7\,dB$. Although this kind of performance should be expected from an array of microstrip patch antennas, the aim of this work is to find a way to improve it. To get a further insight, the radiation patterns of one individual unit-cell inside the 5×5 array are analyzed. The patterns considered here, also referred to as embedded patterns, are the ones of the central unit-cell, as in Figure 9.6a. The process of evaluating the embedded patterns is essential for understanding how the presence of other elements affects the unit-cell's radiation characteristics. It can also provide an insight on how the whole array will perform in terms of scanning. While all the remaining ports are terminated on a matched load, the feeding probes of the selected unit-cell are excited one at a time and the radiation patterns are observed. For symmetry, only the $\hat{x}$-polarized patterns are shown, but the details for both are reported in the adjacent tables.

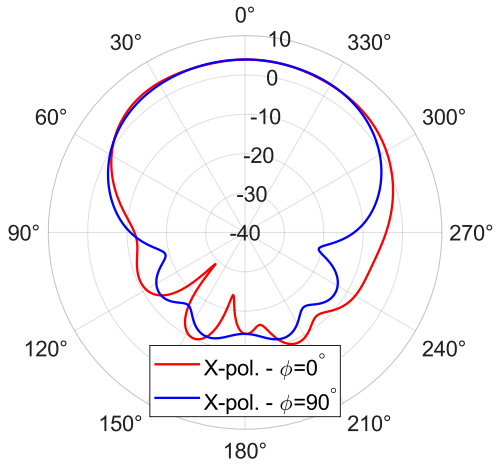

Figure 9.11: Realized gain [dBi] at $27\,GHz$ of the central unit-cell inside the array - $\hat{x}$-pol.

	HPBW $\phi = 0°$	**HPBW** $\phi = 90°$
$\hat{x}$-pol.	117°	107°
$\hat{y}$-pol.	107°	117°

Table 14: HPBW of the central unit-cell.

	Peak realized gain at 27 GHz
$\hat{x}$-pol.	$3.9\,dBi$
$\hat{y}$-pol.	$3.9\,dBi$

Table 15: Peak realized gain of the central unit-cell.

If compared to the patterns obtained for the isolated unit-cell, shown in Figure 9.5a, the ones that result inside the array are quite different: the shape and the HPBW have changed significantly. In particular, the HPBW of the unit-cell has become larger inside the array, if compared to the isolated case. Moreover, the peak realized gain also decreased. This behavior can be justified, in fact, recalling equation (30), the effective area to gain ratio is constant for any kind of antenna, thus the element gain inside the array has to decrease in order to comply with such constraint. If we assume to approximate the effective area with the geometric area of the array, we can check the expected maximum gain for the array:

$$G_{MAX}^{dBi} = 10log_{10}\left(\frac{4\pi}{\lambda^2}N(0.45\lambda)^2\right)\Bigg|_{N=5\times5} \approx 18\,dBi, \tag{90}$$

and subtracting the Array Factor (AF), one obtains the maximum allowed gain of a unit-cell:

$$G_{unit-cell}^{MAX} = G_{MAX}^{dBi} - AF_{dB} = 18 - 10log_{10}(5 \times 5) = 4\, dBi, \tag{91}$$

which is in the order of what was obtained in the simulated results that were previously shown. The analysis continues with the simulated reflection coefficients ($S_{11}, S_{22}, ...$) at all the ports of the 5×5 array.

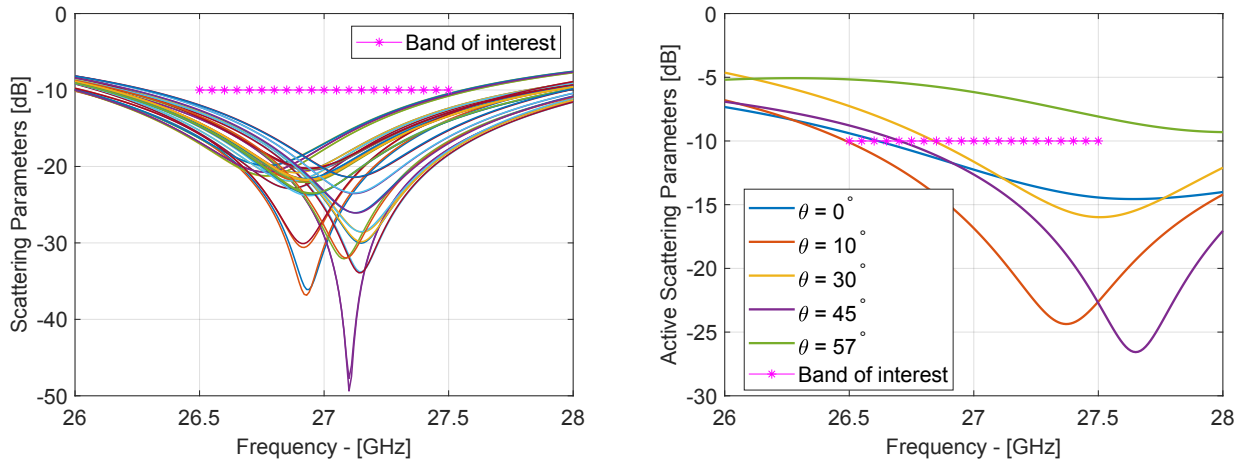

(a) (b)

Figure 9.12: (a) Scattering parameters - all ports. (b) Active scattering parameters for the array central element - $\phi = 0°$ - $\hat{x}-$pol.

Figure 9.12a shows the simulated *scattering parameters* at all the ports of the array. It can be observed that, depending on the position of the port inside the array, i.e. in the center, at the edge or in the corner, impedance matching changes. This effect can be attributed to mutual coupling. Nevertheless, all ports result to be almost matched inside the band of interest. Figure 9.12b reports instead the *active scattering parameters* at the $\hat{x}-$polarized probe feed of the central unit-cell when scanning at different angles in the $\phi = 0°$ plane, with only the $\hat{x} - pol.$ active. As it was discussed in Section 9.1, the active scattering parameters depend on coupling and excitation with respect to the other adjacent unit-cells. It can be observed that as the scan-angle deviates from broadside, impedance matching becomes increasingly worse. This issue is a very typical characteristic of phased arrays. Using traditional matching methods, unit-cells can be impedance matched only at one scan angle and are mismatched at other angles [14][15]. This mismatch causes reflection losses that directly affect the realized gain, making it decrease, especially at large angles. The complexity of the problem has made it of high research interest. Among some of the trials, it was reported that spacing elements at less than $\lambda_0/2$ could help to achieve a weaker impedance variation with the scan angle [2][10]. Other approaches place in front of the array a dielectric sheet (also called *WAIM layer*) with a certain dielectric constant and at a specific distance in order to perform Wide-Angle Impedance Matching (WAIM) [14]. Other solutions further extend the WAIM concept using metasurfaces [15].

9.3 A method for beamwidth enlargement

Motivated to improve the scanning capability that was analyzed in the 5×5 array of reference patch unit-cells, the following sections investigate a method to increase the half-power beamwidth (HPBW) of the unit-cell element. This should allow to mitigate the array scan-loss at large angles. In the literature there have been several attempts to design a single-element with an increased beamwidth. The base antenna element that is usually employed is the very popular microstrip patch antenna. The element is then modified to achieve the desired beam extension. As proposed in [16] and [17], one possible modification is the so called *vertical-wall loading*.

9.3.1 Loading on the patch radiating edges

By loading the patch with two vertical electric walls on its radiating edges, a parasitic vertical current would be induced on the walls by the presence of the fringing electric fields. The concept of loading the electric walls is applied to the reference patch, as shown in Figure 9.13, where only one feed via is considered to simplify this initial analysis.

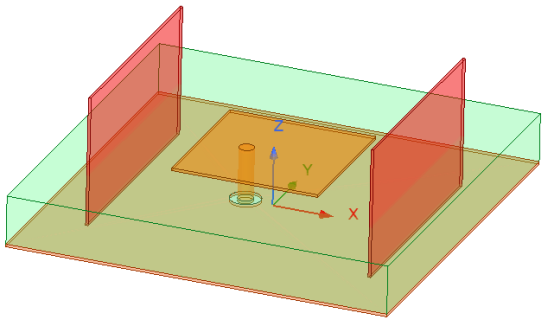

Figure 9.13: Concept of loading the patch with vertical walls.

The fringing electric fields generated by the patch can induce a vertical electric current on the walls. The transmission line model imposes that the electric fields at the radiating edges of the patch are in opposition of phase, since the length of the resonant patch is close to $\lambda_g/2$, with λ_g computed in the substrate at the chosen center frequency. This means that the induced vertical currents, J_1 and J_2, will also be out of phase and separated by almost $\lambda_g/2$. This mechanism is shown in Figure 9.14a. Note that the walls are connected to the ground plane.

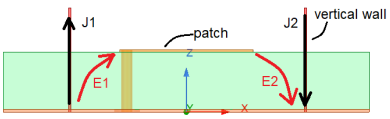

(a)

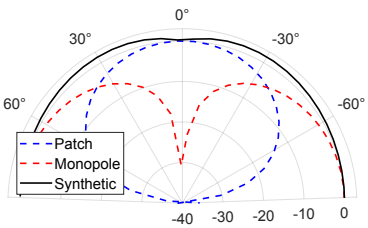

(b)

Figure 9.14: (a) Vertical walls working mechanism. (b) Superposition of normalized patterns [dB].

The total radiation pattern is synthetic, because it is the superposition of the one generated by the patch with the one that results from the presence of the vertical currents. The vertical currents can be regarded as a kind of monopole; together they form an array of two elements oriented along the $\hat{x}-$axis and separated by a distance $\approx \lambda_g/2$. This means that, for the array factor, they will add in phase along the $\hat{x}$ direction and they will instead cancel out in the $\hat{y}$ direction. The synthetic radiation pattern can be approximated by the following relations [16]:

$$F_{patch}(\theta,\phi) \approx K_1 cos\left(\frac{\beta L}{2} sin(\theta)\right) \tag{92}$$

$$F_{monopole}(\theta,\phi) \approx K_2 sin(\theta) \tag{93}$$

$$F_{total}(\theta,\phi) \approx F_{patch}(\theta,\phi) + F_{monopole}(\theta,\phi) \tag{94}$$

where F_{patch} is the field pattern of the patch, $F_{monopole}$ is the field pattern of the monopole-like vertical currents and F_{total} is instead the total radiation pattern given by the superposition of patch and vertical currents. The above relations are plotted in Figure 9.14b, from which one can observe the effect of the vertical currents in extending the radiation pattern of the patch. The coupling between the patch and the vertical currents, which is described by the complex valued K_1 and K_2 terms, mainly depends on the height and the distance of the vertical walls from the patch [16]. Tuning these parameters has the effect of controlling the pattern extension and also the impedance matching.
In order to understand the working mechanism of the proposed method, a pair of vertical electric walls are loaded on the radiating edges of the reference patch. The resulting geometry, presented in Figure 9.13, is then studied through a parametric analysis. The main objective is to identify the relation that exists between the pattern extension and the following parameters:

- **c**: the distance of the vertical walls from the patch radiating edge;
- **v**: the height of the vertical walls.

In Figure 9.15 the pattern extension is quantified by evaluating the HPBW for different values of **c** and **v**. If compared to the reference patch, the simulated results show that the proposed method can effectively increase the beamwidth in both planes, although it is more effective on the $\phi = 0°$ plane.

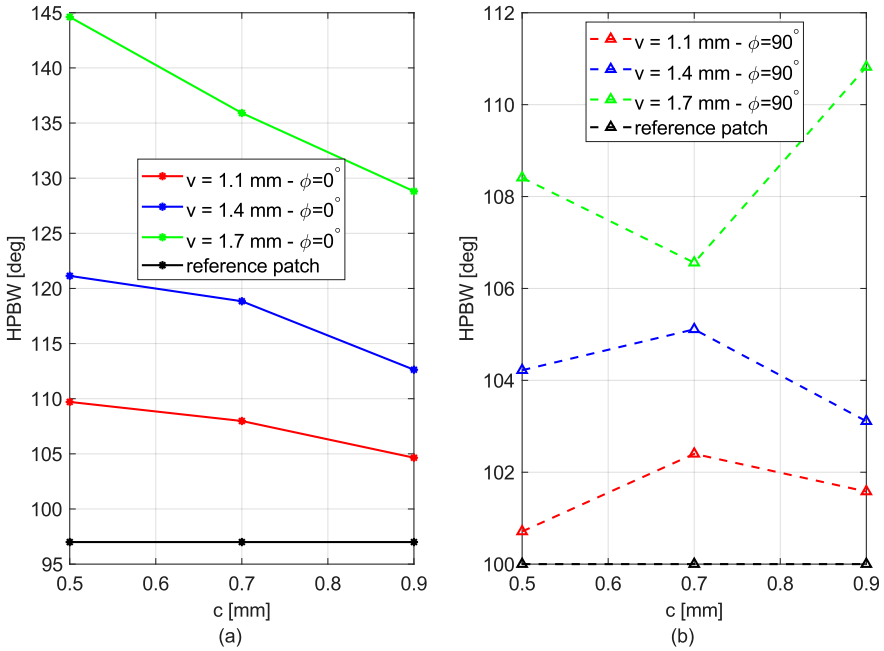

Figure 9.15: HPBW for different values of **c** and **v** - (a) $\phi = 0°$ - (b) $\phi = 90°$.

The trend that can be observed is that the beamwidth increases as the height of the electric walls gets larger while instead it decreases as the distance of the walls from the patch increases.

9.3.2 Loading on the patch non-radiating edges

In addition to positioning the vertical walls on the radiating edges of the patch, the loading on the non-radiating edges was also investigated. Recalling the transmission line model, the electric field along the non-radiating edges of the patch follows a cosine distribution. If the vertical electric walls were loaded on the non-radiating edges like it was done for the radiating ones, then a pair of inverted vertical currents would be induced on each of the walls, therefore cancelling out [17]. To avoid this condition, the loading method is modified and the vertical walls on the non-radiating edges are cut in the center, as shown in Figure 9.16.

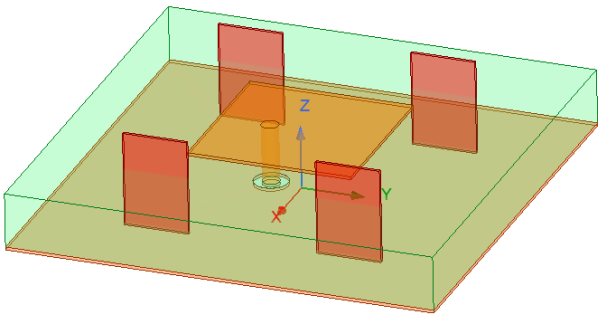

Figure 9.16: Concept of vertical walls loading the non-radiating edges.

Another parametric study is conducted: the effect of parameters **c** and **v** are investigated also for the loading on the non-radiating edges. The following results refer to the case in which the size of the cut on the vertical walls is $d = 1.5\,mm$.

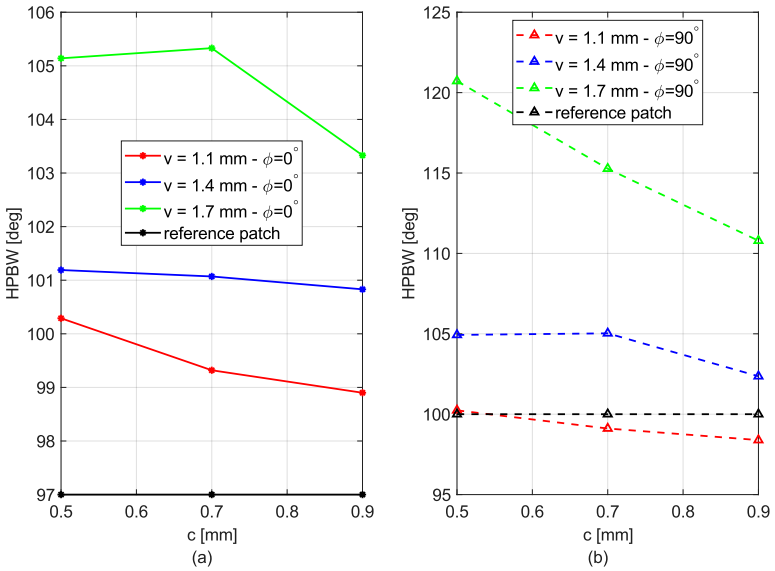

Figure 9.17: HPBW for different values of **c** and **v** - (a) $\phi = 0°$ - (b) $\phi = 90°$.

According to this initial analysis, the loading on the non-radiating edges has a less strong effect on beamwidth enlargement on the $\phi = 0°$ plane compared to the previous case, but on the $\phi = 90°$ plane and for an optimized set of parameters the pattern could be well extended. It should be therefore possible to combine the two types of loading together so that the unit-cell pattern can be extended in both planes.

9.4 The proposed unit-cell

So far, the concept of loading vertical walls on the edges of a patch antenna has been investigated and it has shown the potential to enlarge the radiation pattern beamwidth. Based on this method, a dual linearly polarized unit-cell, consisting of a modified patch antenna, is presented next.

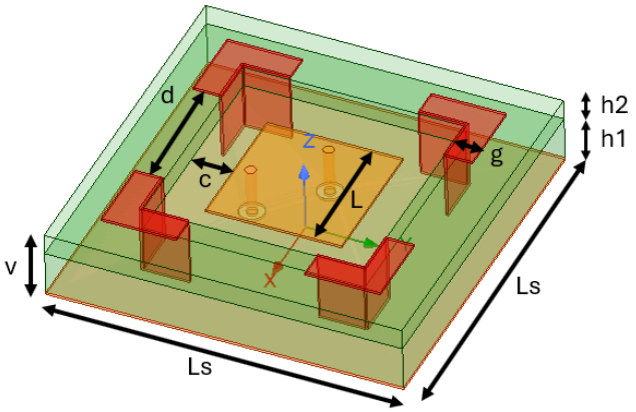

Figure 9.18: Initial version of the proposed unit-cell.

As it can be seen in Figure 9.18, the method of loading vertical walls on both the radiating and non-radiating sides of the patch is further elaborated, as reported in [17]. The main task is to maintain the design symmetric. This constraint is necessary, because both the polarizations

should work in a very similar way and both should have their pattern extended. As it was previously described, the loading on the non-radiating edges should use walls that are cut in the center, which is different from the loading mechanism on the radiating edges.
The loading on the radiating edges was therefore modified and the walls were cut in the center. As a result, the patch could be loaded with vertical walls positioned at the four corners without compromising the beam extension. The design is therefore symmetric. Part of the vertical walls is folded parallel to the ground plane and layed over an additional dielectric layer. The loading walls are therefore turned into a kind of inverted-L antenna. As such, the currents that flow in the horizontal parts of the walls do not radiate. For the image theory, as shown in Figure 9.19, an electric current flowing parallel to a ground plane is canceled by the image current, therefore it does not contribute to the far-field radiation. Only the vertical currents radiate, with the mechanism previously discussed.

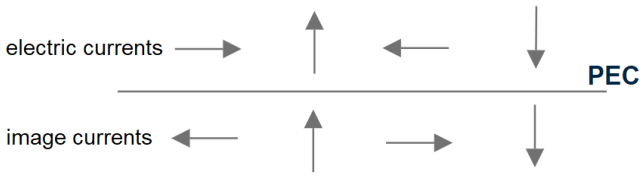

Figure 9.19: Image theory for electric currents over a perfect electric conductor (PEC).

Introducing the horizontal folded parts is functional: the size of them represents an additional tuning parameter that can be used during the optimization phase to control both pattern extension and impedance matching. The additional dielectric layer is kept of the same material as the radiating substrate of the patch, that is a Rogers RO3006. Its main function is to support the walls. The additional dielectric layer was also cut in the center to expose the patch to the air. The cut was found to ease the impedance matching process of the unit-cell antenna. The radiating element is a square microstrip patch with its two feed probes for the dual linear polarization.
Several new parameters are introduced with this modified unit-cell:

Parameter	**Description**
c	the distance of the vertical walls and of the opening on the additional dielectric layer from the side of the patch
g	the size of the horizontal metallic elements
v	the height of the vertical walls
d	the size of the center cut on the walls
h2	height of the additional dielectric layer ($h2 = v - h1$)

Table 16: Parameters of the modified element.

To study the characteristics of the modified unit-cell and the effects that each parameter has, a parametric analysis was carried out. By tuning the dimensions of the parameters one can control both the pattern extension and the impedance matching. The results of some of the parametric analyses that were conducted are reported in the following.

The **c** parameter corresponds to the distance of the vertical walls from the side of the patch. As the walls get closer and **c** decreases, the induced vertical currents become stronger and the pattern beamwidth can be effectively extended but the impedance matching gets shifted towards lower frequencies. Instead, when **c** increases, the walls get more distant from the patch and the coupling between the two becomes weaker, making the pattern less extended and shifting the impedance matching towards higher frequencies.

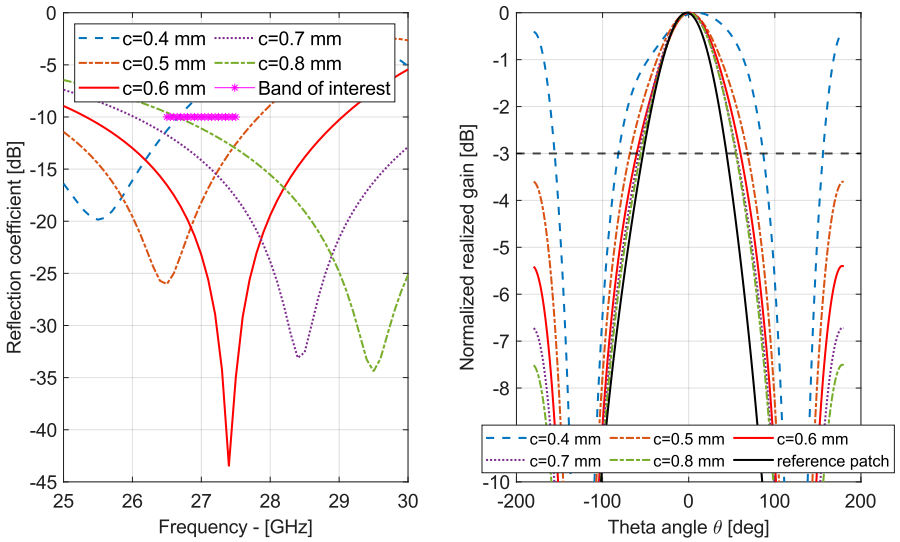

Figure 9.20: (a) Reflection coefficient & (b) normalized $\hat{x}-$pol. radiation pattern on $\phi = 0°$ for different **c** values.

Then there is the parameter **g**, which controls the size of the horizontal metallic elements that are parallel to the ground plane. Variations of this parameter have both an influence on the pattern extension but also on the antenna matching. For example, if **g** increases, then the pattern beamwidth is extended but the impedance matching shifts towards lower frequencies.

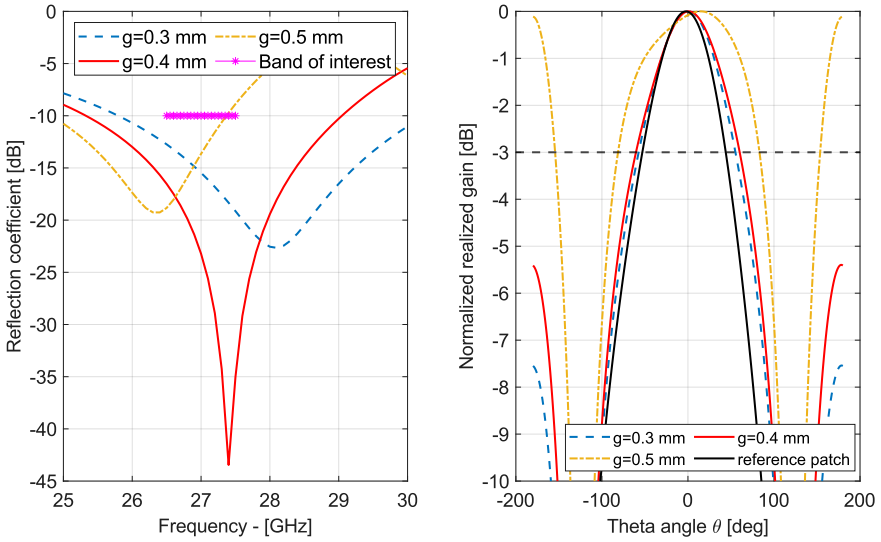

Figure 9.21: (a) Reflection coefficient & (b) normalized $\hat{x}-$pol. radiation pattern on $\phi = 0°$ for different **g** values.

These type of analyses were also carried out for the remaining parameters and several simulation runs were performed to optimize the design. The procedure that was followed can be summarized as follows:

1. Decide a parameter to analyze while the others remain fixed;
2. perform parametric sweeps to understand the influence of the chosen parameter on both pattern extension and impedance matching;
3. find an intermediate solution that gives a satisfactory result;
4. start again from (1.) with a different parameter.

In the end, this process led to an initial set of design parameters that are listed in the following table:

L_s	5 mm	ε_r	6.15	h1	0.64 mm
L	1.9 mm	inset	0.2 mm	diamVia	0.15 mm
c	0.6 mm	g	0.4 mm	v	0.94 mm
d	1.8 mm	$h2 = v - h1$	0.3 mm		

Table 17: Initial set of parameters for the design in Figure 9.18.

The radiation patterns in the $\phi = 0°$ & $\phi = 90°$ plane cuts for the $\hat{x}-$polarization are reported in the following Figures, where they are compared against the reference patch.

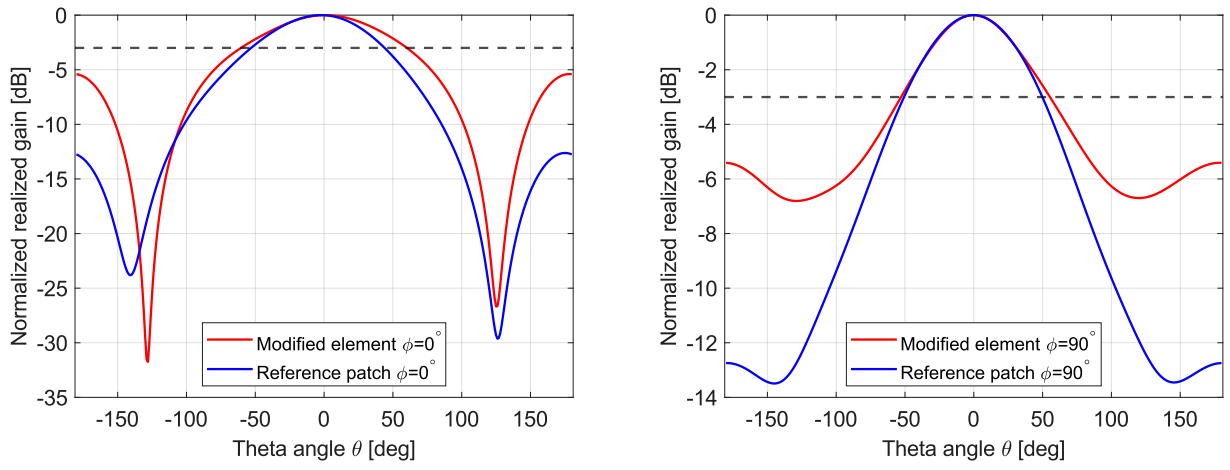

(a) (b)

Figure 9.22: (a) Normalized realized gain - $\hat{x}$-pol. - $\phi = 0°$ - $f_0 = 27\,GHz$. (b) Normalized realized gain - $\hat{x}$-pol. - $\phi = 0°$ - $f_0 = 27\,GHz$.

The HPBW of the modified element results to be extended. To be noted is that, for a given polarization, the extension on the two planes is not the same, and is more favourable for one cut compared to the other. Also, comparing the reference patch to this modified unit-cell, the latter has a reduced peak realized gain, but this can be justified by its increased beamwidth. In fact, a compromise between gain and pattern extension should be made.

In any case, the symmetry between the $\hat{x}$ & $\hat{y}$-polarizations is still present and they have comparable characteristics:

	HPBW phi 0°	**HPBW** phi 90°	**Realized Gain** phi 0°	**Realized Gain** phi 90°
$\hat{x}$**-pol.**	120°	108°	4.37 [dBi] (peak)	4.37 [dBi] (peak)
$\hat{y}$**-pol.**	107°	121°	4.35 [dBi] (peak)	4.35 [dBi] (peak)

Table 18: HPBW and Peak Realized Gain of the modified unit-cell - $f_0 = 27$ GHz.

The scattering parameters for the modified element are reported in the following: by adjusting the parameters the whole band of interest can be matched.

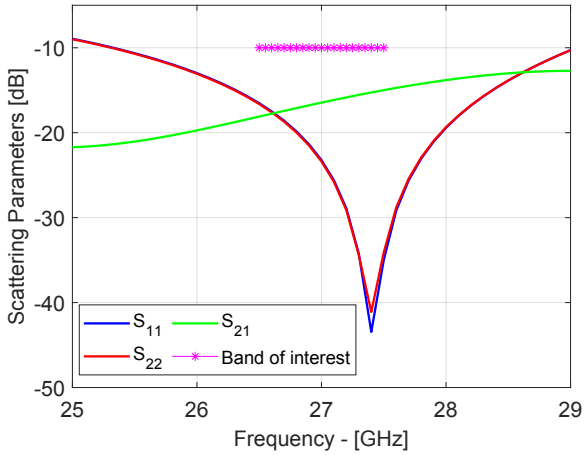

Figure 9.23: Scattering parameters for the modified element.

9.4.1 Modified vertical walls

Although the previous design was helpful to understand the working mechanism of the vertical wall loading method, the major issue is related to the vertical walls themselves. From a manufacturing point of view, they would be impractical to realize. Given that the function of the walls is to support the vertical parasitically induced currents, it should be possible to substitute them with plated vias, which are more convenient to fabricate [17].
The modified design is shown in Figure 9.24a. Figure 9.24b reports the simulated surface current density vector on the plated vias to show their function in supporting the induced currents. The working principle of this modified design is not different from the previous one.

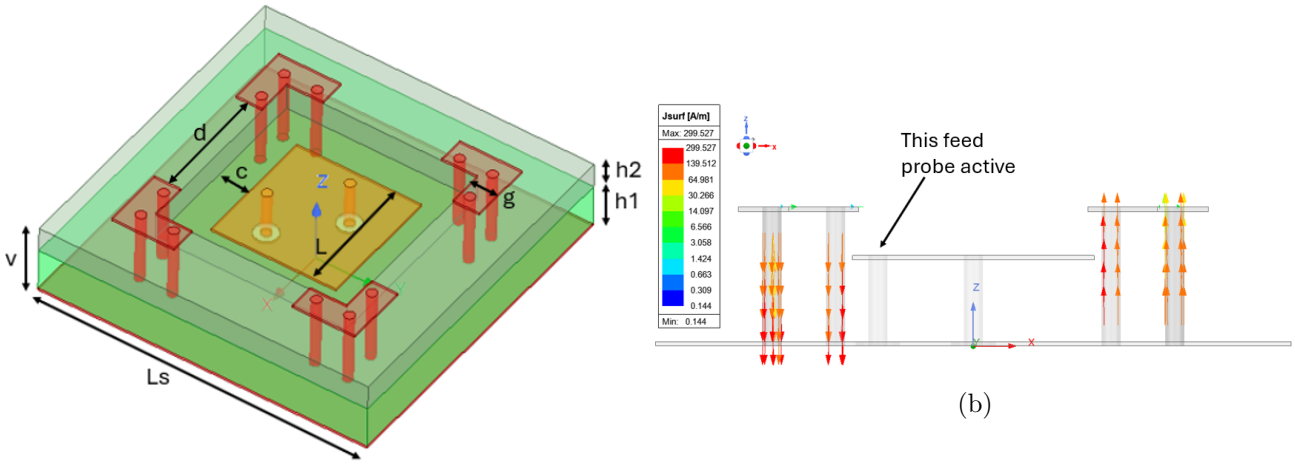

(a) (b)

Figure 9.24: (a) Vertical walls substituted with plated vias. (b) Surface current density vector on plated vias.

The distance between adjacent vias is kept very small, around $\lambda_g/20$. From an electromagnetic point of view, they should appear as if they were a continuous vertical wall. Moreover, the effort was also put into using standard thickness substrate materials, and this is mainly related to the additional dielectric layer. Its height was actually increased from $h2 = 0.3\,mm$ to $h2' = 0.38\,mm$. The **c** parameter was also slightly modified. Because the height of the top substrate layer was increased, it also moved the center frequency to the lower part of the band. Given the relation between impedance matching and the parameter **c** that was found during the parametric studies, by changing from $c = 0.6\,mm$ to $c = 0.5\,mm$, the matching center frequency could be restored. Apart from the just mentioned parameters, the other geometrical dimensions, which are reported in the following table, remained unchanged with respect to the previous version.

L_s	5 mm	ε_r	6.15	h1	0.64 mm
L	1.9 mm	inset	0.2 mm	diamVia	0.15 mm
c	0.5 mm	g	0.4 mm	v	1.02 mm
d	1.8 mm	$h2 = v - h1$	0.38 mm		

Table 19: Set of parameters for the design in Figure 9.24a.

The simulated radiation patterns of this unit-cell are now reported in detail for both the $\hat{x}$ and $\hat{y}$ polarizations:

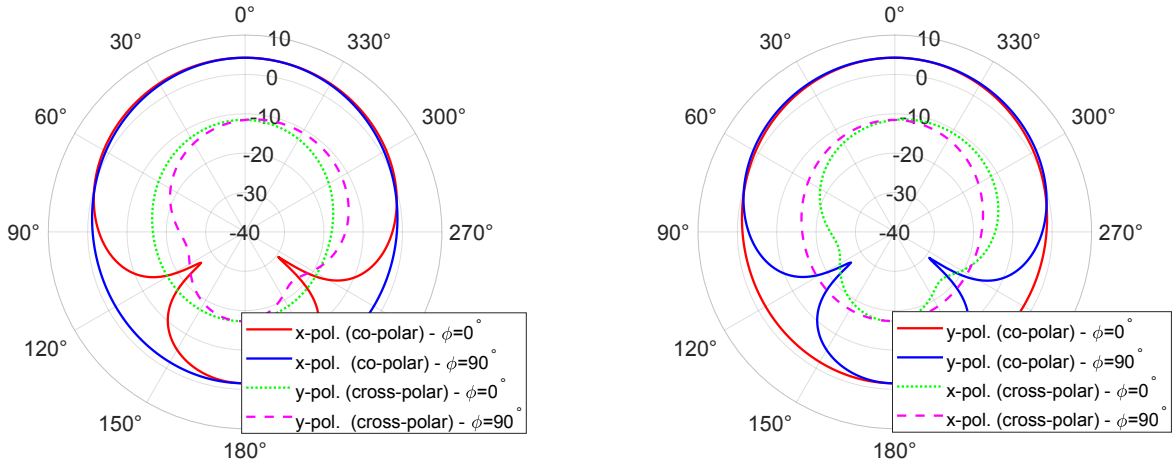

(a) (b)

Figure 9.25: Realized gain [dBi] at $f_0 = 27$ GHz (a) $\hat{x}$-polarization and (b) $\hat{y}$-polarization.

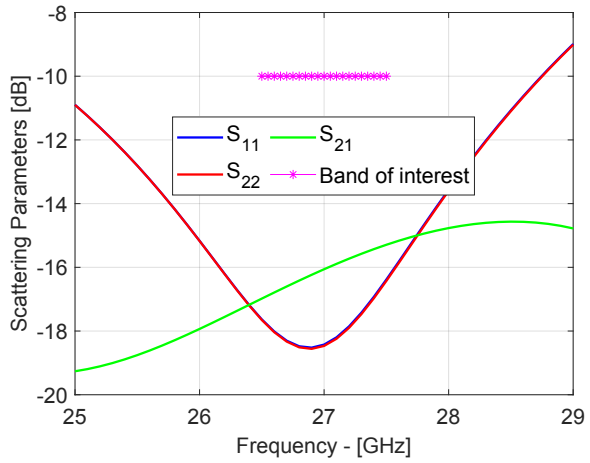

Figure 9.26: Scattering parameters of the unit-cell.

	$\hat{x}-$**pol.**	$\hat{y}-$**pol.**
HPBW $\phi = 0°$	123.9°	109.7°
HPBW $\phi = 90°$	110.4°	123.9°
Peak realized gain $\phi = 0°$	4.23 [dBi]	4.24 [dBi]
Peak realized gain $\phi = 90°$	4.23 [dBi]	4.24 [dBi]

Table 20: Radiation properties at 27 GHz.

The simulated results confirm that the beam extension can still be obtained even after replacing the vertical walls with plated vias. Also, the radiation patterns for both polarizations show a good symmetry, which is a desirable characteristic. It should be observed that, for a given active polarization, the beam extension is not the same in the two orthogonal planes, but nevertheless they both result to be enlarged if compared to the reference patch.

9.5 Array analysis

9.5.1 Infinite array and coupling

When studying phased arrays, especially planar arrays, it is common to carry out the *infinite array analysis*. It allows to get an insight on how the unit-cell would behave if it was placed inside an infinite size array. This means that all the elements experience the same conditions whereas edge effects, which would instead appear in a finite array, are neglected. Though it is important to remark that no infinite size array can exist, the results can be reasonably applied to a very large size finite array [10][18]. The main purpose of this analysis is to obtain the unit-cell's active scattering parameters and active impedance, which account for mutual coupling effects that are due to the presence of neighbouring elements in the array (see Section 9.1). Although it cannot substitute the full simulation of a finite array, it has the great advantage of requiring a limited simulation time. In order to carry it out, a particular simulation setup, shown in Figure 9.27, is required. The first step is to envelope the unit-cell in a vacuum filled airbox. Next, the infinite periodicity is imposed by selecting opposite lateral sides of the box and assigning them to *primary and secondary boundaries*. Basically, the fields that are defined on the primary sides are mapped to the secondary ones. These fields are identical except for a user-selected phase shift that allows to steer the beam. The periodicity is determined by the unit-cell's size, in this case it is $d_x = d_y = L_s = 5\,mm$. To terminate the unit-cell and make it appear as if it radiated in free-space, an absorbing layer is required on the top and bottom sides. There are different available possibilities to realize such layers, in this case, the *PML (Perfectly Matched Layer)* boundaries are used. To simulate the free-space radiation, one should guarantee that at the top and bottom sides no reflections occur, thus the fields impinging on the airbox should be absorbed. If this did not happen, then the simulation results may be incorrect. To avoid this condition, it is also necessary to set the *PML* layer at an adequate distance from the unit-cell. At the very minimum, this distance should be of at least $\lambda_0/4$, but in practice it is recommended to increase it. In this case, the distance is set to $20\,mm$ ($\approx 1.8\lambda_0$) and it was chosen with the aid of the simulation software. Another important step is to include the PML layers inside the definition of the primary and secondary boundaries, as shown below.

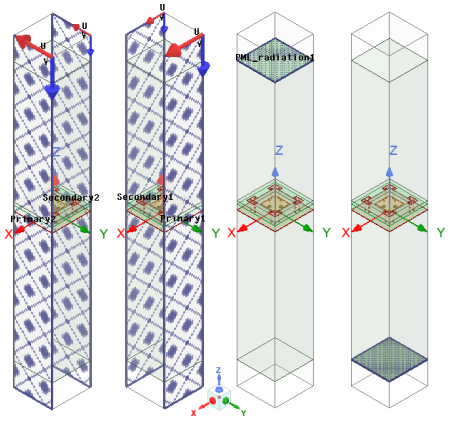

Figure 9.27: Infinite array simulation setup - primary/secondary boundaries and PML layers.

Figure 9.28 reports the active input impedance seen from the $\hat{x}-$polarized port. Due to the symmetry introduced by the infinite periodicity, the active impedance seen from the $\hat{y}-$polarized port is the same. Moreover, the input impedance in the isolated case is also reported for comparison. The results show that when the unit-cell is surrounded by other elements, its input impedance significantly changes if compared to the isolated case. In particular, it becomes largely inductive (positive imaginary part).

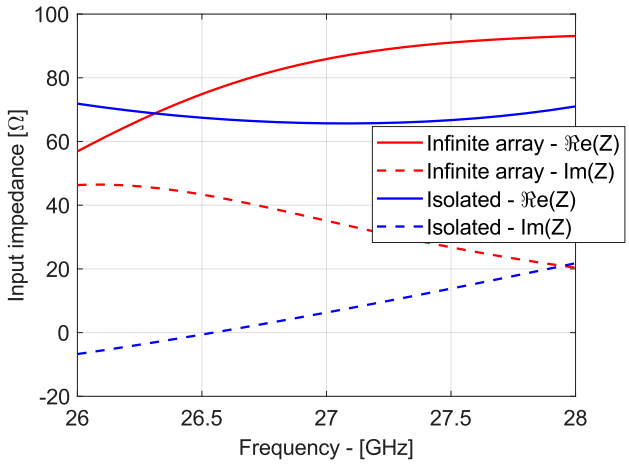

Figure 9.28: Unit-cell input impedance - infinite array vs. isolated.

To better understand the reason for this behavior and to visualize the interaction between unit-cells, a linear 1×3 and a planar 2×2 array configurations were analyzed. It was decided to use such small size arrays in order to reduce simulation times.
Referring to the 1×3 array, two cases are considered:

1. the unit-cells share the same substrate and ground plane, Figure 9.29a;

2. the unit-cells are separated by an air gap, Figure 9.29b.

In the second case, the air gap between the unit-cells is of $d_{gap} = 0.2\,mm \approx \lambda_g/22$.
Then, the electric field magnitude was plotted in the substrate for both the two cases and with only the center element $\hat{y}$-polarization probe excited.

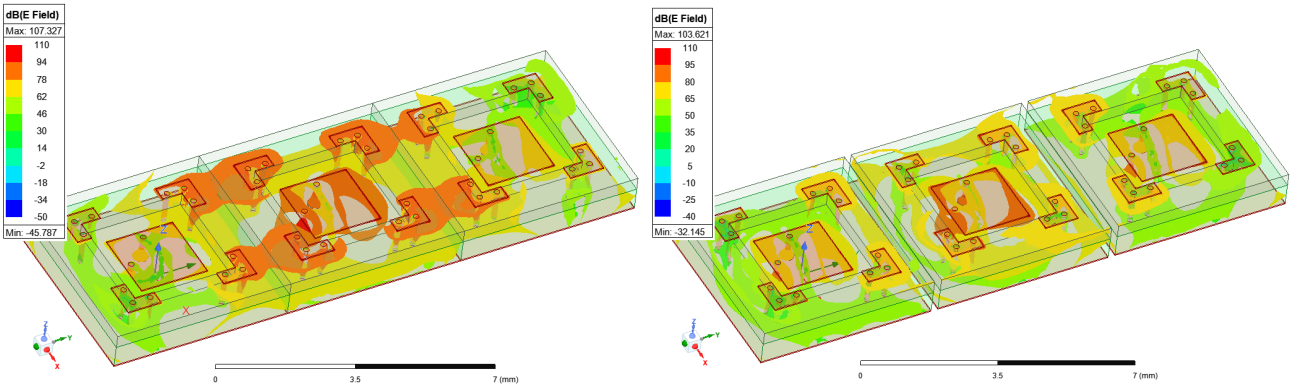

(a) (b)

Figure 9.29: Three unit-cells (a) on a contiguous substrate and ground plane and (b) separated by a small air gap.

Comparing Figures 9.29a and 9.29b, a strong mutual coupling between adjacent vertical vias is observed when the substrate and the ground plane are joined together. Instead, when the air gap is present, the coupling mechanism is disrupted and significantly reduced.
For the case of contiguous substrate and ground plane, the surface current density vector on the ground plane and on the vias is plotted next.

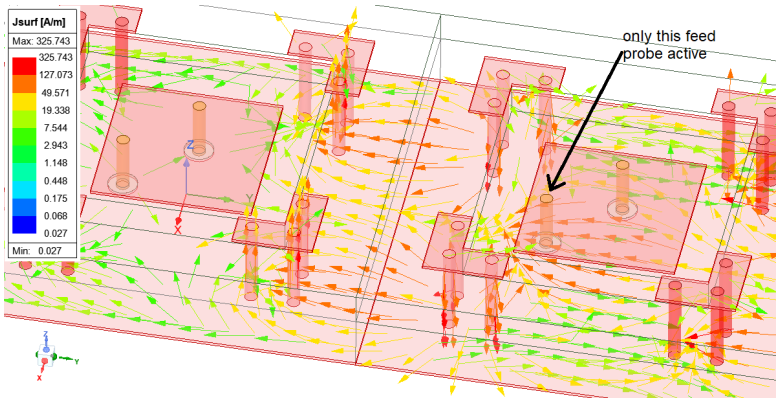

Figure 9.30: Current density vector on ground plane and vertical vias.

Figure 9.30 shows that there is a path for the currents to couple with an adjacent unit-cell. The current goes from one set of vertical vias to another through the ground plane. This is therefore a coupling mechanism whose effect is to make the antenna input impedance change when used inside an array. This variation has a direct influence on the antenna matching, which gets worse.
A very similar behavior was also noted in the 2×2 array. For this case, the surface current density magnitude is reported at different time instants (in the plot shown as phase values) at the central frequency $f_0 = 27\,GHz$. Only the bottom right unit-cell is excited.

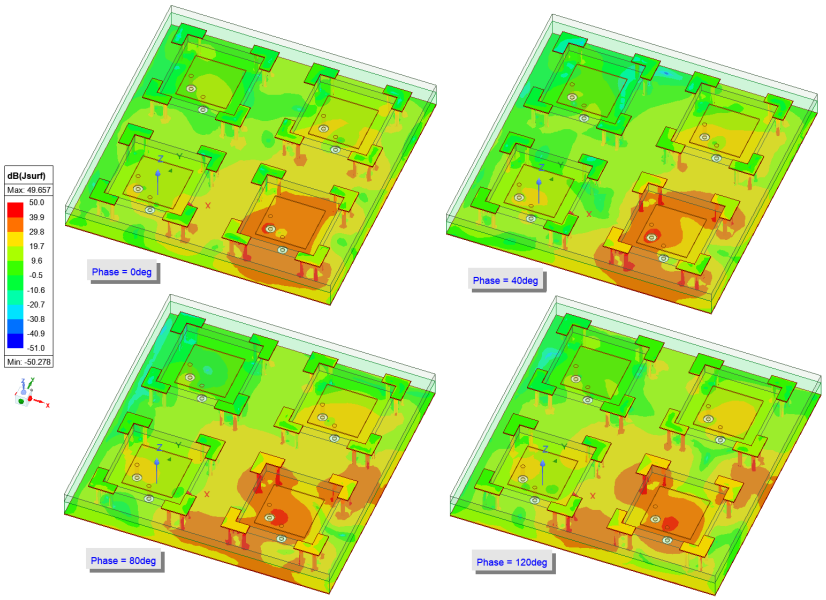

Figure 9.31: Surface current density magnitude - $f_0 = 27$ GHz.

9.5.2 Linear 1×8 array

After observing the interaction that exists between the unit-cells, whether they are separated or not by an air gap, a further analysis was carried out considering a 1×8 array configuration. The main interest is to understand the differences in terms of scattering parameters and scanning capability in the following two cases:

1. the unit-cells share the same substrate and ground plane, with a center-to-center distance of $d_y = 5\,mm = 0.45\lambda_0$;

2. the unit-cells are separated by an air gap of size $d_{gap} = 0.2\,mm$. In this case the center-to-center distance is $d_y = 5.2\,mm \approx 0.47\lambda_0$.

The linear array configuration under analysis is shown in Figure 9.32:

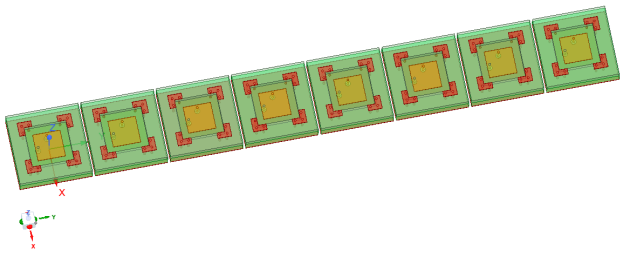

Figure 9.32: 1×8 linear array of the proposed unit-cell.

At first, the reflection coefficients $(S_{11}, S_{22}, ...)$ at all ports are compared in the two cases:

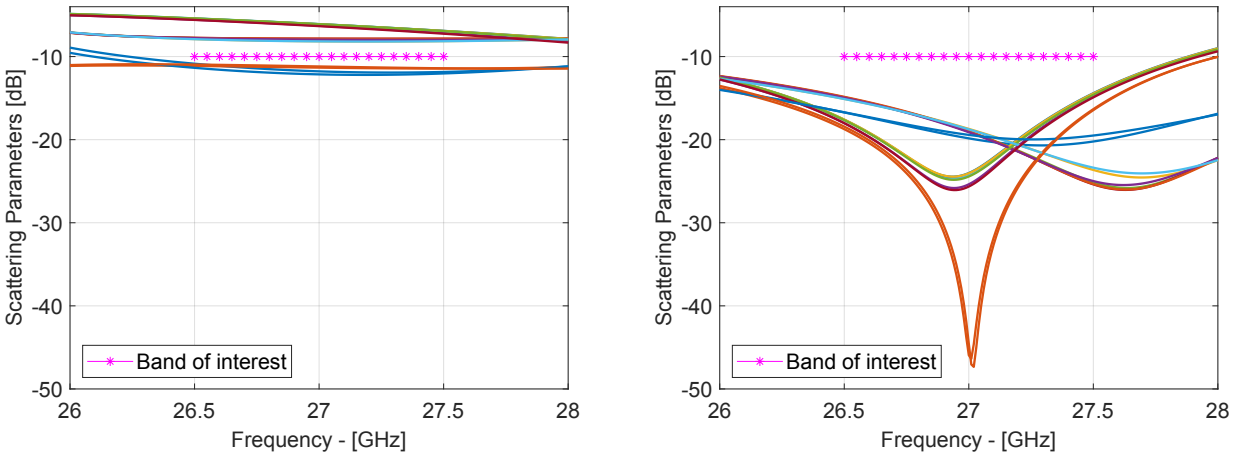

(a) (b)

Figure 9.33: Comparison of the reflection coefficient at all ports of the 1×8 linear array (a) without and (b) with the air gaps.

When the unit-cells are joined together the scattering parameters in Figure 9.33a show that the array is not impedance matched. Instead, when the air gaps are introduced, the scattering parameters in Figure 9.33b show a better behavior, and the cells are almost matched in the band of interest. This large difference between the two cases can be attributed to the coupling mechanism that was previously observed.
The scanning capability was then tested, using one polarization at a time. The ports of the polarization under analysis are supplied with the same signal magnitude but with a linear phase shift between them, while the ports of the other polarization are terminated on a matched load. Given the linear geometry, the array can scan its main beam in only one plane, in this case the yz-plane ($\phi = 90°$). The required phase shift to achieve beam steering was computed using equation (50). Figures 9.34a and 9.34b show the simulated normalized peak realized gain at different scan angles on the $\phi = 90°$ plane, for the two polarizations. These plots compare the results obtained for the 1×8 array with ($d_y = 5.2\,mm$) and without ($d_y = 5\,mm$) the air gap.

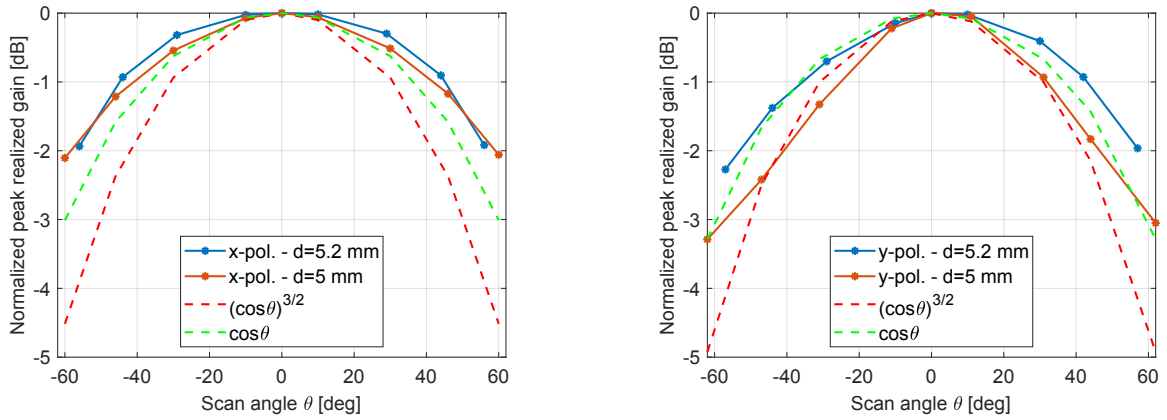

(a) (b)

Figure 9.34: Normalized peak realized gain at $f_0 = 27$ GHz on the $\phi = 90°$ plane (a) $\hat{x}-$polarization (b) $\hat{y}-$polarization.

For the 1×8 linear array with air gaps, the scan-loss at different angles is summarized in Table 21.

Scan angle θ_0	$-56°$	$-44°$	$-29°$	$-10°$	$0°$	$10°$	$29°$	$44°$	$56°$
$\hat{x}-$**pol.** scan-loss [dB]	1.94	0.93	0.32	0.03	0	0.02	0.30	0.90	1.92
Scan angle θ_0	$-57°$	$-44°$	$-29°$	$-10°$	$0°$	$10°$	$30°$	$42°$	$57°$
$\hat{y}-$**pol.** scan-loss [dB]	2.27	1.38	0.70	0.14	0	0.02	0.41	0.93	1.96

Table 21: Scan-loss summary for the 1×8 linear array with air gaps - $\hat{x}$ and $\hat{y}$-pol.

Commenting the results, for the $\hat{x}-$polarization it can be seen that the scanning envelope with or without the air gaps is only slightly affected and the two cases show a similar behavior (approximatelly as $cos\theta$). Instead, the $\hat{y}-$polarization scanning envelope undergoes some more evident changes. Indeed, the case with elements separated by the air gaps shows a better behavior, because it has a smaller scan-loss. This result might suggest that the interaction

between the unit-cells not only affects impedance matching, but it also has an influence on radiation patterns. This fact is further investigated in the following analysis.
The embedded patterns are evaluated next. These are obtained by sequentially exciting the $\hat{x}$ and $\hat{y}$ polarization ports of the fourth element (from the reference system's origin) and while all the other ports are terminated on a matched load. Only the patterns on the $\phi = 90°$ plane are shown, since they belong to the plane on which scanning occurs and therefore directly affect the scan-loss behavior.

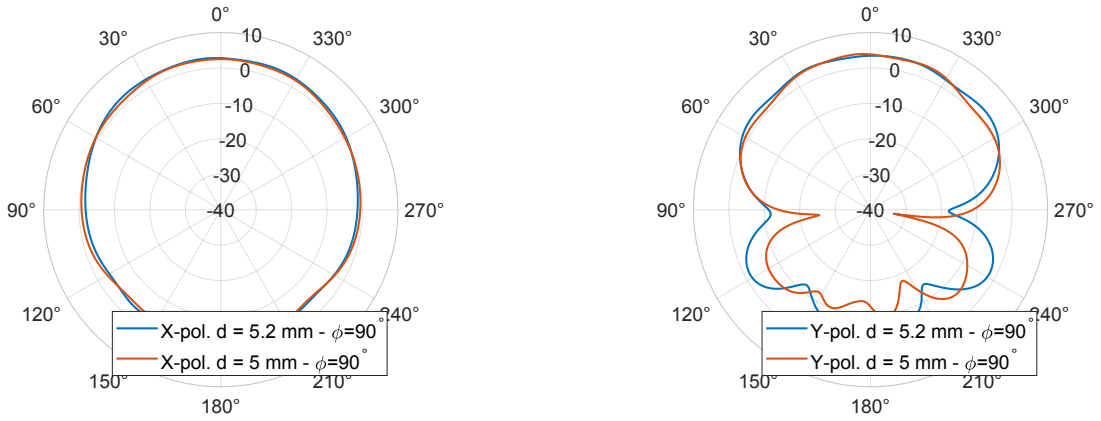

(a) (b)

Figure 9.35: Realized gain comparison of embedded patterns on the $\phi = 90°$ plane (a) $\hat{x}-$polarization (b) $\hat{y}-$polarization.

	HPBW $\hat{x}-$pol.	**HPBW** $\hat{y}-$pol.	**Peak realized gain** $\hat{x}-$pol.	**Peak realized gain** $\hat{y}-$pol.
$d = 5\,mm$	171.3°	84.3°	2.5 [dBi]	4.0 [dBi]
$d = 5.2\,mm$	137.4°	127.9°	2.9 [dBi]	3.6 [dBi]

Table 22: Comparison of embedded patterns' radiation characteristics at 27 GHz, $\phi = 90°$.

Observing the embedded patterns, it appears that they are significantly different compared to the isolated case. These effects can be again attributed to mutual coupling. Recalling that no significant difference was found in the $\hat{x}-$polarized scanning envelopes, this also translates into having similar $\hat{x}-$polarized embedded patterns. On the other hand, the $\hat{y}-$polarized embedded patterns show some more evident differences, especially in their HPBW. When the unit-cells are all joined, the HPBW is reduced ($< 100°$). In fact, inspecting the $\hat{y}-$polarized patterns of Figure 9.35b, it is observed that, at larger angles (around $\pm 60°$), the case of all elements joined ($d = 5mm$) provides a smaller realized gain. This fact can therefore justify the difference in scanning performance that was previously observed. The results also confirm that having embedded patterns with a large HPBW does make a difference in terms of scan-loss, and it can effectively contribute to maintain it below the required threshold. This would be a desirable behavior.

To be noted is that the presence of the air gaps between the cells is not desirable and difficult to realize in practice. It is much more convenient to have all the cells on the same substrate material and to share a common ground plane. Moreover, the aim is to have an array that can scan in more than just one plane, therefore the array geometry should be planar. The following sections investigate these points.

9.5.3 Planar 5×5 array

After assessing the properties of the linear array, a planar 5×5 array of the proposed modified unit-cell is simulated and analyzed. The unit-cells are placed in a square layout with the same center-to-center distance on both the $\hat{x}$ and $\hat{y}$-axes: $d_x = d_y = 5\,mm = 0.45\lambda_0$. In this case, the unit-cells are not separated by any air gap: the ground plane and the substrate material are all joined together. Figure 9.36a shows the planar array under analysis.
The reflection coefficients at all ports of the array $(S_{11}, S_{22}, ...)$ are reported in Figure 9.36b. Given the fact that the unit-cells are all joined together, the coupling mechanism that was shown in the previous analysis makes the cells' input impedance change, compromising impedance matching. This is also shown in Figure 9.37, where the input impedance of the central element of the array is compared to the one of the isolated case.

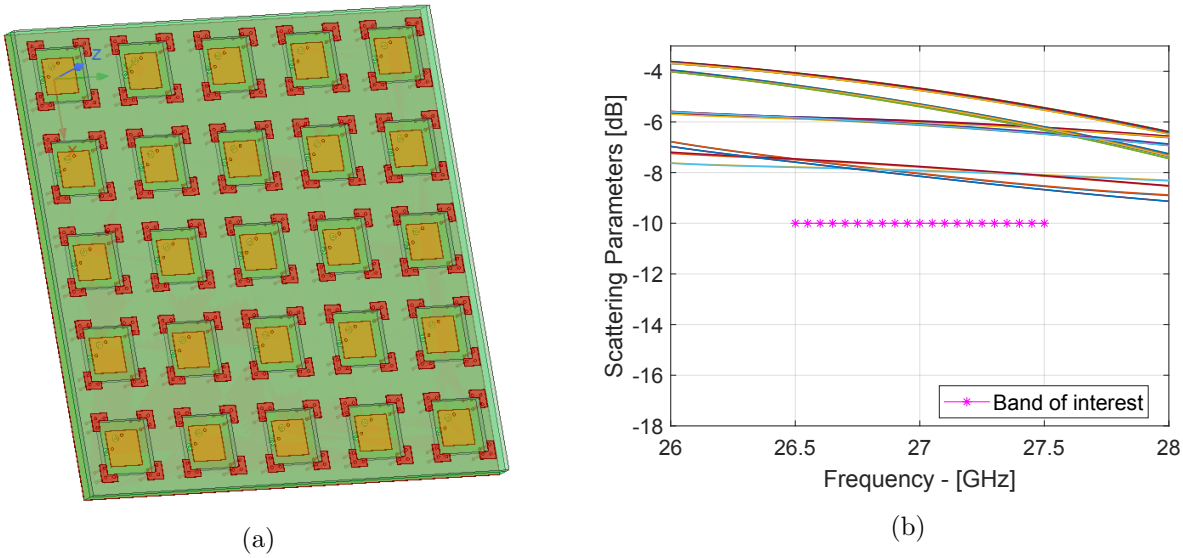

(a) (b)

Figure 9.36: (a) 5×5 array of the proposed unit-cell. - (b) Scattering parameters - all ports.

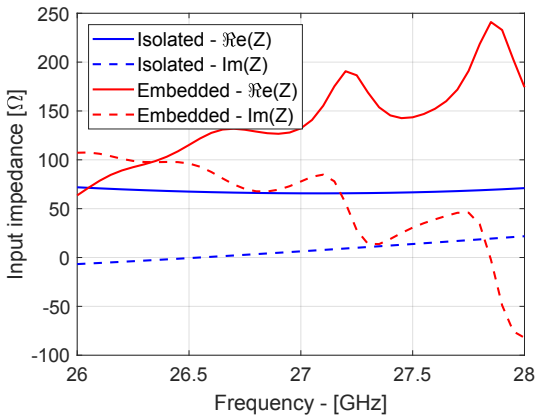

Figure 9.37: Input impedance comparison: isolated vs. embedded.

The embedded patterns are evaluated next. For the sake of brevity, in Figure 9.38 only the $\hat{x}-$polarized patterns on both the principal planes are shown, though the details for both polarizations are reported in the adjacent tables.

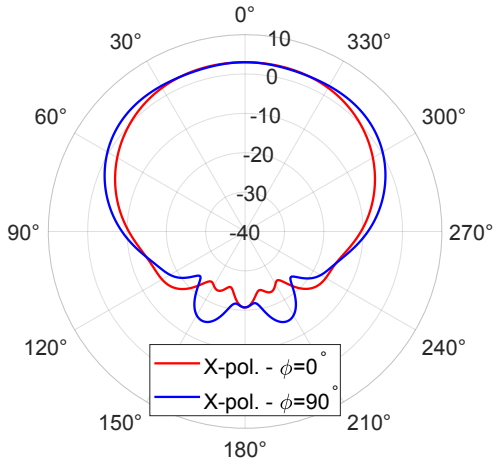

Figure 9.38: Realized gain [dBi] at 27 GHz of the central unit-cell inside the array - $\hat{x}$-pol.

	HPBW $\phi = 0°$	**HPBW** $\phi = 90°$
$\hat{x}$-pol.	94.5°	123.4°
$\hat{y}$-pol.	123.4°	94.5°

Table 23: HPBW of the central unit-cell.

	Peak realized gain at 27 GHz
$\hat{x}$-pol.	2.9 dBi
$\hat{y}$-pol.	3.0 dBi

Table 24: Peak realized gain of the central unit-cell.

Observing the results, the cell's embedded patterns are different from the isolated case. Considering for example the $\hat{x}-$polarization, its HPBW on the $\phi = 0°$ plane has been reduced, while instead it is well extended and $> 120°$ in the $\phi = 90°$ plane. This also suggests that some differences in the scanning behavior on the two planes are to be expected. Moreover, the peak realized gain of the unit-cell is reduced. The reason for this could be attributed to the poor impedance matching.

The scanning behavior is evaluated next and Figures 9.39a, 9.40a, 9.41a, 9.42a show the realized gain patterns at different scan angles. Figures 9.39b, 9.40b, 9.41b, 9.42b show instead the peak realized gain at various scan angles and normalized with respect to the broadside condition. These plots can be used to extract the scan-loss, as previously explained. They also directly compare the behavior of this 5×5 array to the one of reference patch unit-cells.

The comparison serves to better understand the effects that the modified element has on the scan-loss. The results for the $\hat{x}-$polarization are reported first.

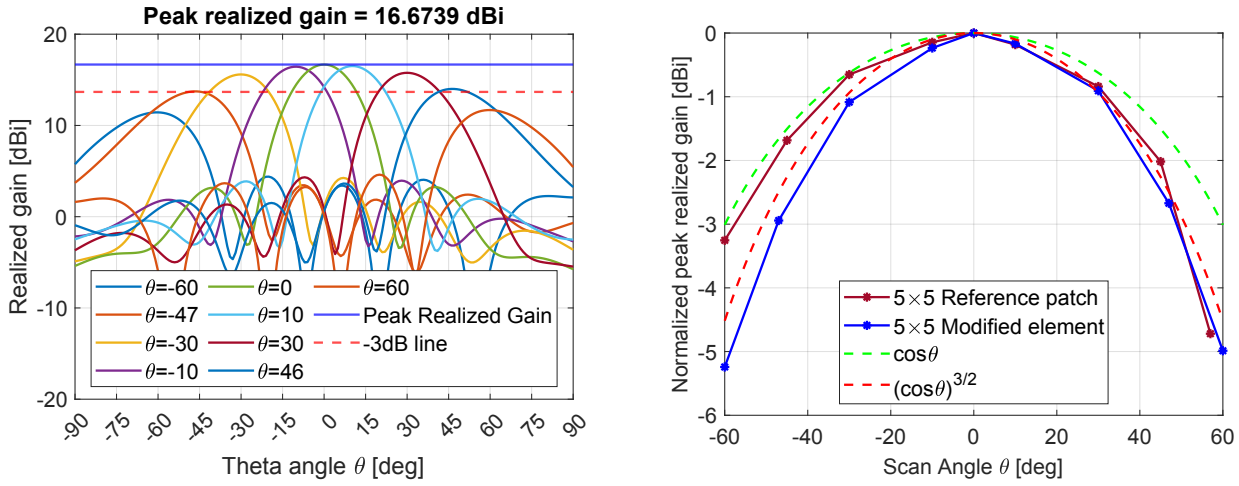

(a) (b)

Figure 9.39: (a) Realized gain - $\phi = 0°$ - $\hat{x}$-pol. (b) Normalized peak realized gain - $\phi = 0°$ - $\hat{x}$-pol.

Scan angle θ_0	$-60°$	$-47°$	$-30°$	$-10°$	$0°$	$10°$	$30°$	$46°$	$60°$
Scan-loss [dB]	5.24	2.94	1.08	0.24	0	0.17	0.91	2.67	4.99

Table 25: Scan-loss summary, 5×5 modified element - $\phi = 0°$ - $\hat{x}-$pol.

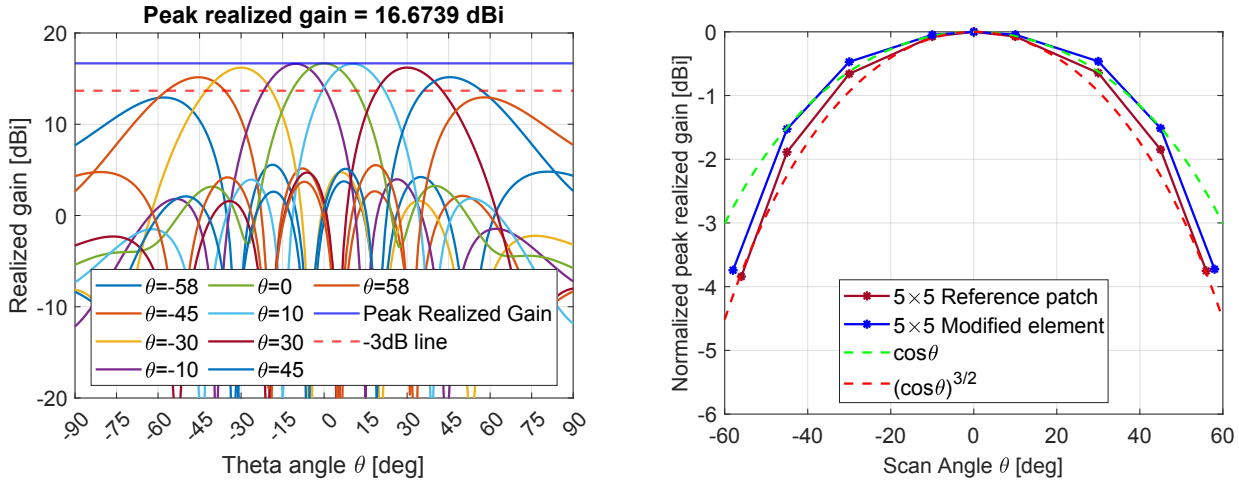

(a) (b)

Figure 9.40: (a) Realized gain - $\phi = 90°$ - $\hat{x}$-pol. (b) Normalized peak realized gain - $\phi = 90°$ - $\hat{x}$-pol.

Scan angle θ_0	$-60°$	$-45°$	$-30°$	$-10°$	$0°$	$10°$	$30°$	$45°$	$59°$
Scan-loss [dB]	3.74	1.53	0.47	0.05	0	0.04	0.46	1.51	3.73

Table 26: Scan-loss summary, 5×5 modified element - $\phi = 90°$ - $\hat{x}-$pol.

The results for the $\hat{y}-$polarization are shown next.

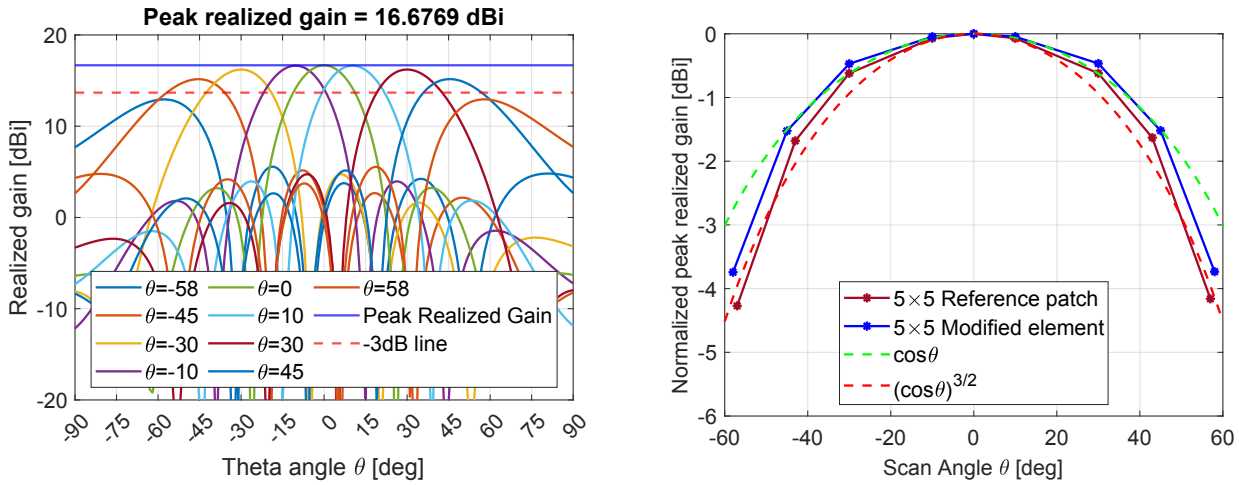

(a) (b)

Figure 9.41: (a) Realized gain - $\phi = 0°$ - $\hat{y}$-pol. (b) Normalized peak realized gain - $\phi = 0°$ - $\hat{y}$-pol.

Scan angle θ_0	$-60°$	$-45°$	$-30°$	$-10°$	$0°$	$10°$	$30°$	$45°$	$59°$
Scan-loss [dB]	3.74	1.52	0.47	0.05	0	0.05	0.47	1.52	3.73

Table 27: Scan-loss summary, 5×5 modified element - $\phi = 0°$ - $\hat{y}-$pol.

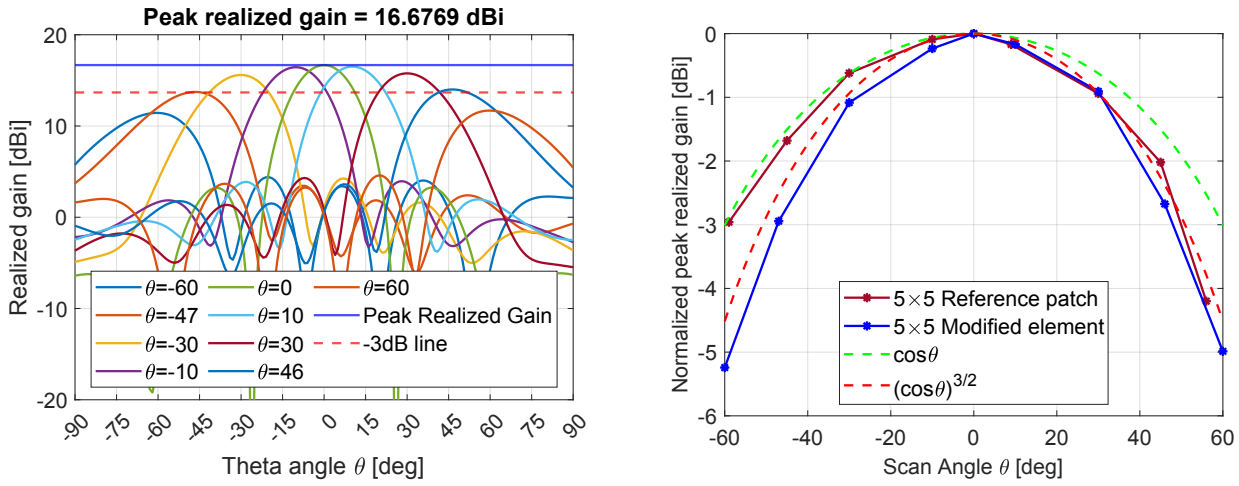

(a) (b)

Figure 9.42: (a) Realized gain - $\phi = 90°$ - $\hat{y}$-pol. (b) Normalized peak realized gain - $\phi = 90°$ - $\hat{y}$-pol.

Scan angle θ_0	$-60°$	$-45°$	$-30°$	$-10°$	$0°$	$10°$	$30°$	$45°$	$59°$
Scan-loss [dB]	5.24	2.95	1.08	0.23	0	0.17	0.91	2.67	4.99

Table 28: Scan-loss summary, 5×5 modified element - $\phi = 90°$ - $\hat{y}-$pol.

Analyzing the results, it is confirmed that there are no grating lobes in the visible range of the array. The peak realized gain of the whole array at broadside is reduced to $\approx 16.7\, dBi$. This result can be related to the poor impedance matching.
For the $\hat{x}-$polarization, the normalized peak realized gain plots show that the proposed modified element does not improve the scan-loss on the $\phi = 0°$ plane. The reason for this could be attributed to the reduced pattern beamwidth. In fact, the embedded pattern HPBW on that plane is significantly reduced, as shown in Figure 9.38 and reported in Table 23. On the $\phi = 90°$ plane, in which the embedded pattern HPBW is larger, the scan-loss behavior shows some improvement, if compared to the 5×5 array of reference patch. This really is the desired behavior. The $\hat{y}-$polarization shows very similar characteristics and it is symmetric compared to the $\hat{x}$ one.
To be noted is that the plots related to radiation patterns shown so far, are always expressed in terms of the realized gain, which does take into account impedance matching (see equation (22)). Therefore, improving it should have beneficial effects on the scan-loss. Moreover, these results have highlighted once again the link that exists between scan-loss and the embedded patterns' HPBW.
The following analysis are therefore aimed at improving impedance matching. To achieve it, in the light of all the above discussion, it will be necessary to mitigate the coupling mechanism between adjacent cells. At the same time, extra care should be taken to assure that the embedded patterns remain extended.

9.5.4 Planar 5×5 array - ground slots

In the effort to find a solution for the coupling issue, the following attempt was made. To disrupt the currents that flow from one element to another, part of the ground plane between adjacent cells is cut by a thin slot. Figure 9.43 shows the current density vector after the slot is cut on the ground plane.

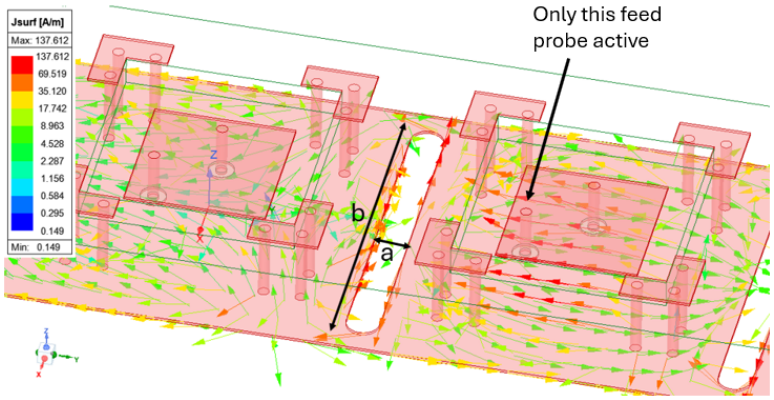

Figure 9.43: Current density vector - Ground plane cut by a thin slot.

The presence of the slot changes the way currents flow on the ground plane.
In order to further observe the effects introduced by the slot, an *infinite array analysis* was carried out using the unit-cell shown in Figure 9.44.

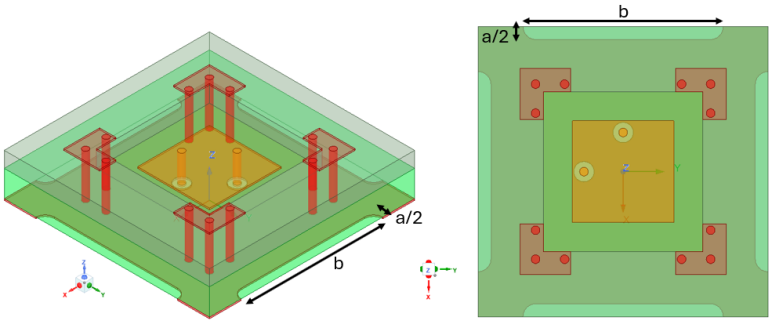

Figure 9.44: Modified unit-cell with the ground slots.

Figures 9.45a and 9.45b show the results of the infinite array simulations at broadside ($\theta = 0°$). The analysis compares the behavior of the unit-cell without and with the slot on the ground plane. As previously shown, when the ground slot is not present, the unit-cell's input impedance shows a strong inductive behavior (positive imaginary part), thus compromising impedance matching. Instead, when the slot is introduced, the impedance imaginary part is reduced, but the center frequency is shifted towards the lower part of the band of interest. To center it back, the length of the patch was tuned and reduced, from $L = 1.9\,mm$ to $L^{'} = 1.8\,mm$. The dimensions of the slot on the ground plane were adjusted during the infinite array simulations, and in the end they result to be: $a = 0.45\,mm$, $b = 3.45\,mm$.

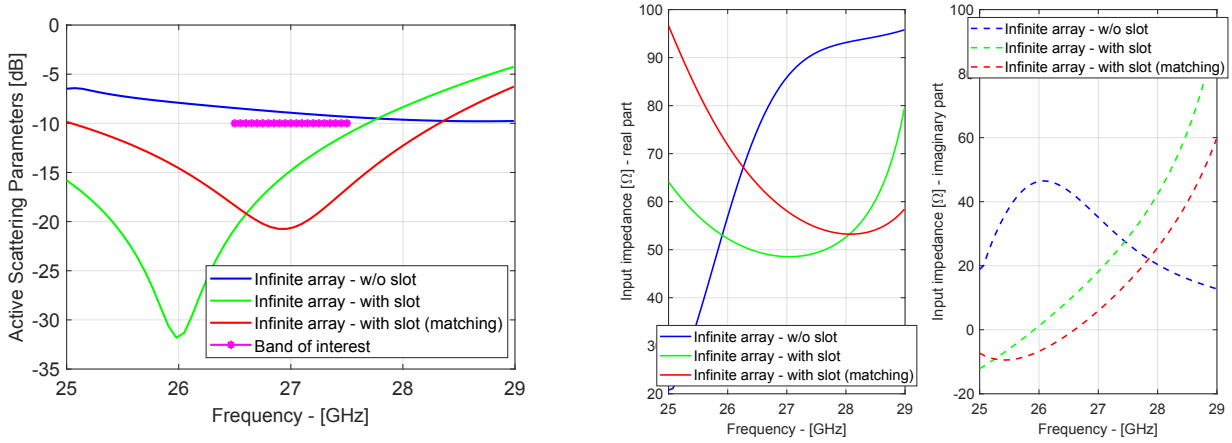

(a) (b)

Figure 9.45: Infinite array (a) Active S-param. comparison at broadside. - (b) Active-Z comparison at broadside.

To be noted is the fact that these results report the active scattering parameters and the active impedance for an infinite array. Although the cell appears to be impedance matched in this analysis, this does not imply that all the cells in a finite array will be.

Using the unit-cell that was just tuned in the infinite array analysis, a finite array is simulated next. The array is in a planar 5×5 layout and it is shown in Figure 9.46. Elements are spaced with the same distance on both the $\hat{x}$ and $\hat{y}$ axes: $d_x = d_y = 5\,mm = 0.45\lambda_0$. Please note the presence of the slots on the ground plane.

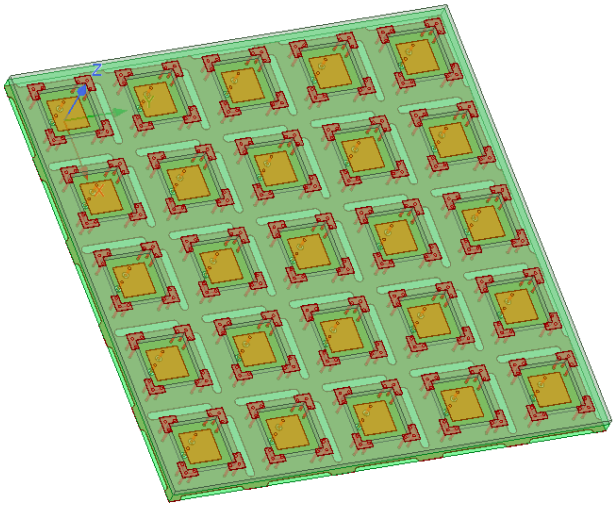

Figure 9.46: 5×5 array using the ground slots.

The reflection coefficients (S_{11}, S_{22}, ...) at all ports are shown in the following Figures 9.47a and 9.47b.

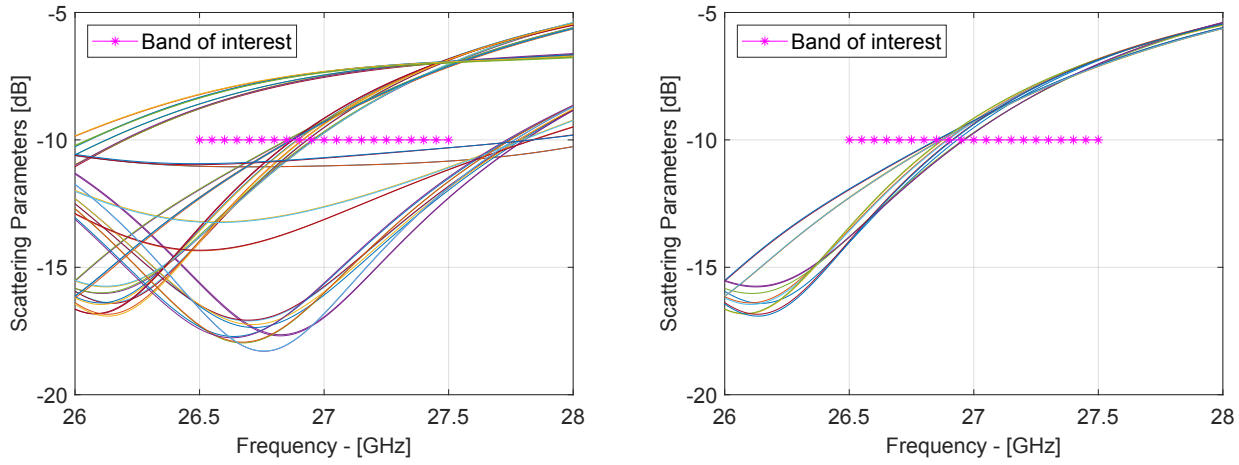

(a) (b)

Figure 9.47: (a) Scattering parameters - all ports. (b) Scattering parameters - inner ports.

The behavior of the scattering parameters shows that not all the elements inside the array are matched in the band of interest. Also, the large variability of the parameters is symptom of the fact that depending on the position of the element, (i.e. in the corner, on the edge or in the center of the array) its impedance changes. The cells that are more in the center of the array (i.e. the embedded 3×3 array, excluding the outermost cells) are the ones that are fully surrounded by other elements. The scattering parameters for these cells are reported in Figure 9.47b. Even if they show a similar behavior, their working frequency is shifted towards the lower part of the band. Therefore, impedance matching remains a critical issue.
Next, to extract the embedded patterns, the central element is excited while all the remaining ports are terminated on a matched load. For symmetry, only the $\hat{x}-$polarized patterns are shown but the details for both are reported in the adjacent tables.

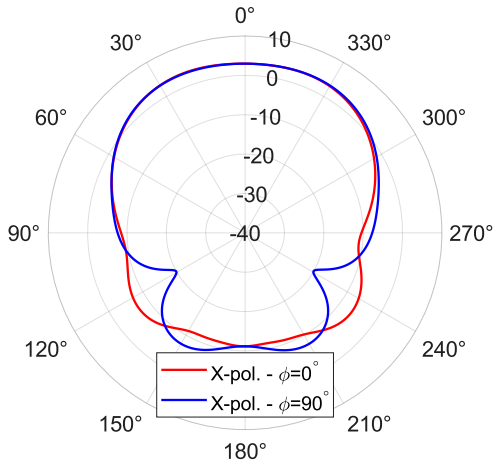

Figure 9.48: Realized gain [dBi] at 27 GHz of the central unit-cell inside the array - $\hat{x}$-pol.

	HPBW $\phi = 0°$	**HPBW** $\phi = 90°$
$\hat{x}$-pol.	99.5°	104.6°
$\hat{y}$-pol.	104.5°	99.6°

Table 29: HPBW of the central unit-cell.

	Peak realized gain at 27 GHz
$\hat{x}$-pol.	3.5 dBi
$\hat{y}$-pol.	3.5 dBi

Table 30: Peak realized gain of the central unit-cell.

The embedded patterns that result inside the array are once again altered. The most critical fact is that the HPBW significantly decreased and the patterns have a narrow beamwidth. This also means that no improvement on the scan-loss is expected.
In Figure 9.49, the electric field magnitude (at 27 GHz) inside the substrate is plotted when only the array center element $\hat{x}-$polarization probe is excited. A strong concentration of electric field is observed over the ground plane slots. These apertures appear to be acting as other sources of radiation, which may contribute to alter the overall radiation pattern.

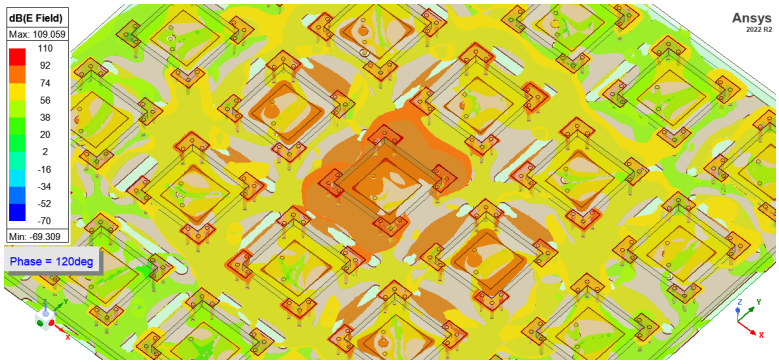

Figure 9.49: Electric field magnitude inside the substrate $[V/m]_{dB}$.

All in all, the use of the ground slots did not yield the expected results and this strategy is not effective.
To complete the analysis, the scanning characteristics for this 5×5 array are reported for the $\hat{x}-$polarization. The $\hat{y}-$polarization is omitted for simplicity, but it resulted to have a very similar behavior.

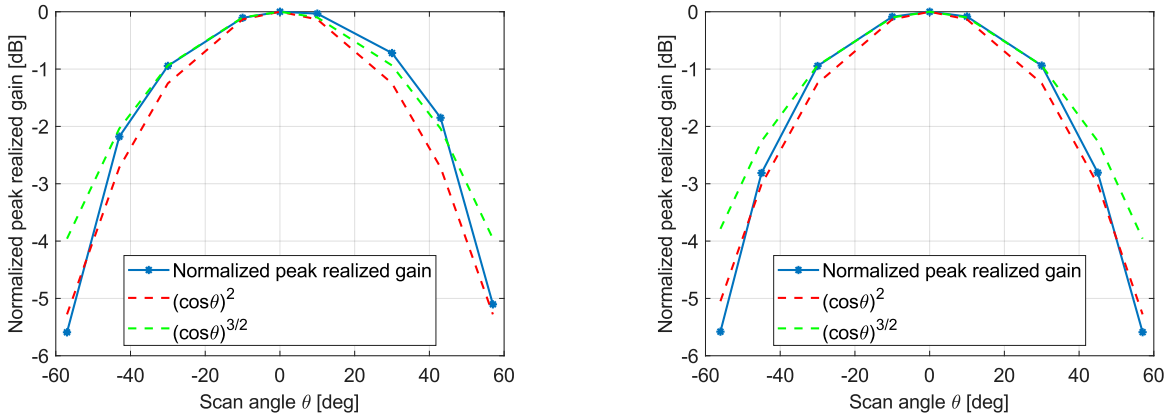

(a) (b)

Figure 9.50: (a) Normalized peak realized gain - $\phi = 0°$ - $\hat{x}$-pol. - (b) Normalized peak realized gain - $\phi = 90°$ - $\hat{x}$-pol.

Scan angle θ_0	$-57°$	$-43°$	$-30°$	$-10°$	$0°$	$10°$	$30°$	$43°$	$57°$
Scan-loss [dB] $\phi = 0°$	5.59	2.18	0.94	0.09	0	0.03	0.72	1.85	5.10
Scan-loss [dB] $\phi = 90°$	5.58	2.81	0.94	0.09	0	0.09	0.94	2.81	5.59

Table 31: Scan-loss summary - $\phi = 0°$ & $\phi = 90°$ - $\hat{x}$-pol.

It is therefore confirmed that the reduced HPBW of the embedded patterns in Figure 9.48 also results in a limited scanning capability. At large angles its behavior can be approximated as $(cos\theta)^2$, which is not desirable.

9.5.5 Planar 5×5 array - decoupling loops

After the previous attempt, a different approach was followed. As reported in [17], by interposing some metallic loops in between adjacent unit-cells, it should be possible to influence how unit-cells couple. The loops, whose geometry is reported in Figure 9.51b, are placed on the same metallic layer of the patch radiating element, embedded in between the two dielectric layers. Their working mechanism was initially tested in a 2×2 array configuration. The following results were obtained using loops whose dimensions are: $q = s = 1\ mm$, $t = 0.86\ mm$ and $r = 0.1\ mm$. Interestingly, the loop's length ($l = 3.8\ mm$) is close to $\lambda_g \approx 4.5\ mm$, where λ_g is the wavelength in the substrate at $27\ GHz$. Also, the loops are not closed, but they are interrupted at two points to avoid the induced currents to flow in a closed loop. As it was mentioned, when multiple cells are put close together, their impedance imaginary part becomes more inductive (positive imaginary part). With the introduction of the decoupling loops it is possible to compensate for this behavior. In fact, the loops seem to provide a capacitive contribution. In this way, the impedance imaginary part could be brought close to zero. The presence of the loops also influences the behavior of the currents on the ground plane, as shown in Figure 9.51a. Here, the surface current density on metallic parts is plotted at different time instants. In this case, only the bottom right unit-cell is excited. From a qualitative point of view, the currents that flow on the ground plane appear to be more "contained", in the sense that a less strong current couples with adjacent elements. This effect is more evident if compared to Figure 9.31, where instead no loops are present.

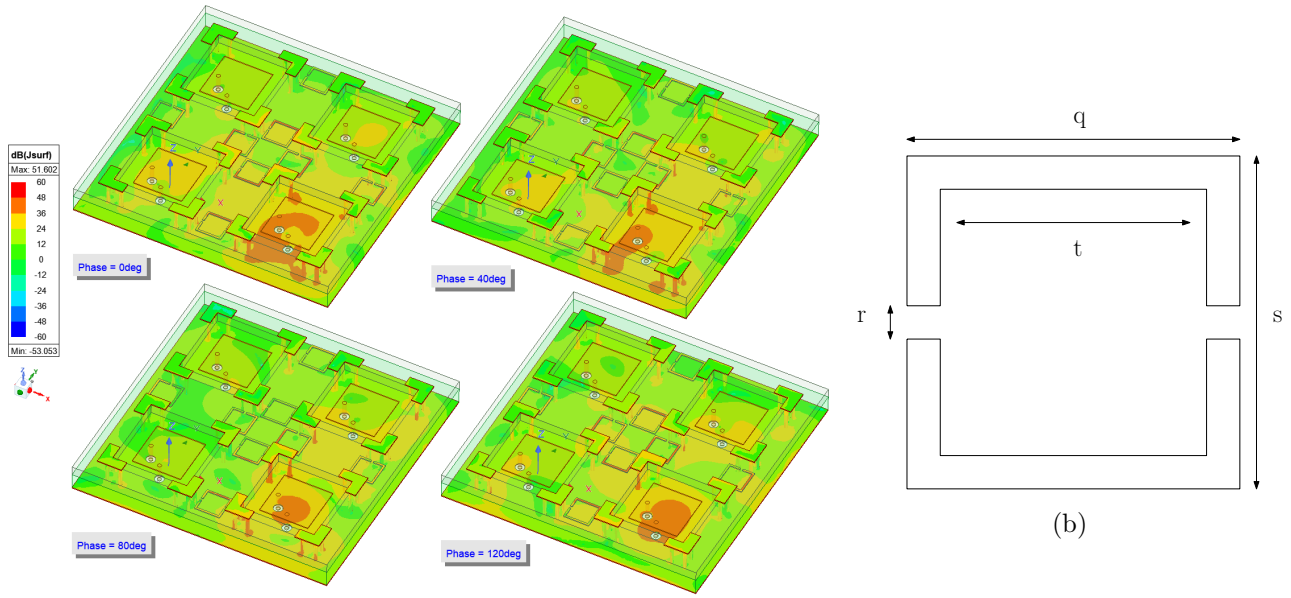

(a) (b)

Figure 9.51: (a) 2×2 array with decoupling loops, surface current density $[A/m]_{dB}$ at different time instants. - (b) Geometry of a decoupling loop.

The following Figures 9.52a and 9.52b compare the scattering parameters at all the ports of the 2×2 array when the loops are present and absent, respectively.

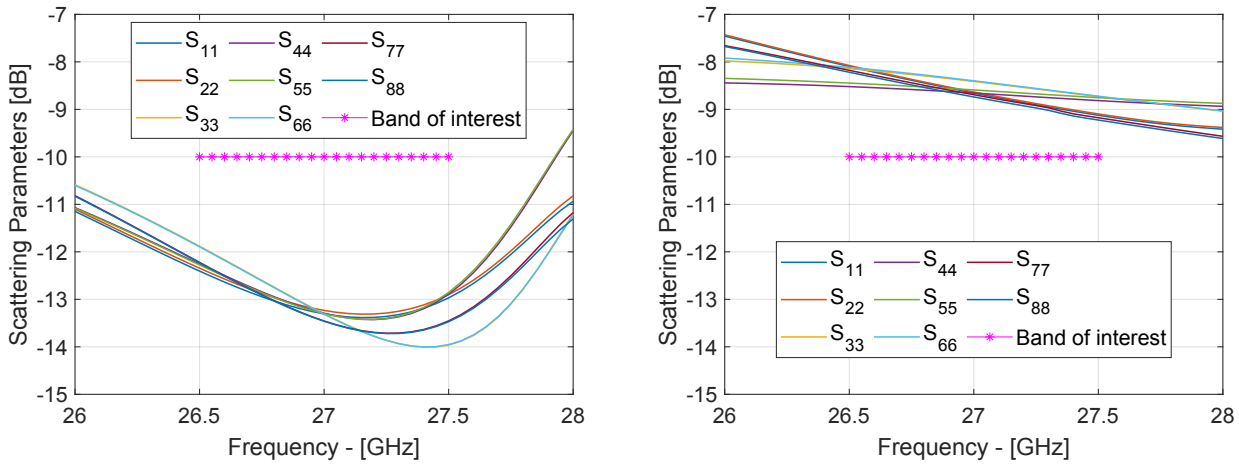

(a) (b)

Figure 9.52: Scattering parameters at all ports of a 2×2 array (a) with and (b) without decoupling loops.

It is evident that without the decoupling loops, the unit-cells are totally impedance mismatched. Instead, with the loops in place, a much more behaved result could be achieved.
The decoupling loops were then applied to simulate a larger 5×5 array, shown in Figure 9.53. In this case, the loops did not change dimensions, which remain $q = s = 1\,mm$, $t = 0.86\,mm$ and $r = 0.1\,mm$, and they are still embedded in between the two dielectric layers, on the same metal layer of the patch. Moreover, note that the ground plane is not interrupted by any kind of slots, it is a continuous metallic layer shared by all the array elements, as it should be. Also note that no air gaps are present between elements. Therefore all unit-cells are on the same substrate material. The center-to-center distance between elements is once again the same on both the $\hat{x}$ and $\hat{y}$ axes: $d_x = d_y = 5\,mm = 0.45\lambda_0$.

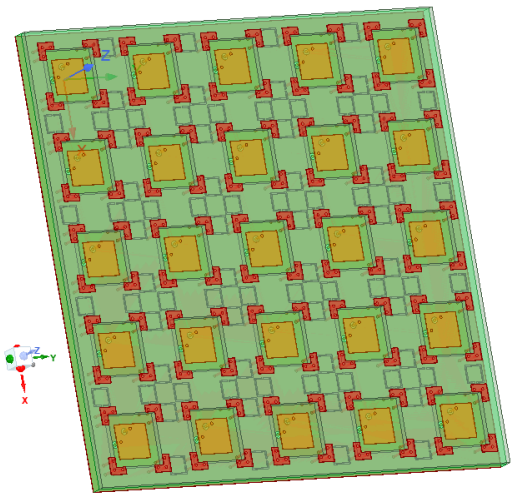

Figure 9.53: 5×5 array using the decoupling loops.

The reflection coefficients at all ports $(S_{11}, S_{22}, ...)$ of the 5×5 array are reported in Figure 9.54a.

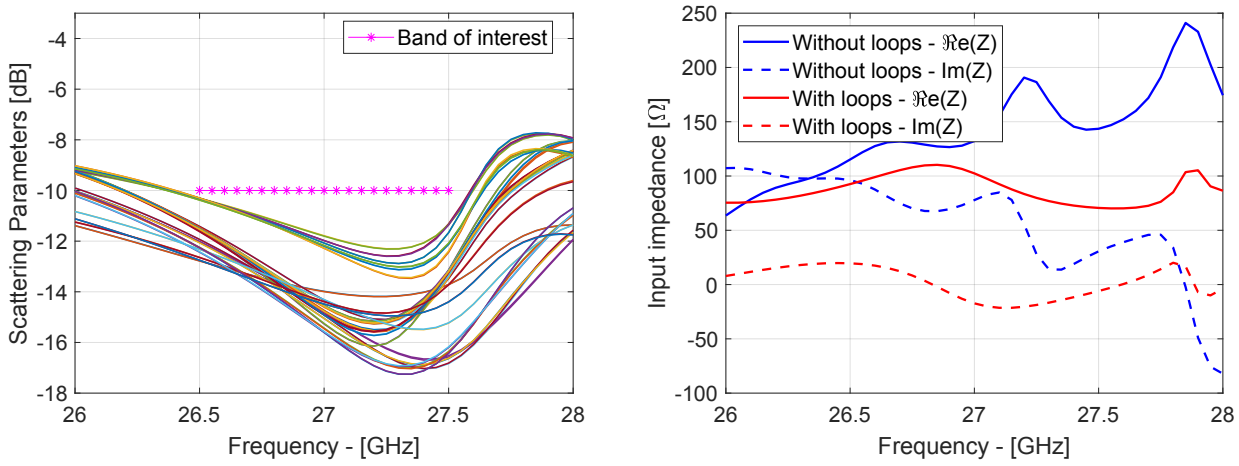

(a) (b)

Figure 9.54: (a) Scattering parameters at all ports of the 5×5 array. - (b) Input impedance of the central element of the 5×5 array.

In this case, the reflection coefficients for all the unit-cells appear to be almost matched in the band of interest. This result could be obtained after adjusting some parameters with respect to the original design in Table 19. The modifications regard the patch length, from $L = 1.9\,mm$ to $L^{'} = 1.92\,mm$, and the position of the feeding probe, from $inset = 0.2\,mm$ to $inset = 0.25\,mm$. All the other parameters remained unchanged. The decoupling loops allowed to achieve better impedance matching results, if compared to the case that did not use them and also to the one that employed the slots on the ground plane.
Figure 9.54b shows instead how the input impedance of the central element of the 5×5 array changes with or without the presence of the decoupling loops. The comparison shows that the loops can indeed offer a capacitive contribution to compensate the initially inductive behavior. This allows to make the impedance imaginary part close to zero.

Next, the embedded patterns are evaluated as usual: the array center element is excited while all the others are terminated on a matched load. Only the $\hat{x}-$polarized patterns are shown, but the details for both polarizations are reported in the adjacent tables.

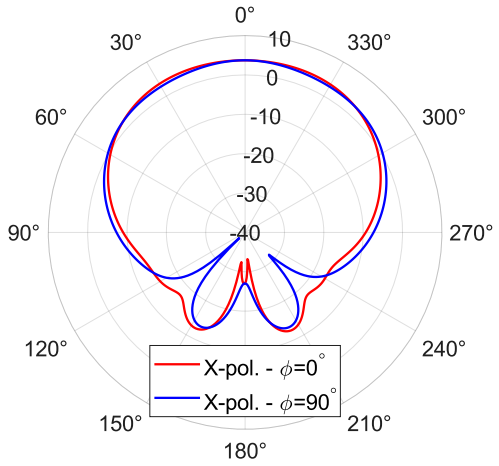

Figure 9.55: Realized gain [dBi] at 27 GHz of the central unit-cell inside the array - $\hat{x}$-pol.

	HPBW $\phi = 0°$	**HPBW** $\phi = 90°$
$\hat{x}$-pol.	106.5°	114.7°
$\hat{y}$-pol.	114.7°	106.2°

Table 32: HPBW of the central unit-cell.

	Peak realized gain at 27 GHz
$\hat{x}$-pol.	3.7 dBi
$\hat{y}$-pol.	3.7 dBi

Table 33: Peak realized gain of the central unit-cell.

It is observed that the embedded pattern's HPBW in the $\phi = 0°$ plane is still smaller compared to the isolated case. As a final step, the array radiation patterns at different scan angles in the two principal planes, for both the polarizations, are shown in Figures 9.56a, 9.57a, 9.58a, 9.59a. The scanning envelopes of Figures 9.56b, 9.57b, 9.58b, 9.59b, directly compare the results for this array to the one of reference patch.

The results for the $\hat{x}-$polarization are reported first.

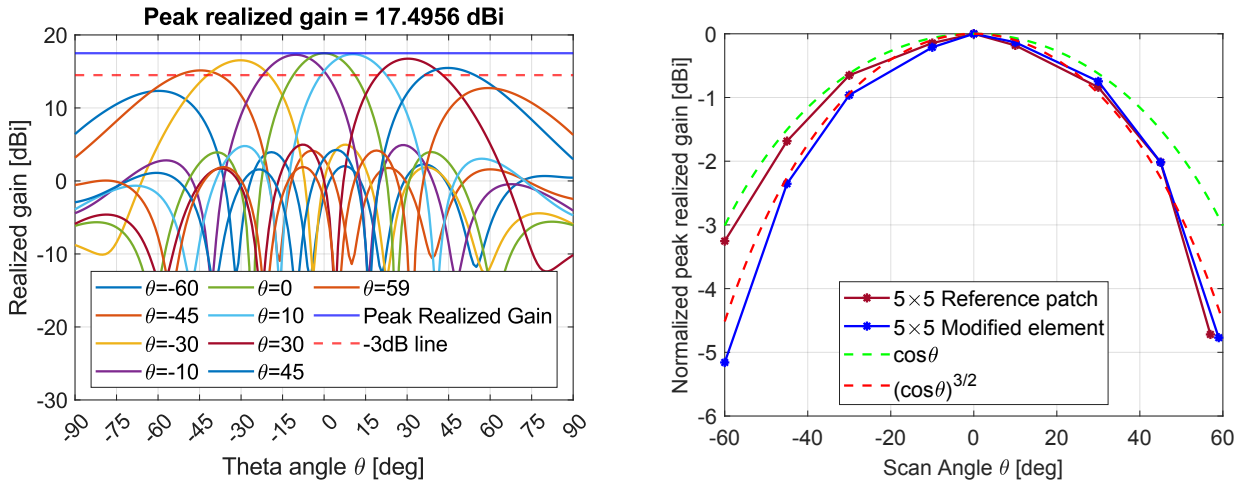

(a) (b)

Figure 9.56: (a) Realized gain - $\phi = 0°$ - $\hat{x}$-pol. (b) Normalized peak realized gain - $\phi = 0°$ - $\hat{x}$-pol.

Scan angle θ_0	$-60°$	$-45°$	$-30°$	$-10°$	$0°$	$10°$	$30°$	$45°$	$59°$
Scan-loss [dB]	5.16	2.35	0.96	0.13	0	0.13	0.75	2.02	4.77

Table 34: Scan-loss summary, 5×5 decoupling loops. - $\phi = 0°$ - $\hat{x}-$pol.

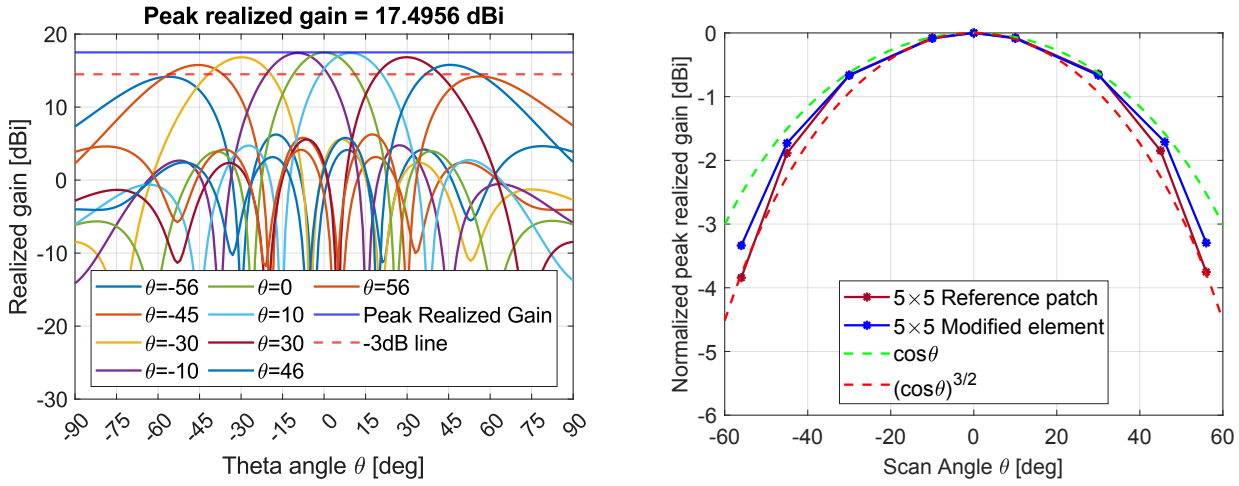

(a) (b)

Figure 9.57: (a) Realized gain - $\phi = 90°$ - $\hat{x}$-pol. (b) Normalized peak realized gain - $\phi = 90°$ - $\hat{x}$-pol.

Scan angle θ_0	$-56°$	$-45°$	$-30°$	$-10°$	$0°$	$10°$	$30°$	$46°$	$56°$
Scan-loss [dB]	3.34	1.73	0.67	0.09	0	0.09	0.66	1.71	3.29

Table 35: Scan-loss summary, 5×5 decoupling loops. - $\phi = 90°$ - $\hat{x}-$pol.

The analysis continues with the $\hat{y}-$polarization.

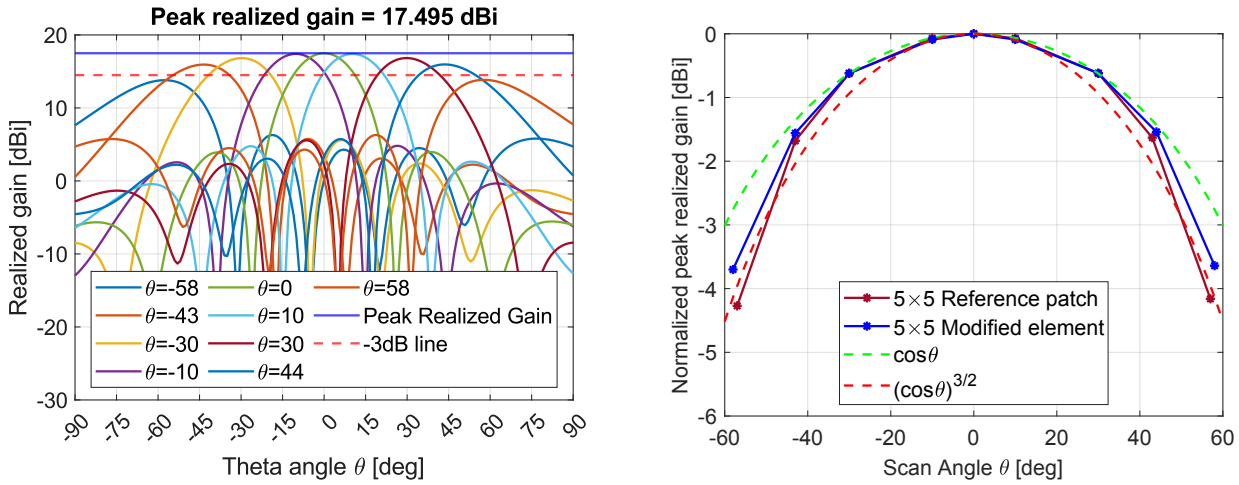

(a) (b)

Figure 9.58: (a) Realized gain - $\phi = 0°$ - $\hat{y}$-pol. (b) Normalized peak realized gain - $\phi = 0°$ - $\hat{y}$-pol.

Scan angle θ_0	$-58°$	$-43°$	$-30°$	$-10°$	$0°$	$10°$	$30°$	$44°$	$58°$
Scan-loss [dB]	3.70	1.56	0.62	0.09	0	0.09	0.62	1.54	3.64

Table 36: Scan-loss summary, 5×5 decoupling loops. - $\phi = 0°$ - $\hat{y}-$pol.

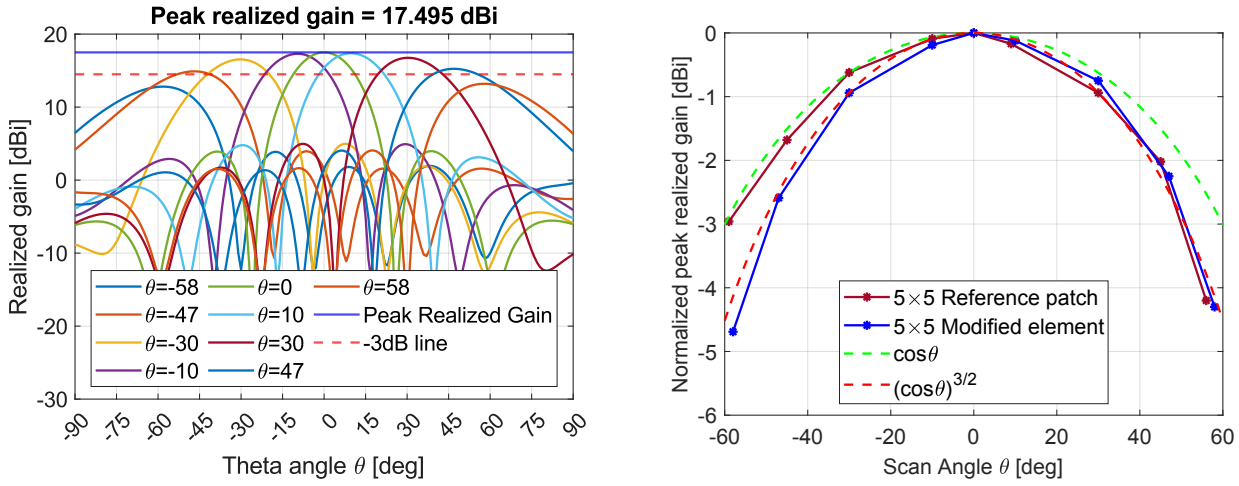

(a) (b)

Figure 9.59: (a) Realized gain - $\phi = 90°$ - $\hat{y}$-pol. (b) Normalized peak realized gain - $\phi = 90°$ - $\hat{y}$-pol.

Scan angle θ_0	$-58°$	$-47°$	$-30°$	$-10°$	$0°$	$10°$	$30°$	$47°$	$58°$
Scan-loss [dB]	4.69	2.59	0.94	0.19	0	0.12	0.75	2.25	4.30

Table 37: Scan-loss summary, 5×5 decoupling loops. - $\phi = 90°$ - $\hat{y}-$pol.

9.5.6 Final overview

At this point, it is worth to collect and compare all the results regarding isolated and embedded patterns. This is done in the summary proposed in Table 38. From the beginning, it was remarked that the HPBW is an important unit-cell parameter for wide-angle beam-scanning arrays. In fact, a large HPBW is beneficial to mitigate the scan-loss at large angles. This is the reason why a lot of attention was put in trying to achieve as large values of HPBW as possible.

	Polarization	**HPBW** $\phi = 0°$	**HPBW** $\phi = 90°$	Reference
Isolated reference patch	$\hat{x}-$pol.	96.9°	100.5°	Figure 9.5
	$\hat{y}-$pol.	100.4°	96.7°	
Reference patch 5×5 array embedded pattern	$\hat{x}-$pol.	117°	107°	Figure 9.11
	$\hat{y}-$pol.	107°	117°	
Isolated modified element	$\hat{x}-$pol.	123.9°	110.4°	Figure 9.25
	$\hat{y}-$pol.	109.7°	123.9°	
Modified element 5×5 array embedded pattern	$\hat{x}-$pol.	94.5°	123.4°	Figure 9.38
	$\hat{y}-$pol.	123.4°	94.5°	
Ground slots 5×5 array embedded pattern	$\hat{x}-$pol.	99.5°	104.6°	Figure 9.48
	$\hat{y}-$pol.	104.5°	99.6°	
Decoupling loops 5×5 array embedded pattern	$\hat{x}-$pol.	106.4°	114.7°	Figure 9.55
	$\hat{y}-$pol.	114.7°	106.2°	

Table 38: HPBW comparison summary.

The work started with the isolated reference patch and with its 5×5 array. After observing the characteristics of the two, and in order to improve the scan-loss of the array, a modified unit-cell was designed using the *vertical wall loading* method, with the precise intent to make it have a large HPBW. In fact, comparing the two isolated cases, the modified element shows a larger HPBW, compared to the reference patch, which suggests that the proposed method can achieve the desired improvement.

Some challenges were faced while trying to translate these benefits into the design of a wide-angle scanning array. As the modified unit-cell is arranged in a planar (or even linear) array configuration, its input impedance and radiation pattern change in a way that is difficult to predict analytically, because mostly dependent on mutual coupling effects. For this reason, one can take into account these effects by evaluating the array embedded patterns. These patterns are obtained by exciting the array center element while all the others are terminated on a matched load. In this work, the interest is to make the embedded patterns have as a large value of HPBW as possible. In fact, if this condition is satisfied, then the scan-loss can be improved. Several arrays were then simulated to understand how the modified element behaves when surrounded by other ones. Initially, a 5×5 array was considered (Section 9.5.3). Apart from successfully rejecting the grating lobes, it showed that the embedded pattern's HPBW was

significantly reduced in one of the two principal planes. This negatively affected the scan-loss on that plane, making it comparable with the array of reference patch. Instead, on the other plane, where the HPBW was larger, the scan-loss could be improved. The array also showed an unsatisfactory impedance matching.
After that, the focus was turned into achieving better matching while also trying to disrupt the coupling mechanism between unit-cells. The first attempt was the one which used the ground plane slots (Section 9.5.4). Even if they had an influence on the cell's impedance, they were not sufficient to achieve good enough levels of matching. Moreover, the slots had the effect of significantly reducing the embedded pattern's HPBW in both the principal planes. This then reflected into a poor scanning capability of the array.
A second attempt was carried out and the decoupling loops were introduced (Section 9.5.5). In this case, the embedded pattern's HPBW was partially restored. This change could be attributed to the improved impedance matching and to the fact that no slots on the ground plane were present. Still, the pattern's HPBW was not sufficiently extended to show any major improvement in scan-loss with respect to the reference patch array. In fact, the embedded patterns' HPBW for these two cases were similar. This was shown in Figures 9.56b, 9.57b, 9.58b, 9.59b, where the scan-loss for the two cases were directly compared. Additionally, the array with decoupling loops was still capable of suppressing the grating lobes, also at large angles. The side-lobe level (SLL) at broadside was $SLL_{\theta_0=0^\circ} \approx -13\,dB$, while at large angles it increased up to a maximum of $\approx -7\,dB$.

10 Conclusions

In this work, the propagation characteristics of mm-Waves have been explored. This frequency range will be the key enabler for future multi-Gbit wireless communication systems, given its large availability of spectrum resources. Higher frequencies pose new challenges. Among them, the increased propagation losses negatively affect network coverage. Small communication cells and network controlled repeaters (NCRs) will allow to overcome these issues. In this framework, highly directive antennas, in the form of beam-scanning phased arrays, will be exploited to obtain highly directive beams. With them, radiated energy can be precisely focused toward the direction of interest, thus overcoming the increased propagation losses. Typically, antenna arrays are designed by arranging multiple unit-cell elements close together, with an inter-element distance that is usually below $\lambda_0/2$, where λ_0 is the wavelength in free-space at the desired working frequency. Small inter-element spacing is fundamental to suppress the grating lobes. These not only radiate energy toward unwanted directions, but they also represent a source of interference. Small spacing also worsens mutual-coupling between array unit-cells. Coupling brings unwanted effects on both the cell's input impedance and pattern characteristics. For beam-scanning arrays, the most desired feature is being able to scan the main beam in a wide angular region, while maintaining good impedance matching and the gain as high as possible. This is not a trivial task, as both impedance and gain deteriorate for increasing scan angles. Conventional radiating elements, such as microstrip patch antennas, typically have broadside radiation patterns whose gain rapidly decreases at large angles. This has a negative influence on the scanning performance of the array. The focus should be therefore put toward reducing this scan-angle dependency.

This thesis was aimed at the study of how to design a wide-angle beam-scanning phased array intended to be used in an NCR device. The objective was to steer the main beam in the wide angular region of $\pm 60°$ for both the azimuth and elevation planes. Moreover, this should be achieved while adopting two linear polarizations (H and V). Initially, the focus was put in the design of an array of common microstrip patch antennas. This allowed to explore the aforementioned effects, including the scan-angle dependency of impedance matching and realized gain. The scan-loss was also analyzed and it was found that indeed it worsens for increasing scan-angles, approaching $5\ dB$ in the worst case.

Motivated by this fact, the attention was therefore moved toward realizing a unit-cell with an extended radiation pattern (in terms of HPBW). Having a wide beamwidth element would be beneficial to compensate for the scan-loss at large angles. The vertical wall loading method was applied to modify the radiation characteristics of a common microstrip patch. The modifications include the use of some parasitic metallic elements, in this case represented by plated vias, that support vertically oriented currents excited by the presence of the patch's fringing electric field. Although the method seemed promising while working on the isolated unit-cell, the presence of the vertical vias inherently introduced some major coupling effects when multiple cells were put close together to design the array. Both the elements' input impedance and radiation patterns were heavily affected. It was observed that the shared ground plane between the cells allowed coupling currents to flow from one unit-cell to adjacent ones.

This not only had effects on radiation patterns, but also made it difficult to achieve impedance matching. Several simulations were performed to visualize and address this critical issue, for example, surface currents and electric fields were plotted inside the design with the help of the simulation software to understand the interaction between the cells. Multiple attempts to achieve impedance matching were carried out and among them, the use of ground plane slots and of decoupling loops were reported and their effects on the behavior of the whole array analyzed. Indeed, the use of decoupling loops allowed to achieve some improvements regarding impedance matching, but the radiation properties remained a problem. In particular, it was noted that, comparing the embedded pattern in the 5×5 arrays of reference and of the proposed unit-cells, no major improvement was made in terms of HPBW, therefore the scanning performance of the two arrays resulted to be almost equivalent. This is clearly not the desired outcome. A major difficulty was encountered, that is how to control the radiation patterns of the cells inside the array. In particular, how to assure that the characteristics of the isolated element are translated to the ones inside the array. This is indeed related to mutual coupling, which can be considered to be the major cause of the pattern modifications.

Future work might focus on researching alternative solutions to achieve wide beamwidth unit-cells. Coupling effects have posed significant challenges in this design, therefore a further understanding and the adoption of effective strategies to mitigate them should be investigated with greater attention.

References

[1] GSMA, "5g-mmwave deployment best practices," *online*, 2022.

[2] C. A. Balanis, *Antenna theory: analysis and design*. John Wiley & sons, 2016.

[3] S. Ghosh and D. Sen, "An inclusive survey on array antenna design for millimeter-wave communications," *IEEE Access*, vol. 7, pp. 83 137–83 161, 2019.

[4] M. Morini, E. Moro, I. Filippini, A. Capone, and D. De Donno, "Exploring upper-6ghz and mmwave in real-world 5g networks: A direct on-field comparison," *arXiv preprint arXiv:2403.00668*, 2024.

[5] I. A. Hemadeh, K. Satyanarayana, M. El-Hajjar, and L. Hanzo, "Millimeter-wave communications: Physical channel models, design considerations, antenna constructions, and link-budget," *IEEE Communications Surveys & Tutorials*, vol. 20, no. 2, pp. 870–913, 2017.

[6] C.-K. Wen, L.-S. Tsai, A. Shojaeifard, P.-K. Liao, K.-K. Wong, and C.-B. Chae, "Shaping a smarter electromagnetic landscape: Iab, ncr, and ris in 5g standard and future 6g," *IEEE Communications Standards Magazine*, vol. 8, no. 1, pp. 72–78, 2024.

[7] J. Xin, S. Xu, S. Xiong, H. Xu, and H. Zhang, "A survey on network controlled repeater technology," in *2022 IEEE 8th International Conference on Computer and Communications (ICCC)*. IEEE, 2022, pp. 1097–1101.

[8] 3GPP, "3gpp r1-2203133: Discussions on side control information to enable nr network-controlled repeaters," *online*, 2022.

[9] J. R. Hampton, *Introduction to MIMO communications*. Cambridge university press, 2013.

[10] R. Mailloux, *Phased Array Antenna Handbook, Third Edition*. Artech House, 2017.

[11] P. Delos, B. Broughton, and J. Kraft, "Phased array antenna patterns—part 1: Linear array beam characteristics and array factor," *Analog Devices*, 2020.

[12] D. Pozar, "The active element pattern," *IEEE Transactions on Antennas and Propagation*, vol. 42, no. 8, pp. 1176–1178, 1994.

[13] A. Ramos, T. Varum, and J. N. Matos, "A review on mutual coupling reduction techniques in mmwaves structures and massive mimo arrays," *IEEE Access*, vol. 11, pp. 143 143–143 166, 2023.

[14] E. Magill and H. Wheeler, "Wide-angle impedance matching of a planar array antenna by a dielectric sheet," *IEEE Transactions on Antennas and Propagation*, vol. 14, no. 1, pp. 49–53, 1966.

[15] M. Soltani and G. V. Eleftheriades, "Wide-angle impedance matching of a patch antenna phased array using artificial dielectric sheets," *IEEE Transactions on Antennas and Propagation*, vol. 72, no. 5, pp. 4258–4270, 2024.

[16] G. Yang, J. Li, D. Wei, and R. Xu, "Study on wide-angle scanning linear phased array antenna," *IEEE Transactions on Antennas and Propagation*, vol. 66, no. 1, pp. 450–455, 2017.

[17] D. Chen, W. Yang, S. Pan, Q. Xue, and W. Che, "Millimeter-wave 45°-polarized ltcc phased array using wide-beam patch-via-wall elements for wide-angle scanning applications," *IEEE Transactions on Antennas and Propagation*, 2023.

[18] D. Pozar and D. Schaubert, "Analysis of an infinite array of rectangular microstrip patches with idealized probe feeds," *IEEE Transactions on Antennas and Propagation*, vol. 32, no. 10, pp. 1101–1107, 1984.